Jacobs

ConnectFlow

Verification Document

Version 13.0

2 November 2023

ConnectFlow

Project No:	DEPRWD17
Document Title:	Verification Document
Document No:	Version 13.0
Date:	2 November 2023
Project Manager:	Pete Appleyard
Author:	ConnectFlow Team

Jacobs Clean Energy Limited

HQ Building
Thomson Avenue
Harwell Campus
Didcot OX11 0GD
United Kingdom
T +44 (0)118 913 7700

www.jacobs.com

Contents

Executive Summary

ConnectFlow is the suite of Jacobs' groundwater modelling software that combines a continuum porous medium (CPM) module and a discrete fracture network (DFN) module. ConnectFlow can be used very flexibly to model groundwater flow and transport in both fractured and porous media on a variety of scales.

The following documentation is available for ConnectFlow:

- ConnectFlow Technical Summary Document;
- ConnectFlow Command Reference Manual;
- ConnectFlow Verification Document;

This document, the Verification Document, provides information on the verification of ConnectFlow, which builds confidence in its flow and transport models.

1. Introduction

ConnectFlow is the suite of Jacobs' groundwater modelling software that a continuum porous medium (CPM) module and a discrete fracture network (DFN) module. ConnectFlow can be used very flexibly to model groundwater flow and transport in both fractured and porous media on a variety of scales.

ConnectFlow models have been used in the following applications:

- safety assessment calculation in support of radioactive waste disposal programmes;
- modelling in support of groundwater protection schemes;
- modelling of landfills;
- regional groundwater flow;
- aquifer contamination;
- site investigation;
- pump test simulation;
- tracer tests;
- saline intrusion;
- design and evaluation of remediation strategies.

Further details of the ConnectFlow's capabilities can be found in [i] and [ii].

The ConnectFlow software has been developed over a period of more than 20 years under a rigorous quality system that conforms to the international standard ISO 9001.

The purpose of this document is to present evidence that ConnectFlow is an appropriate tool to use for modelling groundwater flow and transport. This evidence takes the form of

- Comparison with analytical solutions.
- Comparison of results against other independently written groundwater flow software.

Sections 2, 3 and 4 provide details of a set of verification test cases and associated results. In all cases the results are considered "good" in terms of agreement with the reference data.

A number of the test cases are re-used to extend the range of capabilities tested. These variations include boundary condition types, mesh topology and algorithmic choices.

Section 5 references further testing that has taken place on the ConnectFlow suite of software, which complements and extends the testing covered in the earlier sections.

2. Continuum Porous Media Verification

A summary of the CPM test cases is given in Table 2-1.

Table 2-1 CPM verification tests

Case	Title	Overview
2.1	Radial steady state flow.	Steady state groundwater flow. Modelled using hexahedral, prismatic and constrained meshes. Boundary conditions include mass flux, constant pressure and point sinks.
2.2	Steady state flow in fractured rock.	Steady state groundwater flow. Variations include mesh aligned with fractures and a regular mesh with permeabilties modified via an imported fracture file.
2.3	2D Steady state flow with particle tracks	Steady state groundwater flow with varying permeability. Forward and backward particle tracks and conservative and regular particle tracks are generated.
2.4	Transient buoyant flow	Transient groundwater flow driven by buoyancy via the Boussinesq approximation. Decaying heat source and heat conduction through rock. Transient particle tracks are generated.
2.5	Unsaturated heat transport	Transient unsaturated groundwater flow and heat transport.
2.6	1D Unsaturated flow	Transient unsaturated groundwater flow. Tested using both Crank Nicholson and Gears Method time stepping.
2.7	Seepage face	Steady state radial flow to a well with a seepage face boundary condition.
2.8	Henry's salt transport	Steady state ground water flow. Density dependent on salinity.
2.9	1D Rock matrix diffusion.	Transport of salinity allowing for diffusion between fractured rock and the rock matrix. Tested using Crank Nicholson and Sequential Iteration solver options.
2.10	1D Nuclide transport with sorption and decay	Steady state groundwater flow with nuclide transport. Sorption and decay modelled individually and combined. Tested using Crank Nicholson and Fast Linear Transport options.
2.11	3D mass conserving flux calculation	Post processing for a CPM steady state ground water calculation. Calculation of mass fluxes through finite elements using Cordes-Kinselbach algorithm.
2.12	Reactive transport	Multi-component solute transport with chemical reactions.

2.1 Radial Steady State Flow

2.1.1 Overview

This case models steady groundwater flow in a 2D disk where water is removed from the centre at a constant rate and the outer disk boundary is maintained at a constant head.

The example has a simple analytical solution, which is used to verify the ground water flow solution on a range of mesh topologies.

2.1.2 Problem Definition

The problem definition and solution is a variant of that from Feftra [iii] and de Marsily [iv].

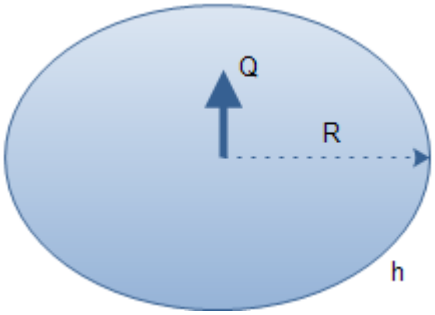

Figure 2-1 Schematic of problem definition

Table 2-2 Input parameters

Symbol	Parameter	Value
h	Head at disk circumference	**0 m**
Q	Outflow from disk	**1.0E-7 m^3/s**
K	Hydraulic Conductivity	**1.0E-8 m/s**
R	Radius of disk	**2000 m**
d	Thickness of disk	**1 m**
r	Radial distance from axis	**0-2000 m**

2.1.3 Variations

2.1.3.1 Mass flux boundary condition

The modelled domain consists of a 15 degree sector, which is truncated at r = 1 m where a mass flux boundary condition is applied. The mesh consists of a line of 3D hexahedral elements, with the spacing refined towards the centre of the domain.

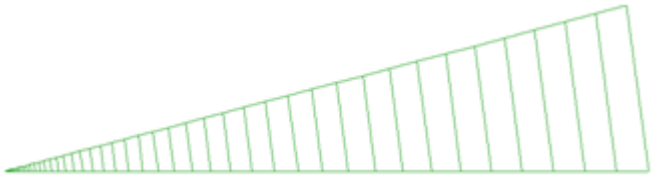

Figure 2-2 Hexahedral mesh with sector truncated close to origin

2.1.3.2 Point sink and prism element

The modelled domain consists of a 15 degree sector, which is composed of a line of hexahedral elements except at the origin where a prism element is used. The outflow is modelled using point sinks at the two vertices on the axis.

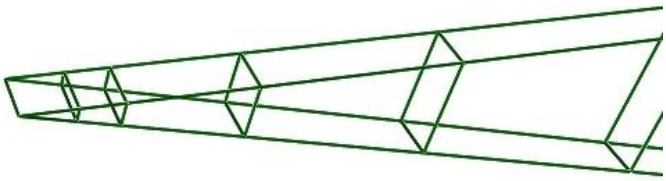

Figure 2-3 Hexahedral mesh with prism at origin

2.1.4 Constrained mesh

The modelled domain consists of a 15 degree sector, which is truncated at r = 1 m, where a mass flux boundary is applied. The mesh consists of a line of 3D hexahedral elements for r = 1 m to r = 1000 m. The mesh is then refined into two cells circumferentially from r = 1000 m to r = 2000 m. The meshes are joined using ConnectFlow constraints. This is an advanced technique that allows grids of different densities to be connected together.

Figure 2-4 Hexahedral constrained mesh

2.1.5 Results

The analytical solution is given by

$$h(r) = h(R) - \frac{Q}{2\pi Kd}\ln(\frac{R}{r})$$

The results from ConnectFlow show very good agreement with the analytical solution in Figure 2-5 and Figure 2-6. The solution for the constrained mesh in Figure 2-7 is a little less accurate as expected.

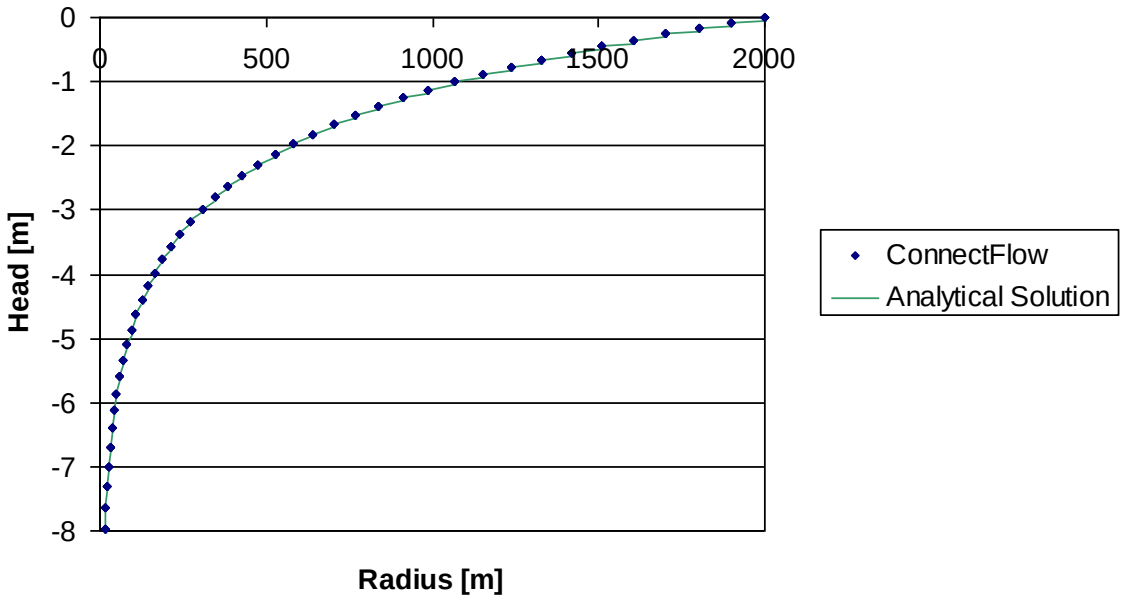

Figure 2-5 Mass flux boundary condition

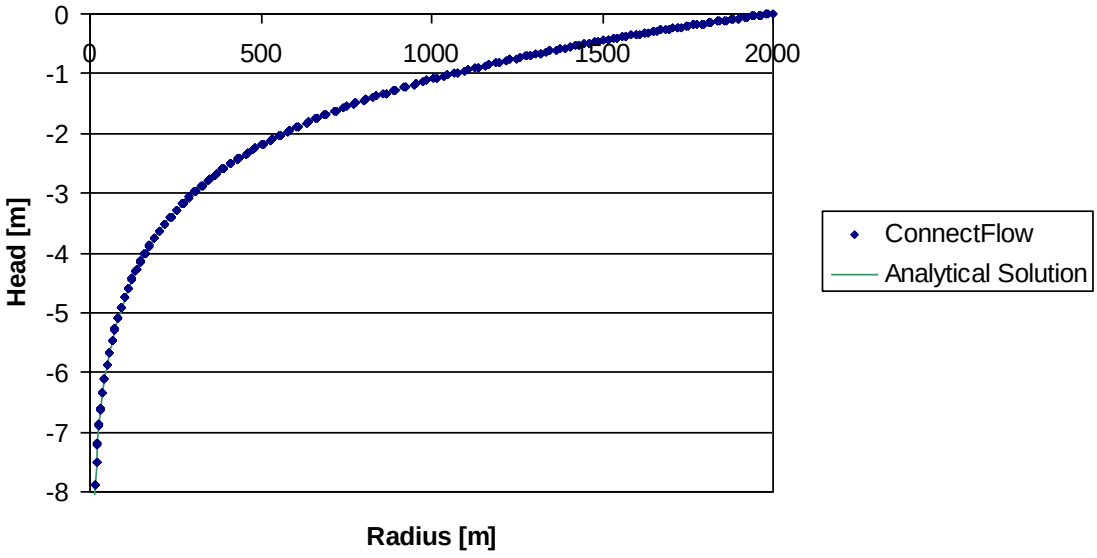

Figure 2-6 Point sink and prism element

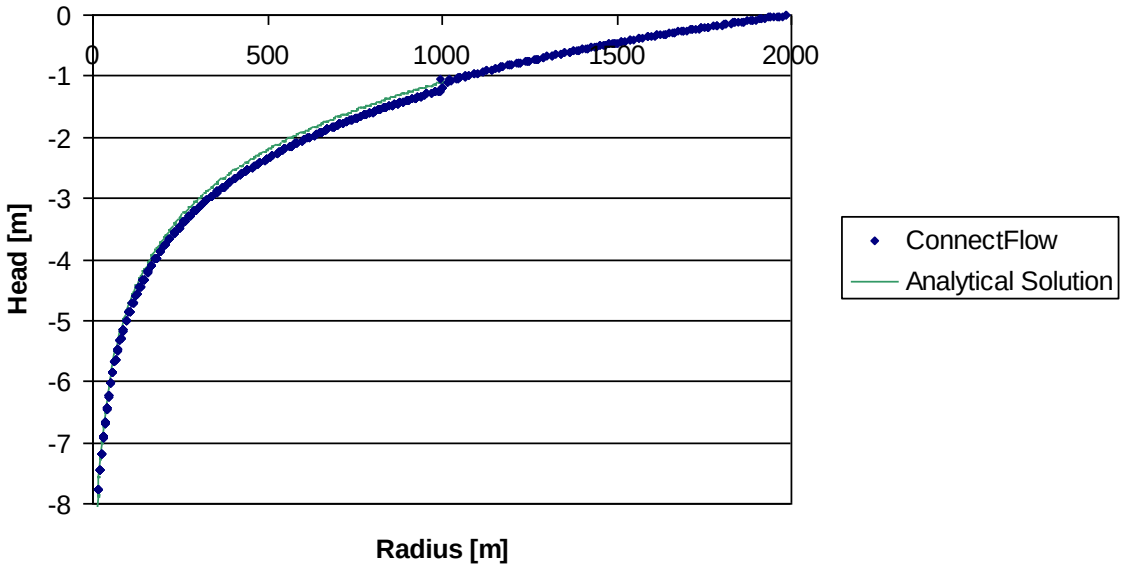

Figure 2-7 Constrained mesh

2.2 Steady Flow in Fractured Rock

2.2.1 Overview

This case is taken from Level 1 of the international HYDROCOIN project for verification of groundwater flow codes [v]. It models steady state flow in a two-dimensional vertical slice of fractured rock. The rock contains two inclined fractures which intersect one another at depth, and have a higher permeability than the surrounding rock.

The topography has been made simple so that it consists of two valleys located where the fracture zones meet the surface. To simplify the problem definition, the shape of the surface is described by straight lines. Although the surface topography is symmetric, the flow is influenced by the asymmetry of the fracture zones.

This problem is based on an idealized version of the hydrogeological conditions encountered at a potential site for a deep repository in Swedish bedrock. A detailed three-dimensional model of this was made in a separate study [vi].

2.2.2 Problem Definition

Figure 2-8 depicts the modelled domain.

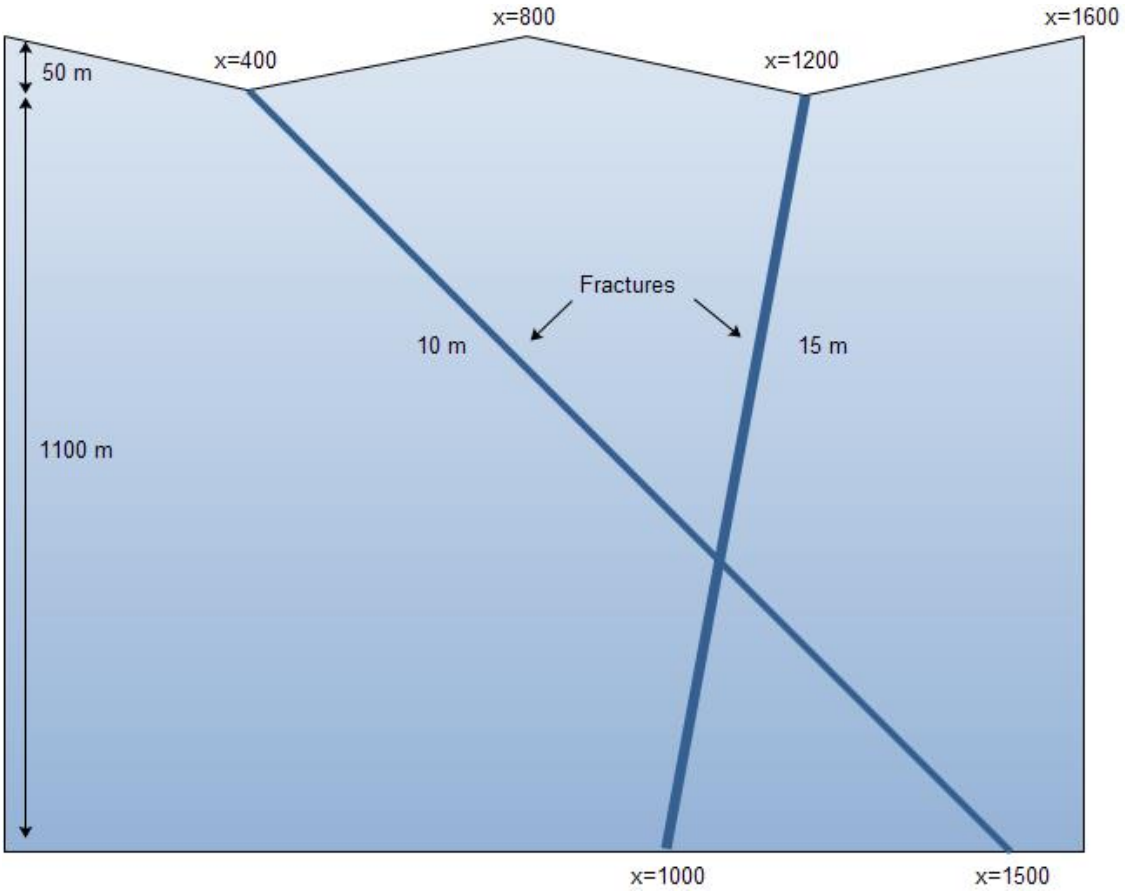

Figure 2-8 Fractured rock

Table 2-3 Input parameters

Symbol	Parameter	Value
K_r	Hydraulic conductivity of rock	**1.0E-8 m/s**
K_f	Hydraulic conductivity of fracture	**1.0E-6 m/s**
ϕ	Porosity	**0.03**

2.2.3 Variations

2.2.3.1 Multiple Element Types

In this variation the region is meshed using a mix of hexahedral (CB27) and prismatic elements as shown in Figure 2-9.

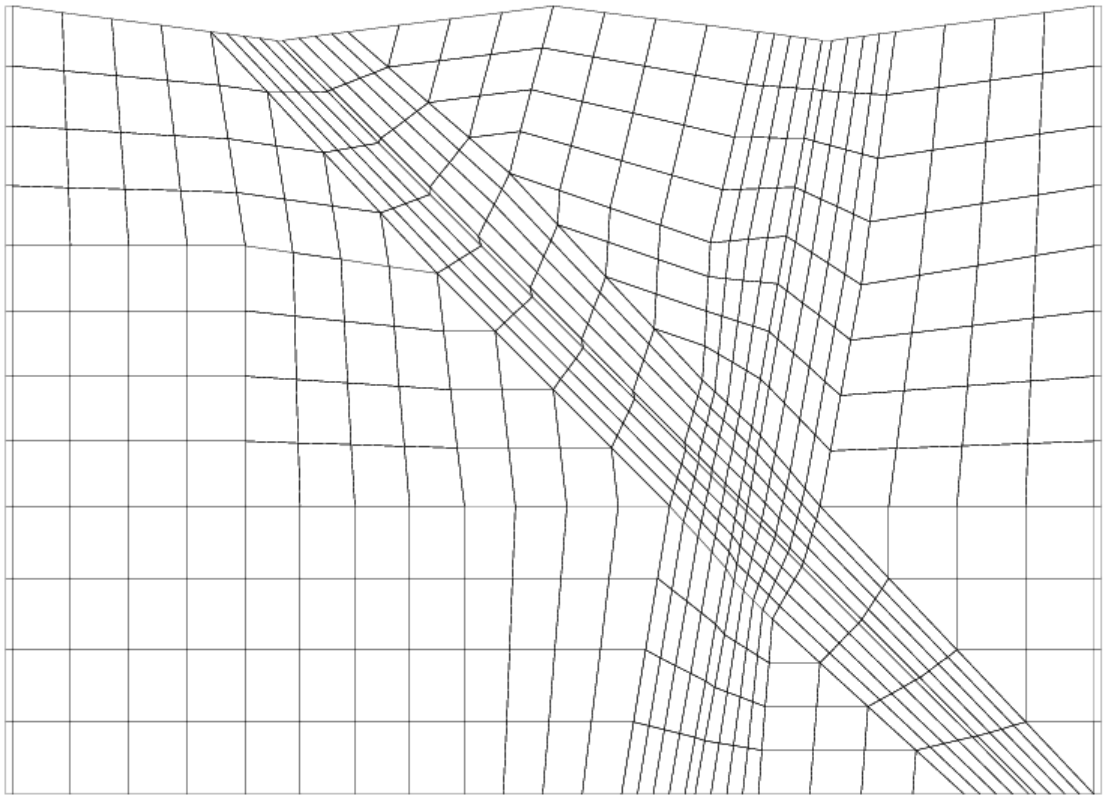

Figure 2-9 Mesh around fractures

2.2.3.2 Hexahedral Elements

In this variant hexahedral elements only are used, and then the element permeabilties are modified according to the imported fractures. It was found that in this scenario the lower order CB08 elements gave a more accurate solution than the CB27 elements for a given mesh resolution. This is likely to be due to the rapid change in permeabilties that are not aligned with the grid.

The results presented here are for mesh with 160x80 elements. The representation of the fractures using this approach is illustrated in Figure 2-10.

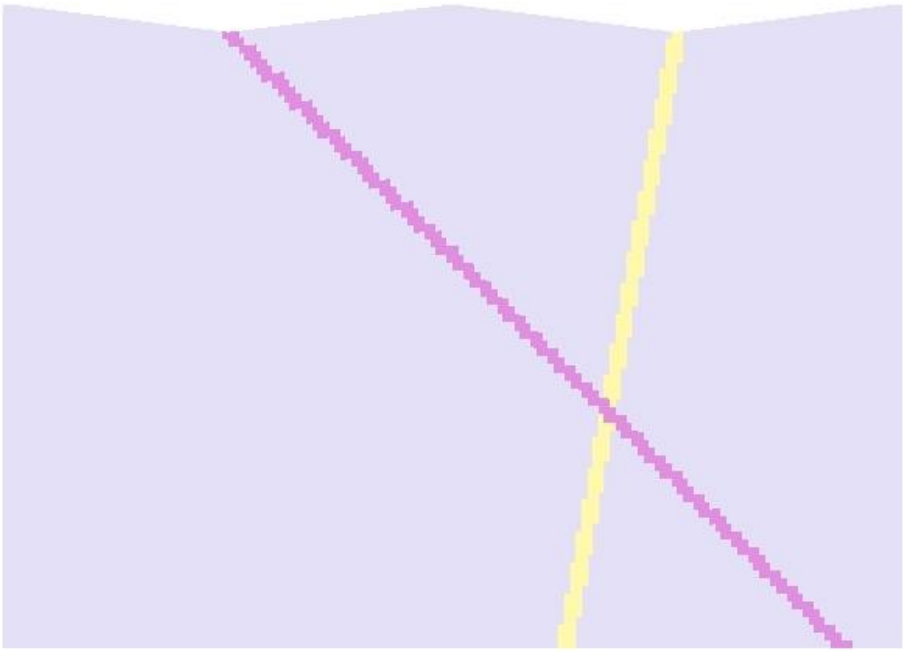

Figure 2-10 Hexahedral elements

2.2.4 Results

The results presented here compare head profile at a height of y=-200. The multiple element type results show excellent agreement with the HYDROCOIN study. The hexahedral element results have a head profile that is close to the HYDROCOIN results, but with slightly higher heads across the range.

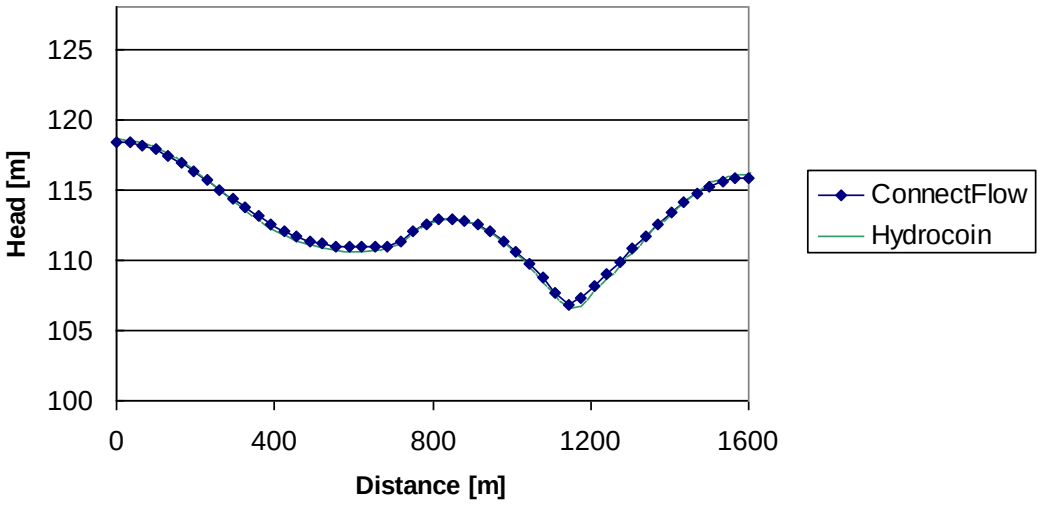

Figure 2-11 Head at height -200m (multiple element types)

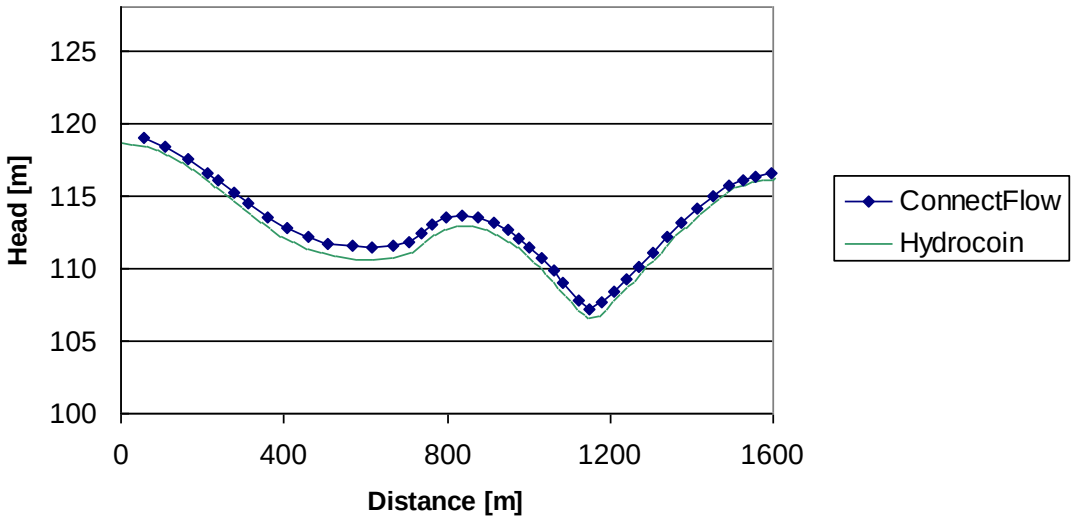

Figure 2-12 Head at height -200m (hexahedral element mesh)

In addition, the ConnectFlow results were compared against the Feftra base case results reported in [iii]. The differences in head between the two codes being less than 1% for the multiple element type mesh and less than 2% for the hexahedral mesh (relative to the head variation in the surface boundary condition).

A particle track starting from position (100,-200) also showed good agreement with the Feftra base case, as illustrated in Figure 2-13.

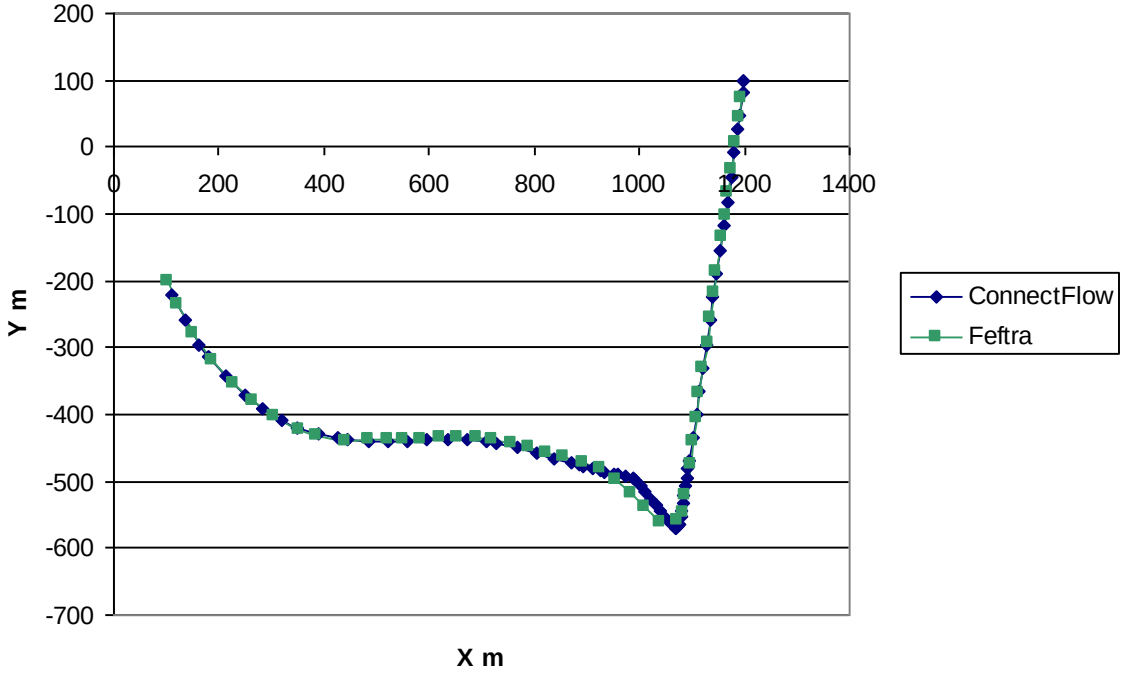

Figure 2-13 Particle track from (100,-200) with multiple element types

In Figure 2-14 the ConnectFlow particle track is overlaid on the geometry, with the track colouring representing elapsed time. The total time of the track is 5% higher than the Feftra base case.

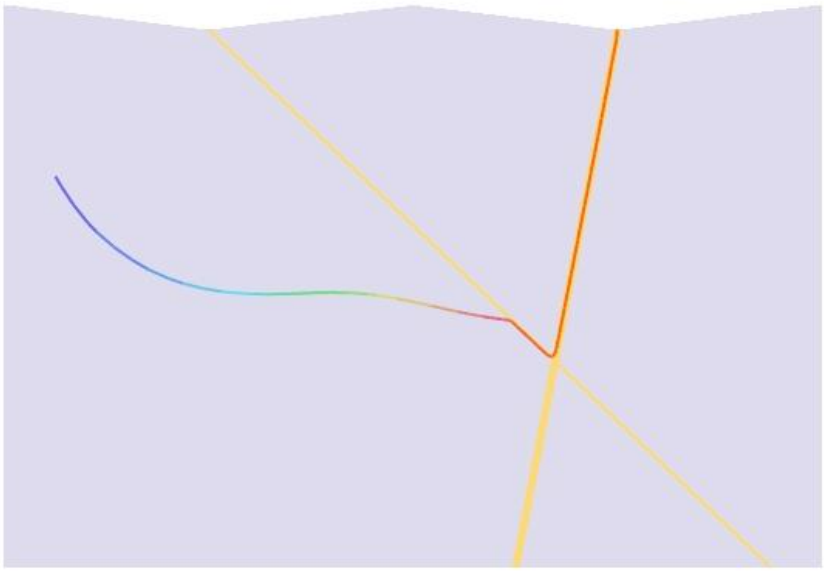

Figure 2-14 Particle track overlaid on geometry

2.3 2D Steady Flow with Particle Tracks

2.3.1 Overview

This case is taken from Level 3 of the international HYDROCOIN project for verification of groundwater flow codes [vii]. It models steady state flow in a two-dimensional vertical slice of rock, containing a circular region of higher permeability.

The case has a non-uniform analytical solution and is used in the HYDROCOIN study to test particle tracking.

2.3.2 Problem Definition

The analytical solution assumes an infinite domain for the low permeability region. The original HYDROCOIN setup had a disk radius a = 10m, an outer region Lx = 50m, Ly = 30m and used both calculated and analytically prescribed flow fields.

In the ConnectFlow results presented here both the flow field and particle tracks are calculated. From initial tests it was found that a larger outer region was required in order to appropriately model the analytical solution.

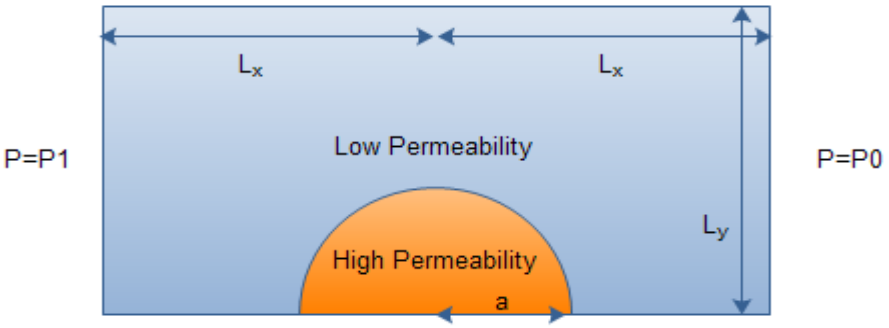

Figure 2-15 Schematic of problem definition

Table 2-4 Input parameters

Symbol	Parameter	Value
Lx	Upstream and downstream distances	**250 m**
Ly	Vertical outer region distance	**240 m**
a	Radius of inner disk	**10 m**
P1	Upstream pressure	**2.5E5 Pa**
P0	Downstream pressure	**-2.5E5 Pa**
k_o	Permeability of outer region	**1.0E-15 m^2**
k_i	Permeability of inner region	**1.0E-13 m^2**
ϕ	Porosity	**0.1**
ρ	Density	**1000 kg/m^3**
μ	Viscosity	**1.0E-3 Pa.s**

Eight particle tracks are released 50 m upstream of the disk centre and at Y values of 10, 12, 14, 16, 18, 20, 22 and 24 m.

The analytical solution for the pathlines is given in the HYDROCOIN report [vii] as

$$y = y_o / (1 + \frac{a^2}{r^2} \frac{(k_i - k_o)}{(k_i + k_o)})$$ for r > a

$$y = y_o \frac{(k_i + k_o)}{2k_o}$$ for r < a

Where r is the distance from the center of the disk and y0 is a constant representing the height of the track a long distance away from the origin.

2.3.3 Variations

2.3.3.1 Wrapped Mesh

In this variation, the mesh is modelled to wrap around the cylinder. A higher quality mesh is generated, but some vertices are surrounded by 3 elements and others by 5. A mesh of around 3000 elements was used.

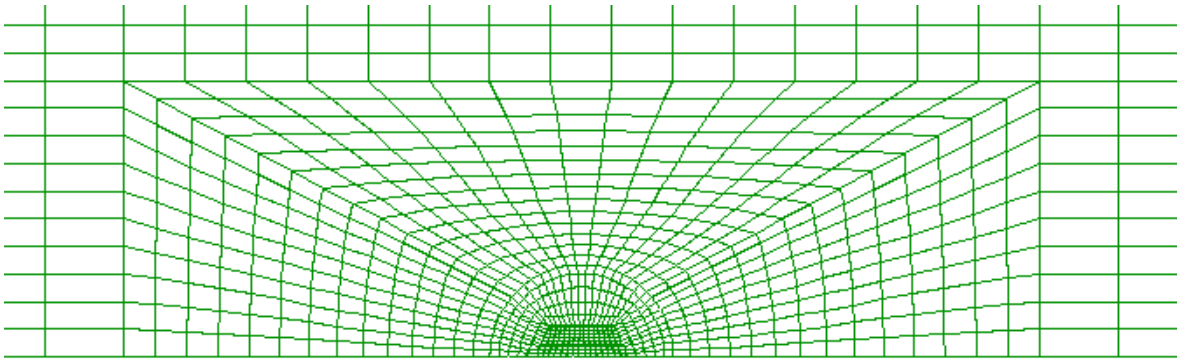

Figure 2-16 Wrapped mesh

The mesh topology does not support the mass conserving particle tracking method, so just the regular particle tracking approach was used.

2.3.3.2 Regular Mesh (Distorted Elements)

In this variation a regular mesh is used where elements always have 4 neighbours, which results in a distorted mesh inside the cylindrical region. A mesh of around 6000 elements was used. The mesh is finer in this case, as the refinement of the cylinder propagates to the boundaries.

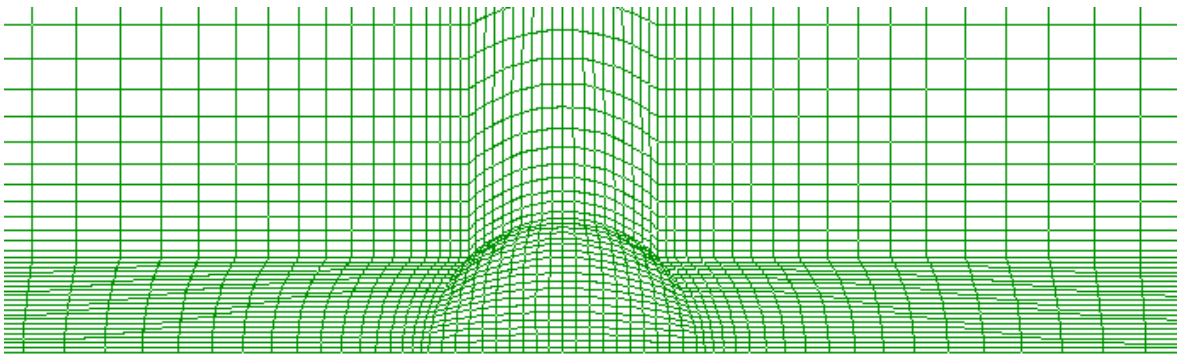

Figure 2-17 Regular mesh

Both regular particle tracking and the mass conserving method were used.

2.3.4 Results

The calculated particle tracks were within 1% of the analytical solution, both in terms of location at each point and in terms of overall travel from x = -50m to x = +50m.

Table 2-5 Particle tracking results

Calculation method	% Error in Location	% Error in Travel Time
Wrapped mesh, regular tracks	0.96%	**0.44%**
Regular mesh, regular tracks	0.41%	**0.17%**
Regular mesh, mass conserving tracks	0.27%	**0.20%**

Backward particle tracks from x = 50m to x = -50m were also calculated and were again within 1% of the analytical values.

Table 2-6 Backward particle tracking results

Calculation method	% Error in Location	% Error in Travel Time
Wrapped mesh, regular tracks	0.93%	**0.45%**
Regular mesh, regular tracks	0.41%	**0.17%**
Regular mesh, mass conserving tracks	0.27%	**0.21%**

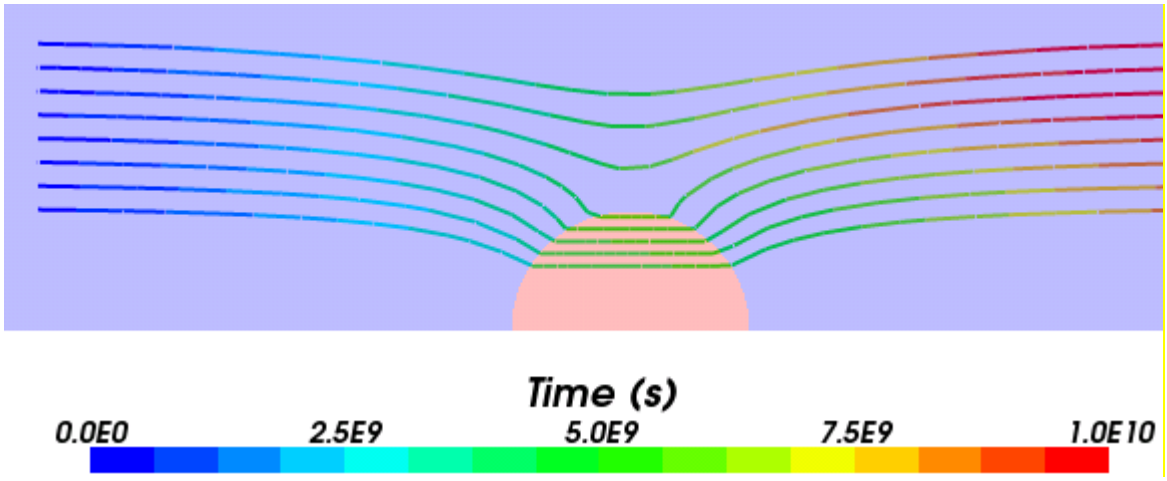

Figure 2-18 Particle tracks for wrapped mesh

In addition, the volumetric flow rate through the inner disk was calculated for variation 1, using the "calculate conserved mass flux" option.

The flow through the disk from [vii] has a constant velocity in the X direction of $\frac{k_o k_i}{(k_i + k_o)} \frac{(P1 - P0)}{2L_x \mu\varphi}$. For the values in Table 2-4, this gives a flow rate of 1.9801E-7 m^3/s. The calculated ConnectFlow value is 1.9834E-7 m^3/s which is within 1% of the analytical solution.

2.4 Transient Buoyant Flow

2.4.1 Overview

This case is taken from Level 1 of the international HYDROCOIN project for the verification of groundwater flows [v]. It models the flows arising from an exponentially decaying heat source and has an analytical flow solution.

This type of problem is relevant when considering the disposal of heat emitting radioactive waste, where buoyancy induced flows can last for thousands of years.

2.4.2 Problem Definition

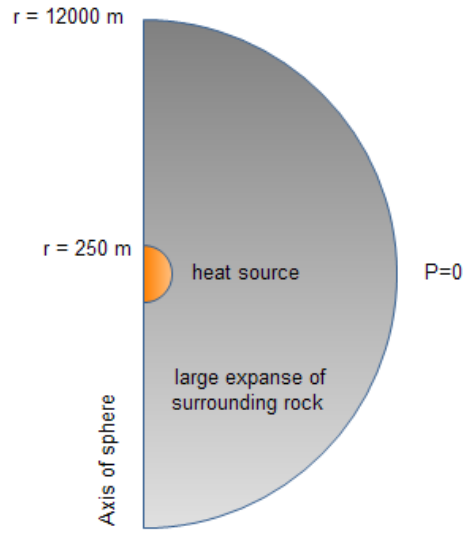

Figure 2-19 Schematic of problem definition

The test problem models transient heat flow through the rock only and ignores advection of heat. The viscosity is taken to be constant and the density variation is only applied to the buoyancy term of the equations.

The modelled domain consists of a thin one cell thick segment of the sphere. The analytical solution assumes an unbounded region of surrounding rock. Following some initial test runs, a surrounding region of 12000 m was selected as having a minimal impact on the solution.

A relatively fine mesh of 26000 elements was used. Coarser meshes of around 5000 elements give good results for the temperature and pressure profiles but have larger errors on particle tracking positions and travel times.

Table 2-7 Input parameters

Symbol	Parameter	Value
W_0	Initial power output	**250 MW**
λ	Decay constant in heat source	**7.3215E-10 1/s**
ρ_r	Rock density	**2.6E3 kg/m^3**
C	Rock specific heat	**8.79E2 J/kg K**
Γ_r	Rock thermal conductivity	**2.51 W/m K**
k	Permeability	**1.0E-16 m^2**
ϕ	Porosity	**1.0E-4**
S_s	Specific storage coefficient	**2.0E-6 1/m**
ρ	Density	**992.2 kg/m^3**
μ	Viscosity	**6.529E-4 Pa.s**
β	Expansion coefficient of water	**3.85E-4 1/K**

2.4.3 Results

The comparison of results includes temperature profiles Figure 2-20, pressure profiles Figure 2-21 and transient particle tracks Figure 2-22 and Figure 2-23.

The results are all within 7% of the analytical solution, including the particle travel times.

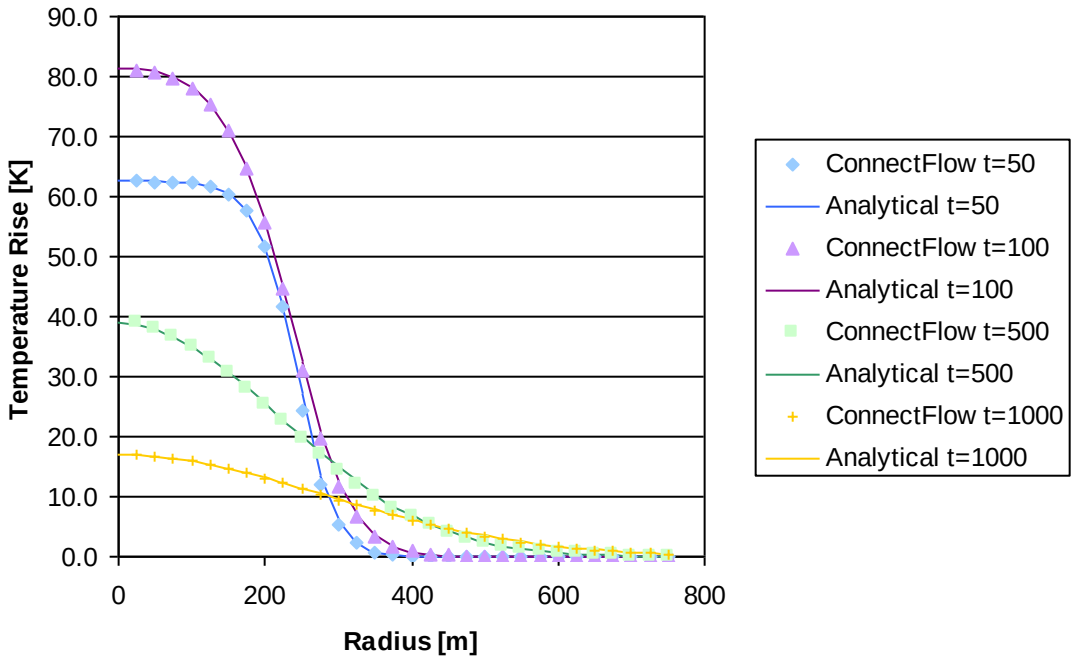

Figure 2-20 Vertical temperature rise along the vertical sphere centreline

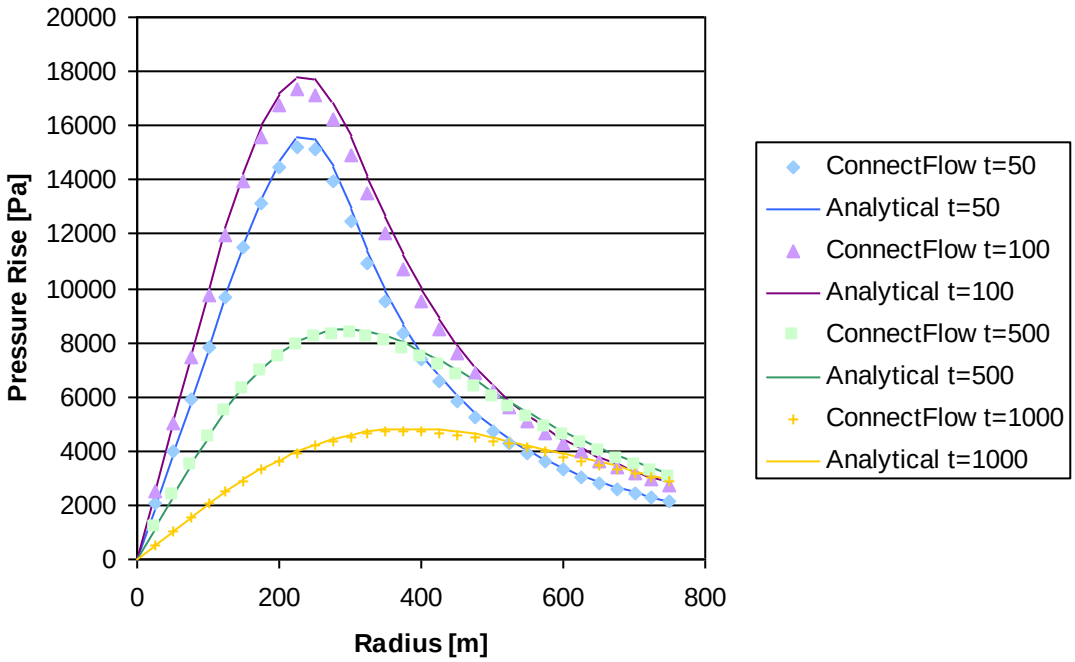

Figure 2-21 Vertical pressure rise along the vertical sphere centreline

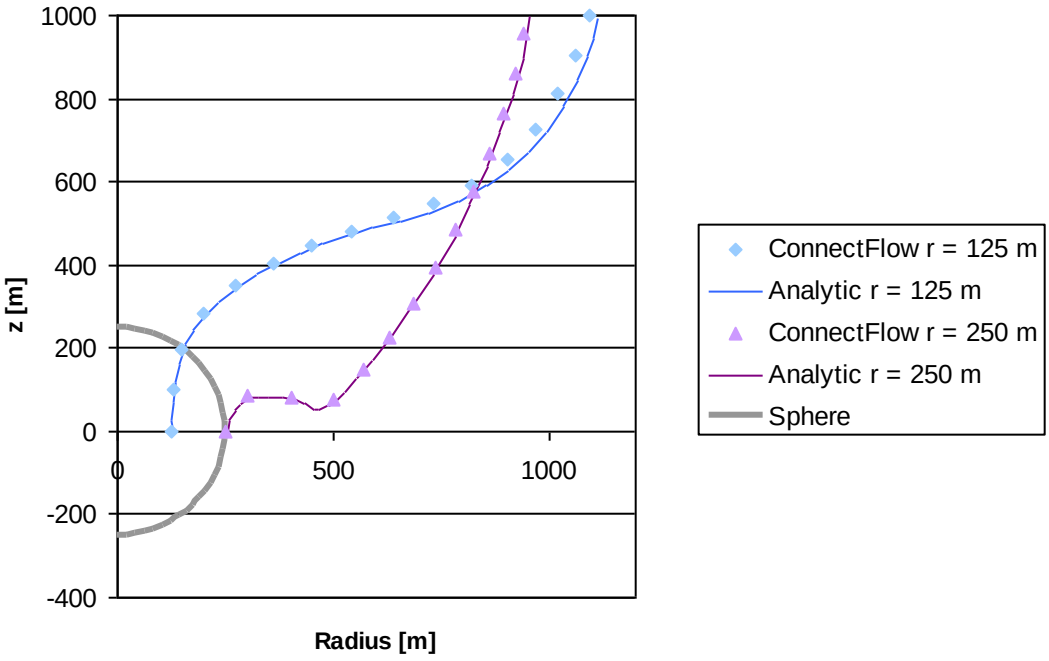

Figure 2-22 Particle tracks originating from z = 0 starting at t = 100 years

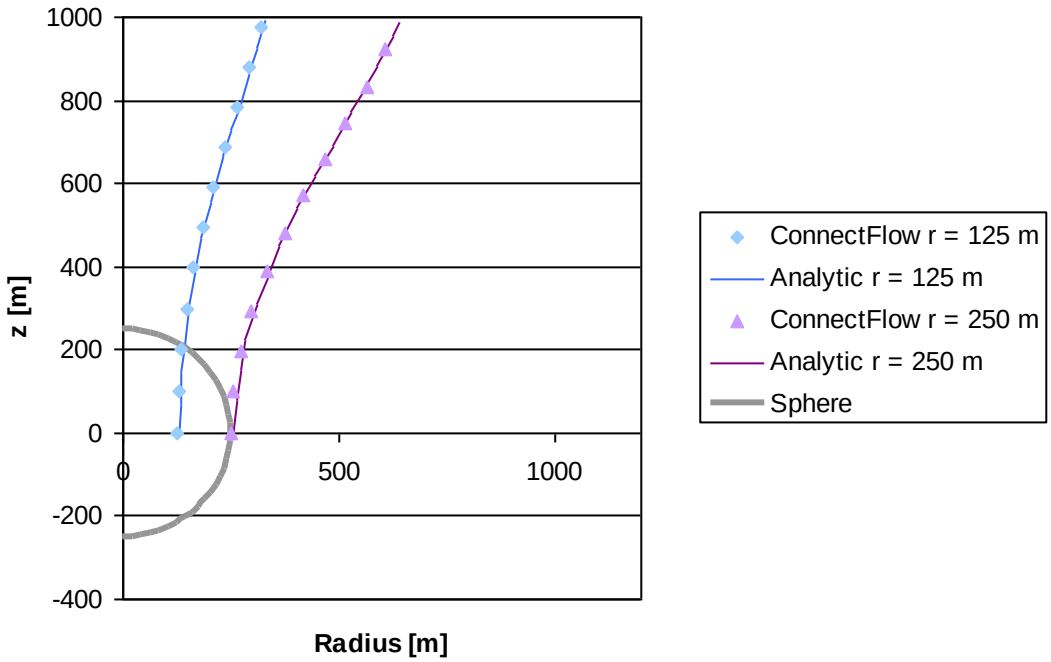

Figure 2-23 Particle tracks originating from z = 0 starting at t = 1000 years

2.5 Unsaturated Heat Transport

2.5.1 Overview

In this section, the base-case model[1] of the Sensitivity Analysis Task of the Äspö Engineered Barrier Systems (EBS) Task Force [viii] is investigated. A single deposition hole is modelled in a 2D axisymmetric model, including the bentonite buffer and the host rock. The canister is not explicitly represented; instead a heat source term is applied on a canister buffer interface. Emphasis of the analysis is on the variation of the temperature and saturation with time along fixed positions on the bentonite buffer.

2.5.2 Problem Definition

The deposition hole is based on the KBS-3V [viii] specifications. Dimensions of the computational domain and its features are schematically illustrated in Figure 2-24.

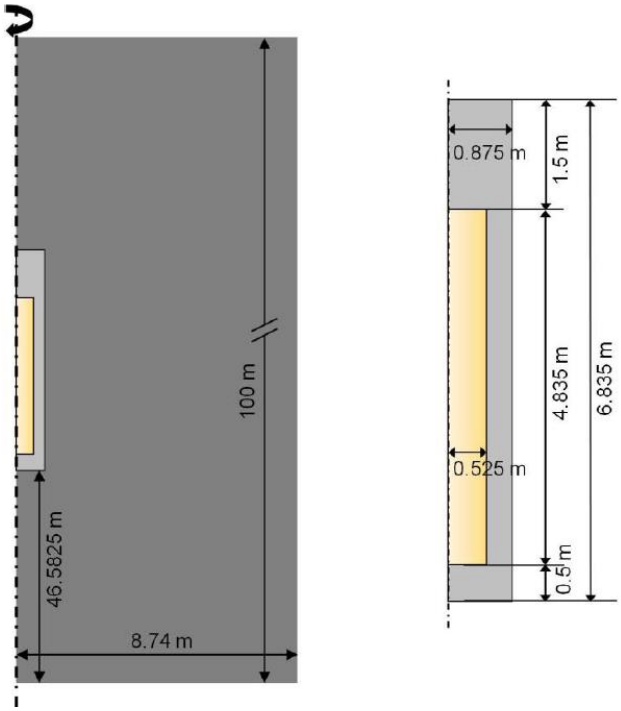

Figure 2-24 Dimensions of the computational domain (dark grey is the host rock, light grey is the bentonite yellow is the area of canister. This figure is reproduced from [viii]

The modelling process is subdivided into two phases (i.e. Phase 1 and Phase 2). Phase 1 is a purely hydraulic calculation and considers an open deposition hole (i.e. with the canister and bentonite absent). Dirichlet boundary conditions (BCs) for the pressure are specified on the surface of the deposition hole (i.e. atmospheric pressure) and on the upper and lower boundaries of the model. A Neumann 'no-flow' BC, is applied along the axis of symmetry and at the other outer boundaries. Hydrostatic pressure is set as an initial condition (IC) throughout the rest of the domain and a transient simulation is performed until steady state is reached. Phase 1 provides the steady state pressure field for Phase 2, as an IC. Phase 2 is a coupled Thermo – hydraulic calculation. The numerical simulation begins on the date of emplacement of the canister and bentonite buffer within the deposition hole, and a transient calculation is performed for 100 years after the installation. The BCs applied in Phase 1 are used, with the addition of a Neumann BC at the outer edge of the canister – bentonite interface. A heat source applied at the interface emulates the heat generated by nuclear fuel waste. The power

[1] For the purposes of this verification exercise, the thermal conductivity of the buffer is assumed to be constant rather than a function of saturation (i.e. $0.7 \cdot (1 - S_l) + 1.3 \cdot S_l$ W/(m·K)) prescribed in the Task description for the base-case model.

decay used in the modelling is given by Equation (1). The initial power output $P_0$is 1700 W, whilst parameters t_i and a_i are listed in Table 2-8.

$$P(t) = P_o \sum_{i=1}^{7} a_i \exp\left(-\frac{t}{t_i}\right) \quad (1)$$

The ICs and BCs employed in the modelling of both phases are schematically summarised in Figure 2-25. The physical parameters used in the modelling are presented in Table 2-9 and Table 2-10.

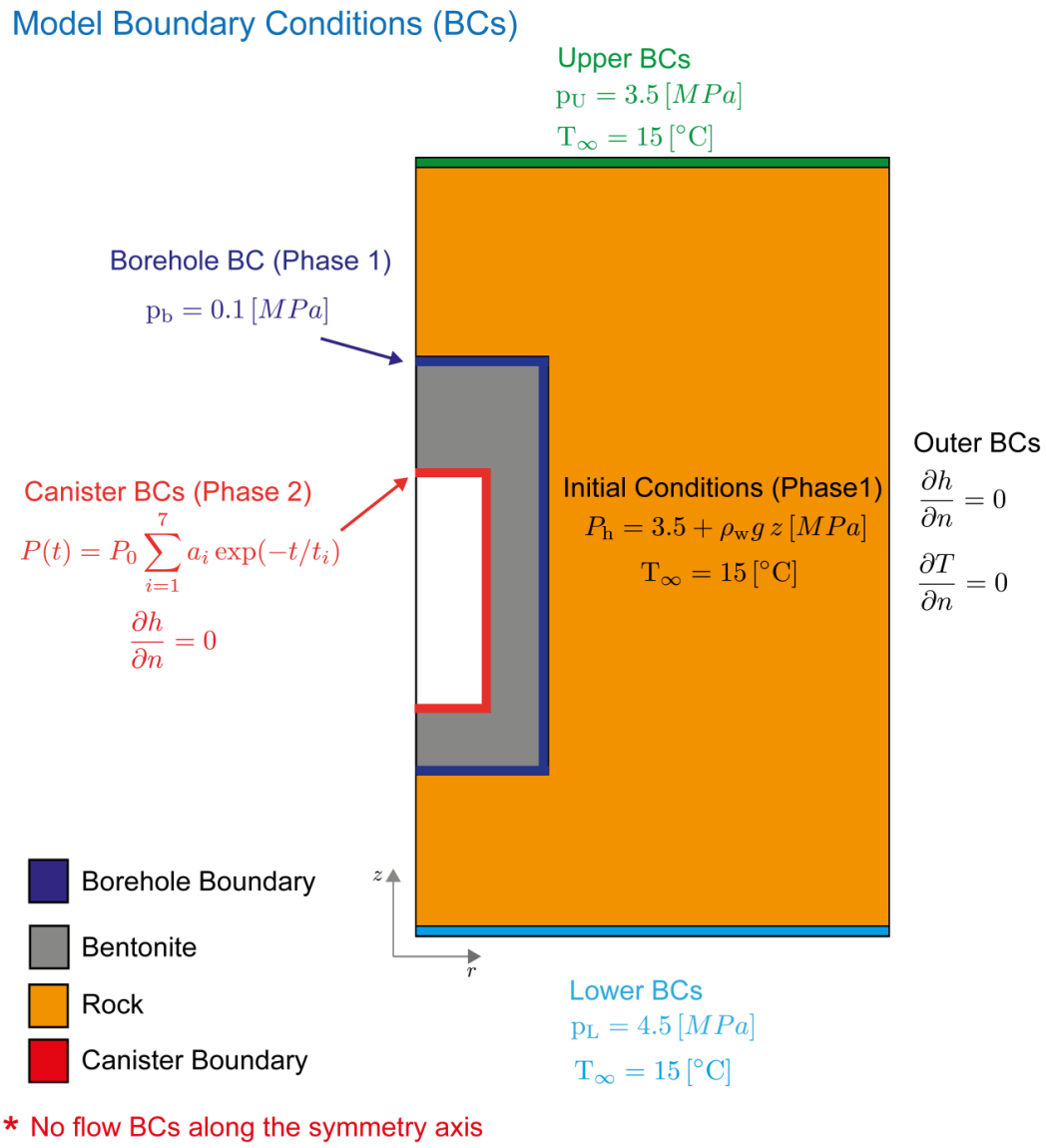

Figure 2-25: Summary of the ICs and BCs for Phase 1 and Phase 2

The standard Van Genuchten model (i.e. the functional forms $S_l\left(P_{cap}\right), k_{rel}(S_l)$), as presented in Table 2-10 for the host rock), is fully implemented in ConnectFlow. The task specifications require that, for the bentonite buffer, a modified Van Genuchten function, is to be used (with an extra term in ($S_l(P_{B,cap})$ in Table 2-10). In addition, a cubic law relating the relative permeability and the saturation is also prescribed. This functionality is easily implemented in ConnectFlow with the aid of two user defined external routines, **uspcap.f** and **uskrel.f.** These versatile routines enable the user to freely specify the relationships used.

In total, the grid consists of approximately 2500 finite elements. In Figure 2-26, the discretisation along the bentonite buffer, the canister – bentonite interface, as well as the points used for the sampling of temperature and saturation are presented.

Table 2-8 Constants and coefficients for the power output from the canister, as described in Equation (1)

I	t_i (years)	a_i
1	20	0.0601
2	50	0.7050
3	200	-0.0547
4	500	0.2498
5	2000	0.0254
6	5000	-0.0094
7	20000	0.0239

Table 2-9 Thermodynamic, transport and hydraulic properties, are presented for the fluid, the host rock and the bentonite buffer

Parameter	Value
Fluid Properties	
Density (ρ_l)	**1000 kg / m^3**
Viscosity (μ_l)	**1.0 x 10^{-3} Pa·s**
Host Rock Properties	
Density (ρ_R)	**2700 kg / m^3**
Porosity (n_R)	**0.003**
Initial Liquid Saturation ($S_{l,0}$)	**1.0**
Capillary Pressure ($P_{R,cap}$)	$S_l\left(P_{cap}\right)=\left(1+\left(\frac{-P_{cap}}{P_0}\right)^{\frac{1}{1-m}}\right)^{-m}$, **$P_0$ = 1.74 MPa, m=0.60**

Parameter	Value
Relative permeability (liquid) ($k_{R,rel}$)	$k_{rel}(S_l) = \sqrt{S_l}\left(1-\left(1-S_l^{\left(\frac{1}{m}\right)}\right)^m\right)^2$, **$m$=0.6**
Tortuosity (τ_R)	**1.0**
Bentonite Properties	
Density (ρ_B)	**2780 kg / m3**
Porosity (n_B)	**0.438**
Initial Liquid Saturation ($S_{l,0}$)	**0.61**
Capillary Pressure ($P_{B,cap}$)	$S_l\left(P_{B,cap}\right) = \left(1+\left(\frac{-P_{B,cap}}{P_0}\right)^{\frac{1}{1-m}}\right)^{-m}\left(1+\frac{P_{B,cap}}{P_1}\right)^{m_1}$ **P_0 = 5.523 MPa, m=0.16, P_1 = 950 MPa, m_1=1.6.**
Tortuosity (τ_B)	**1.0**
Relative permeability (liquid) ($k_{B,rel,l}$)	S_l^3

Table 2-10 Thermal properties of the fluid, the host rock and the buffer.

Parameter	Value
Fluid Properties	
Thermal conductivity (λ_l)	0.6 W/(m·K)
Specific heat capacity (c_l)	4.183 kJ/(kg·K)
Host Rock Properties	
Thermal conductivity (λ_R)	2.4 W/(m·K)
Specific heat capacity (c_R)	770 J/(kg·K)
Bentonite Properties	
Thermal conductivity (λ_B)	1.2 W/(m·K)
Specific heat capacity (c_B)	800 J/(kg·K)

2.5.3 Results

In Figure 2-27, a series of surface plots of the temperature distribution (Phase 2 calculation) collected at different times are displayed. The temperature variation is shown for the whole extent of the computational domain. The Task Description, prescribes six sampling points (see

Figure 2-26) to be used for the collection of temperature and saturation measurements. In this study, results obtained using ConnectFlow are directly compared to ones obtained byTOUGH2. A good agreement is shown for both temperature (Figure 2-28) and saturation profiles (Figure 2-29). The maximum temperature achieved for all points by ConnectFlow is found to be smaller by few degrees. However, even though there is a moderate deviation on the slope of saturation rate, full saturation is achieved for all points at approximately the same time, with ConnectFlow predicting a fully saturated state at slightly earlier times.

Deviations are to be expected. Even though the same grid is used for both computations, a different numerical solution scheme is adopted in TOUGH2 (i.e. Finite Difference), while the Finite Element method is opted for ConnectFlow. In particular, the set of equations solved by ConnectFlow and TOUGH2 are different. TOUGH2 uses a multiphase calculation, whilst ConnectFlow solves Richards equation [ix], [x] & [xi]. Within this investigation, emphasis was placed on the minimisation of gas effects within the TOUGH2 simulation, thus an approximation to Richards equation is justified.

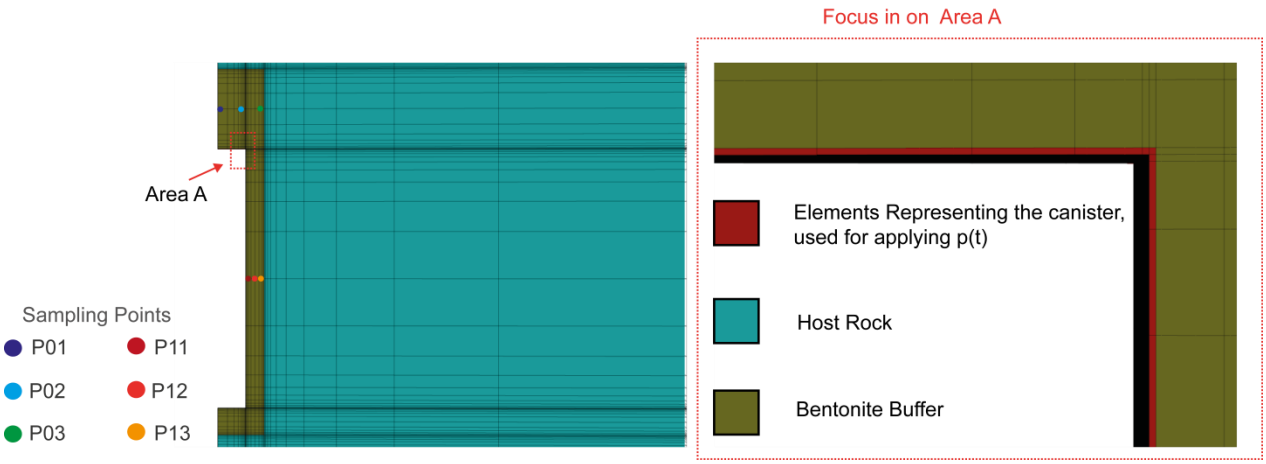

Figure 2-26 Part of the mesh used for the computations is given in the figure on the left, showing the discretisation of the buffer. Temperature and saturation profiles are obtained for the six points in the buffer and presented in Figure 2-28 & Figure 2-29. On the right, the interface layer (red elements) between the canister and the buffer is shown.

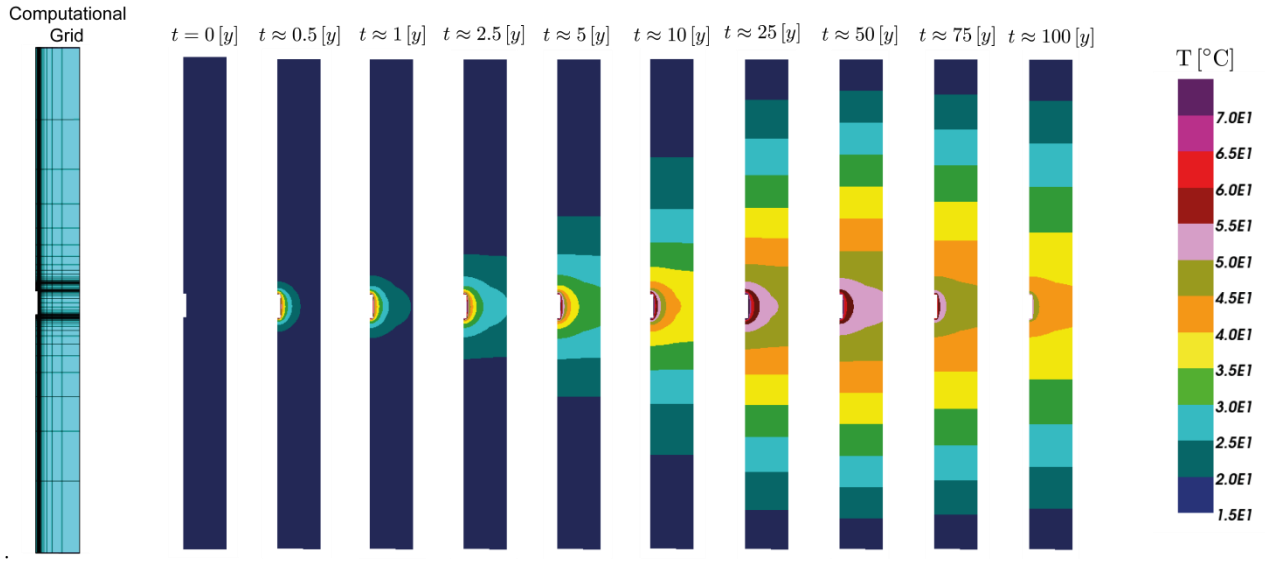

Figure 2-27 The temperature field in the model is plotted at different times.

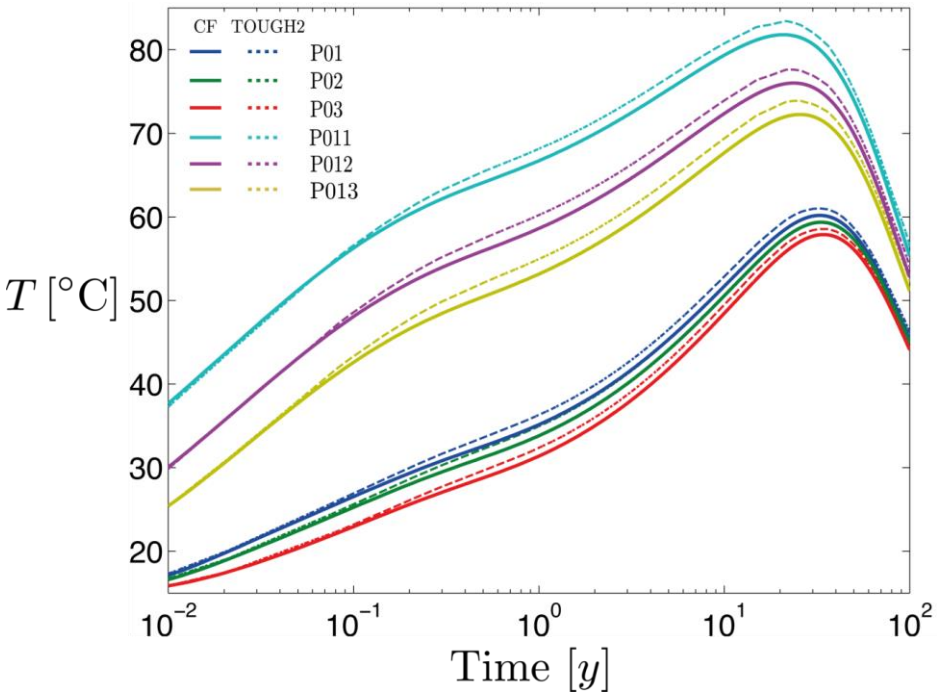

Figure 2-28 Variation of Temperature with time, calculated by ConnectFlow (–) and TOUGH2(- -) simulations.

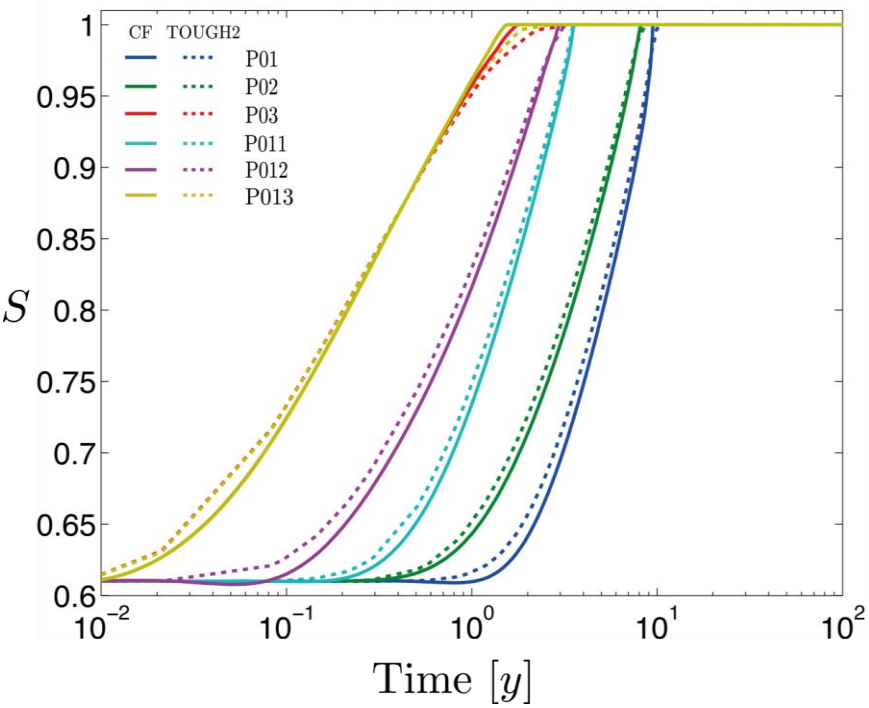

Figure 2-29 Variation of Saturation with time, calculated by ConnectFlow (–) and TOUGH2(- -) simulations.

2.6 1D Transient Unsaturated Flow

2.6.1 Overview

This case models transient flow in a 50 m horizontal section of clay, where the initial pressure is constant and the ends are maintained at a different pressure.

For small variations in pressure the problem has a semi-analytical solution.

2.6.2 Problem Definition

Figure 2-30 Schematic of problem definition

The region was meshed using a line of 40 hexahedral elements.

The unsaturated behaviour for relative permeability and capillary pressure were modelled using Van Genuchten functions.

Table 2-11 Input parameter values

Symbol		Parameter	Value
K		Hydraulic Conductivity	**5.0E-14 m/s**
ϕ		Porosity	**0.18**
S_s		Specific storage coefficient	**2.0E-6 1/m**
ρ		Density	**1000 kg/m^3**
μ		Viscosity	**1.0E-3 Pa.s**
Van Genuchten	n	Exponent	**1.5**
	P_r	Entry pressure	**8.0E6 Pa**
	S_{lr}	Residual Saturation	**0.01**

As the variation in saturation across the model is small (<3%), we can approximate the equations for transient unsaturated flow as a diffusion equation, so that, in 1D

$$\frac{\partial P}{\partial t} = \alpha \frac{\partial^2 P}{\partial x^2}$$

where

α is the diffusivity [m^2s^{-1}];

x is distance [m];

P is pressure;

t is time.

and α is given by

$$\alpha = \frac{k_r K}{S_s S + \phi \rho g \frac{\partial S}{\partial P}}$$

where S is the liquid saturation and k_r is the relative permeability and g is gravity.

For the case considered here, the values in the above equation are averaged between the initial conditions and the boundary conditions to provide an approximate constant diffusivity.

Given this approximate constant diffusivity, a semi-analytical solution can be obtained from

$$P = P_1 + (P_0 - P_1) \sum_{n=0}^{\infty} \frac{4}{(2n+1)\pi} \exp\left\{ \frac{-(2n+1)^2 \pi^2 \alpha t}{L^2} \right\} \sin\left\{ \frac{(2n+1)\pi x}{L} \right\}$$

Where P_0 is the uniform initial pressure field -1.1E7, P_1 the boundary pressure of -1.0E7, and L the domain length of 50 m.

2.6.3 Variations

2.6.3.1 Crank Nicholson

The transient behaviour is modelled using Crank Nicholson with 150 time steps of size 1.0E11 seconds.

2.6.3.2 Gears method

The transient behaviour is modelled using Gears predictor-corrector time stepping method with an initial time step of 1.0E11 seconds. A total of 23 time steps were used.

2.6.4 Results

The results show good agreement with the semi-analytical solution. The small differences are due to the semi-analytical model assuming constant saturation with time.

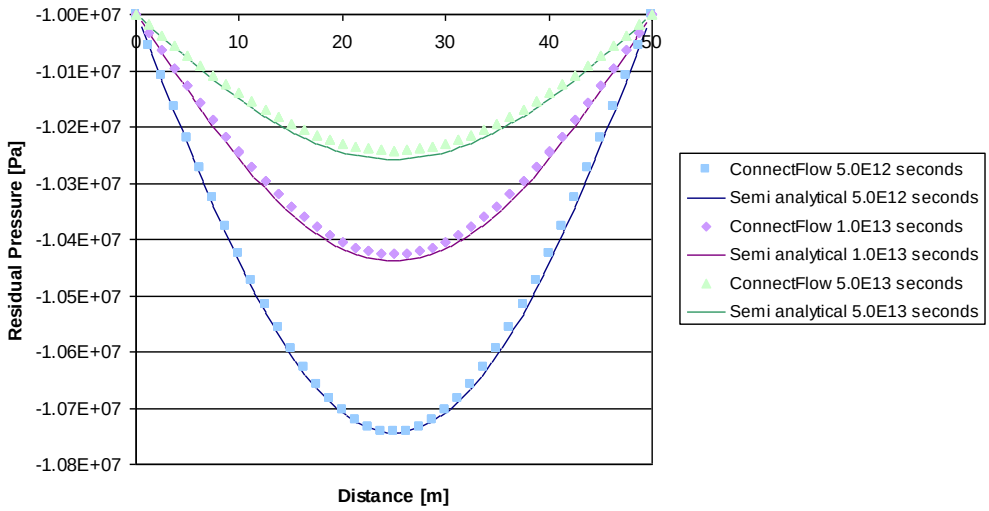

Figure 2-31 Crank Nicholson - Transient unsaturated pressures

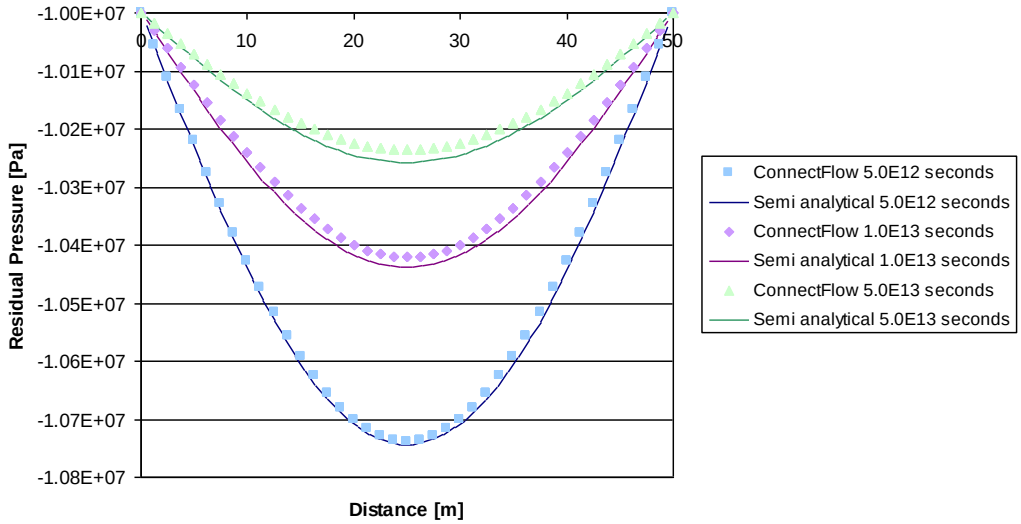

Figure 2-32 Gears method - Transient unsaturated pressures

An additional comparison was made with Tough2v2 software [xii].

Table 2-12 Comparison with Tough2v2

Calculation method	Pressure at x=25, t=1.0E13
ConnectFlow – Crank Nicholson	**-1.0426E7**
ConnectFlow – Gears Method	**-1.0421E7**
Semi analytical	**-1.0438E7**
Tough2	**-1.0423E7**

Both ConnectFlow and Tough2 show the same behaviour relative to the semi analytical solution.

2.7 Seepage Face

2.7.1 Overview

A seepage face is a boundary between the saturated flow field and the atmosphere, along which groundwater discharges. A seepage face is homologous to a free surface boundary condition, so a Dirichlet boundary condition (BC) suffices for its mathematical description, either in terms of hydraulic head h (set to be equal to the elevation z i.e. $h = z$), or in terms of total pressure p (set to atmospheric i.e. $p = 0$). The BC along the ground surface above the upper limit (a point for a 2D models or a line in 3D models) of the seepage face, is usually a Neumann BC (i.e. no flow). The challenge in modelling a seepage face is that its upper extent is unknown during the problem formulation and its determination forms a part of the solution. This verification case considers the steady state radial flow to a well, for which the Dupuit –Forchheimer well discharge formula holds (analytical solution based on the Dupuit assumptions) [xiii].

2.7.2 Problem Definition

A schematic diagram of the problem (segment of a cylinder) is presented in Figure 2-33. In a cylindrical polar coordinate system (r, z), the well axis is aligned with the z axis. A no-flow boundary condition is imposed at the bottom and the top of the model. A far distance head boundary condition (green line) is imposed on the right of the model, setting up the initial height of the water table (i.e. $h = h_\infty$), whilst a fixed head BC ($h = h_w$), is imposed at the bottom of the well (blue line) . Along the side of the well (red line), a seepage face boundary condition is applied. The resulting flow is radially symmetric between the circular equipotential boundaries located at $r = R$ and $r = r_w$.

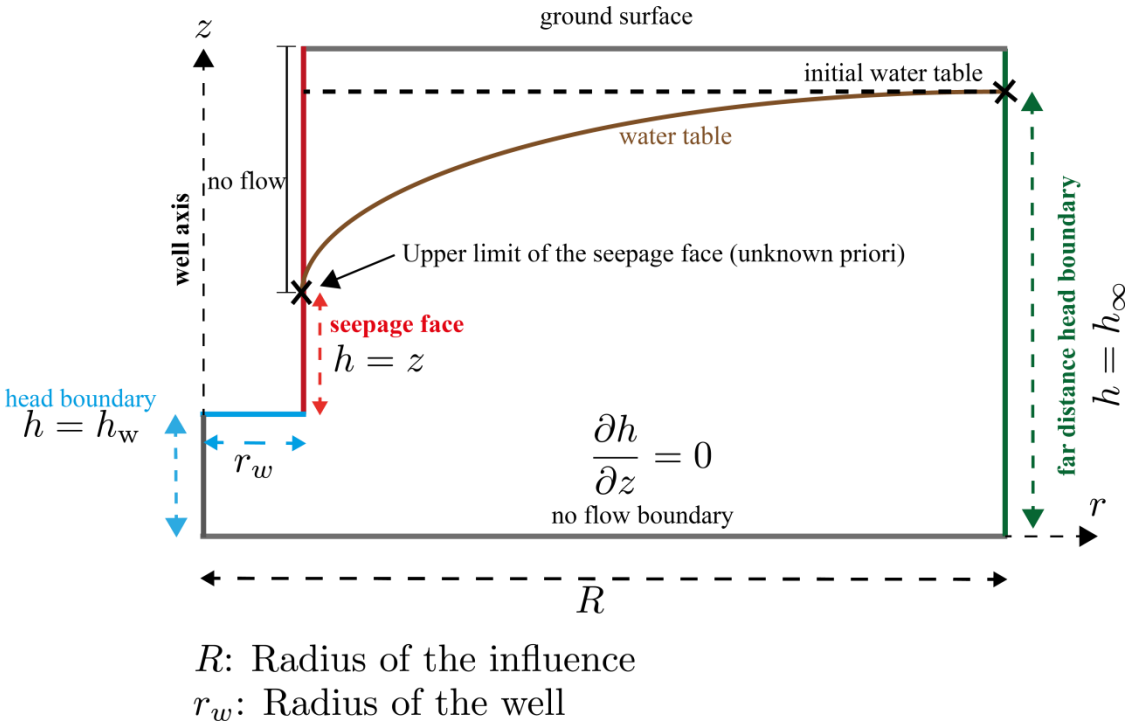

Figure 2-33 Schematic illustration of the conceptual model of a steady state radial flow to a well with a seepage face.

For the above configuration and based on the Dupuit assumptions [xiii] , an analytical expression for the steady volumetric discharge into the well can be derived. This expression known as the Dupuit – Forchheimer well discharge formula, is given as:

$$Q_w = \pi K \frac{h_\infty^2 - h_w^2}{ln\left(R/r_w\right)}. \quad (1)$$

Further, the phreatic surface elevation $h = h(r)$ is given as:

$$h = \sqrt{P(r)}, \text{ where } P(r) = h_w^2 + (h_\infty^2 - h_w^2)\frac{\ln\left(R/r\right)}{\ln\left(R/r_w\right)}. \quad (2)$$

Table 2-13 Input parameters.

Symbol	Parameter	Value
K	Hydraulic conductivity	9.81E-7 m/s
ρ	Density	1000.0 kg/m^3
μ	Viscosity	1.0E-3 Pa.s
h_w	Hydraulic Head at the well	100 m
h_∞	Initial water table	450 m
r_w	Radius of the well	50 m
R	Radius of influence	i)1000 m ii)2000 m iii)3000 m

2.7.3 Variations

2.7.3.1 Volumetric discharge

The first verification test involves the direct comparison of the volumetic flow rates to the well, as obtained by ConnectFlow, to the ones suggested by the Dupuit- Forchheimer well discharge formula. The modelling approach incorporates a thin wedge shaped computational domain in ConnectFlow, which serves as an approximation to the conceptual axissymetric model. Three flow domains are investigated. For each case, only the radius of the domain R is altered (i.e. $R = 1000, 2000, 3000\ [m]$) ,whilst the height of the computational domain, the radius of the well, the head at the elevation of the well and the initial head of the aquifer are kept fixed as, $H = 800[m]$, $r_w = 50[m], h_w = 100[m]$ and $h_\infty = 450[m]$, respectively. The seepage face BC as implemented within ConnectFlow, is applied along the periphery of the well (red line in Figure 2-33). The next task, takes into account the performance of the implemented BC, by investigating how closely the head approximates the elevation along the seepage face, as well as the recovery of the length of the seepage face.

2.7.4 Results

The results in terms of volumetric flow rates (Table 2-14), as obtained by ConnectFlow and the analytical solution (1) are in a good agreement. In particular it can be observed that an increase in the aspect ratio defined as the radius of influence over the radius of the well, results in more accurate prediction.

Table 2-14 Volumetic flow rates to the well, calculated using the Dupuit –Forchheimer formula and ConnecFlow, for different radius of influence.

Radius of the domain	Aspect Ratio R/r_w	Dupuit-Forchheimer m^3/s	ConnectFlow m^3/s	Abosulute Error %
$R = 1000\ [m]$	20	0.1980	0.1672	3.0804
$R = 2000\ [m]$	40	0.1608	0.1472	1.3551
$R = 3000\ [m]$	60	0.1448	0.1378	0.7035

Considering the actual performance of the seepage face BC, it can be observed from Figure 2-34 that along the length of the seepage face (see Table 2-15), the head closely approximates the elevation. The length of the seepage face is shown to be sensitive to the radius of influence, which appears to decrease with an increasing radius of influence. Figure 2-35, portrays the behaviour of the saturation along the boundary of the well, and further supplements the above observation. Clearly the upper extent of the seepage face (position where the flow is fully saturated i.e. $S = 1$), is found to be decreasing with an increasing radius of influence. In Table 2-15, the position of the upper extent of the seepage face is presented, where it is also accompanied by the relative error of the computed head with respect to the actual elevation. Evidently, in all three cases the error is below 1%, suggesting a good approximation (i.e. $h \sim z$) and a satisfactory performance for the BC.

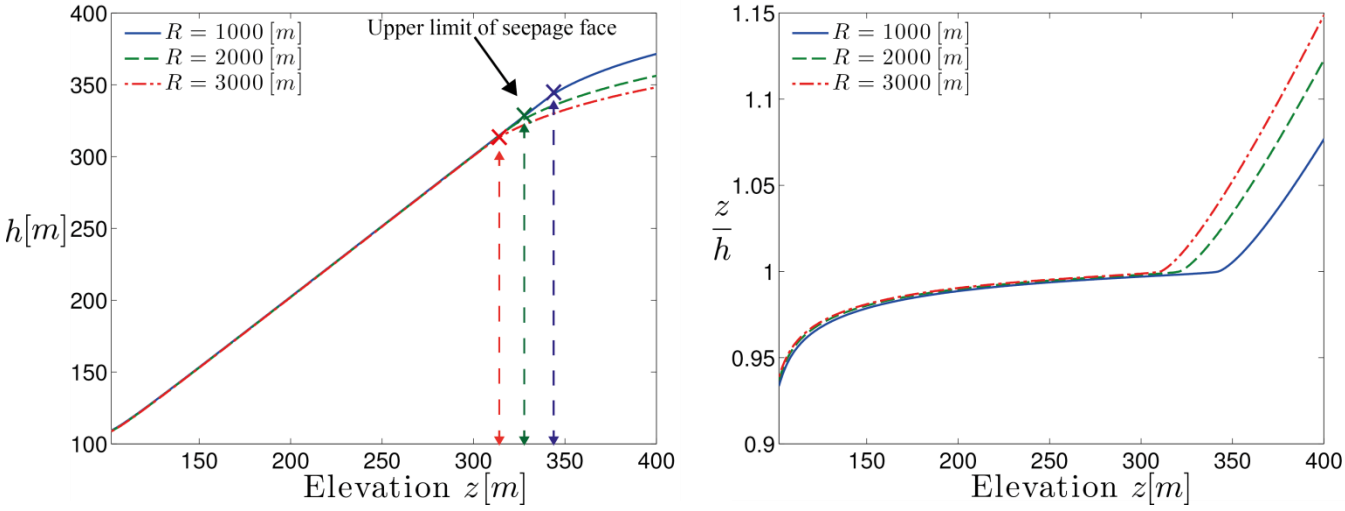

Figure 2-34 On the left graph the Head is plotted as function of the elevation, whilst the figure on the right displays the fraction of the elevation over the head, as function of the elevation.

Table 2-15 The upper extent of the seepage face, its actual length and the mean value of the relative error along the whole extent of the seepage face, measuring the performance of the seepage face BC.

Radius of the domain	Aspect Ratio R/r_w	Upper extent of the seepage face $[m]$	Seepage face length $[m]$	Mean Relative Error $(\frac{h-z}{z})\%$
$R = 1000\ [m]$	20	340	90	0.3348
$R = 2000\ [m]$	40	320	70	0.2888
$R = 3000\ [m]$	60	310	60	0.2641

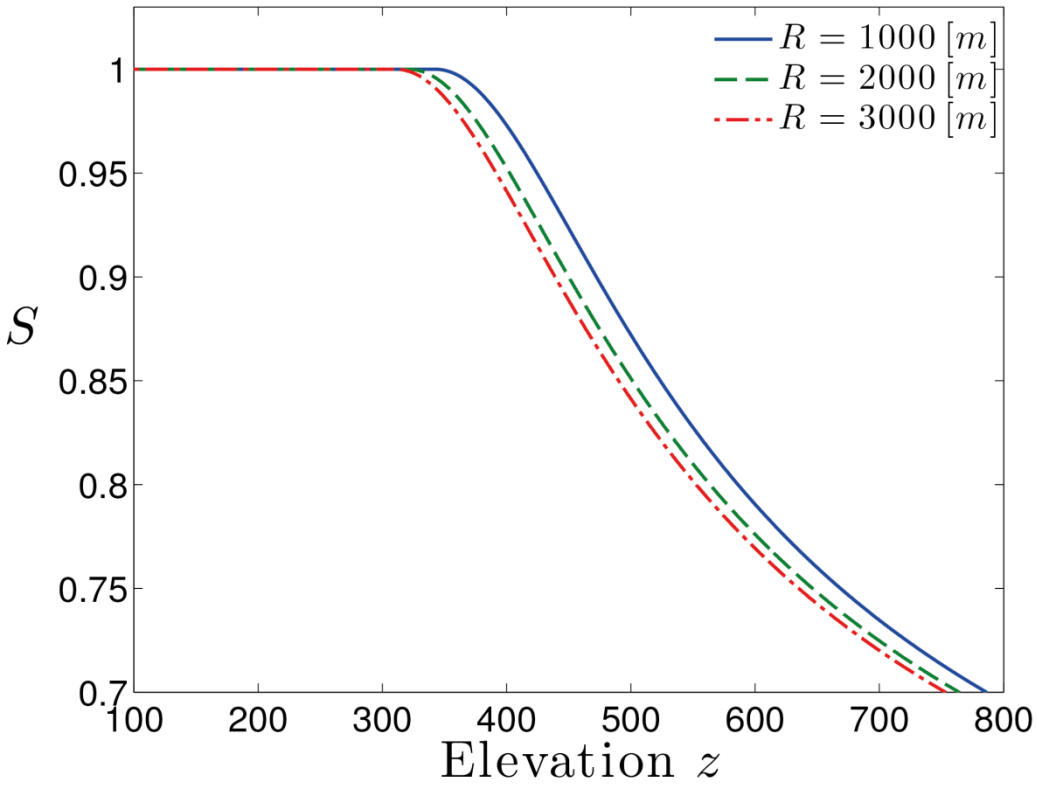

Figure 2-35 Saturation S, along the well boundary is plotted as function of the elevation.

The computed phreatic surfaces obtained for the three flow domains, are grouped and presented, along with the ones obtained after applying the Dupuit-Forchheimer model (see equation 2) are presented in Figure 2-36. It must be noted that within the Dupuit assumptions the seepage face is neglected, and that the analytical approximation is only valid far from the well. As can be seen, the computed phreatic surface closely resembles the one obtained from Dupuit – Forchheimer for increasing values of r. Finally, the cone of depression is found to be decreasing as the radius of influence decreases.

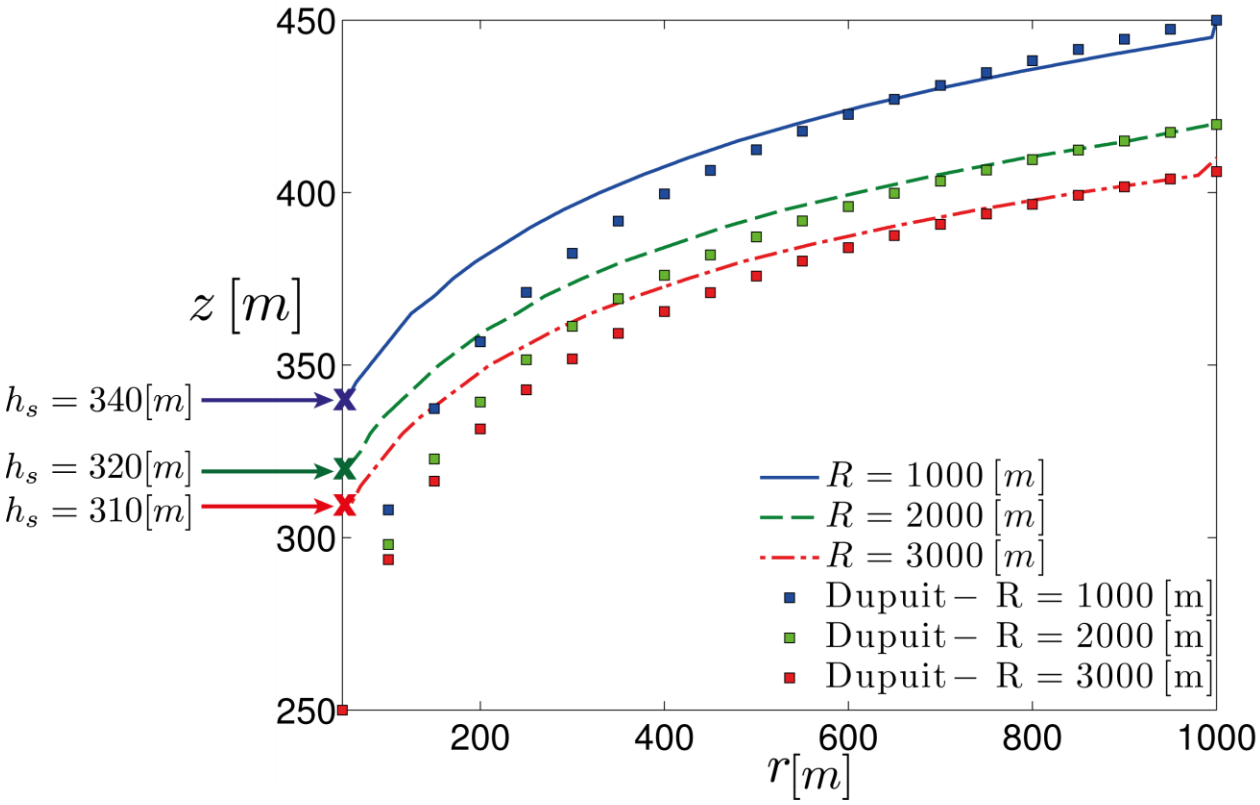

Figure 2-36 Water table position, based on the computations (lines) and the Dupuit Forchheimer model (squares).

2.8 Henry's Salt Transport

2.8.1 Overview

This case considers salt water intrusion into a vertical slice of an isotropic homogeneous confined aquifer.

The variant modelled is a modified version of the original Henry's test case, as recommended in [xiv]. The modified case halves the fresh water inflow rate, which increases the sensitivity of the solution to the variation in density.

2.8.2 Problem Definition

A schematic of the test case is shown in Figure 2-37 and the input parameters are given in Table 2-16.

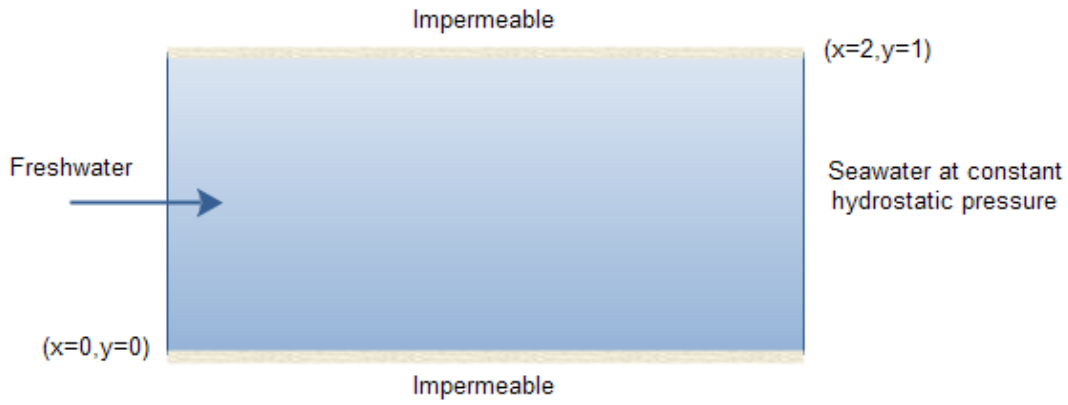

Figure 2-37 Henry's Problem

A uniform hexahedral grid was used of size 80x40 elements.

Table 2-16 Input parameters

Symbol	Parameter	Value
K	Hydraulic conductivity of rock	**1.0E-2 m/s**
D	Coefficient of molecular diffusion	**1.886E-5 m^2/s**
Q	Freshwater inflow per unit depth	**3.3E-5 m^2/s**
ρ_0	Reference density	**998 kg/m^3**
ρ_{max}	Saltwater density	**1023 kg/m^3**
α_L	Longitudinal dispersivity	**0 m**
α_T	Transverse dispersivity	**0 m**
ϕ	Porosity	**0.35**

The model makes use of the ConnectFlow "reference waters" capability which allows fluids with different properties to be defined. The steady solution is obtained by running a transient solution until the steady state is reached.

2.8.3 Results

The test case has an analytical solution, represented by an infinite double Fourier series. A truncated form of the series gives a non-linear system which can then be iteratively solved. Results from this process are reported in [xiv] and these are used for the comparisons in Figure 2-38. The maximum error in contour location is less than 3%.

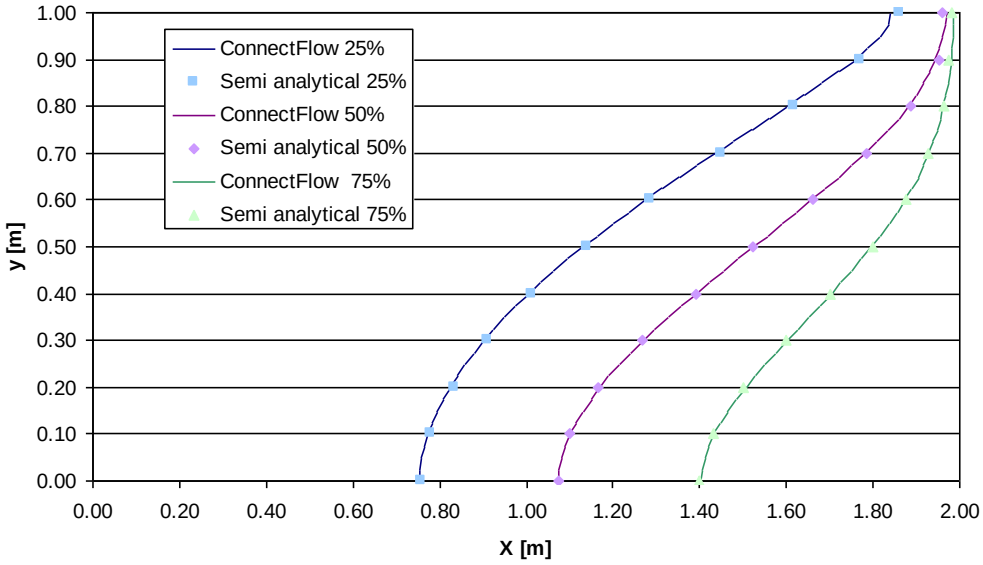

Figure 2-38 Non-dimensional concentration of salinity

2.9 1D Rock Matrix Diffusion (RMD)

2.9.1 Overview

This case considers the transient one dimensional transport of salinity through fractured rock where diffusion between the fractured rock and the adjacent rock matrix is modelled. This test case assumes a constant density.

The test case is taken from the SKB R-04-78 report [xv] and has a semi-analytical solution.

2.9.2 Problem Definition

Figure 2-39 depicts the modelled 1D domain.

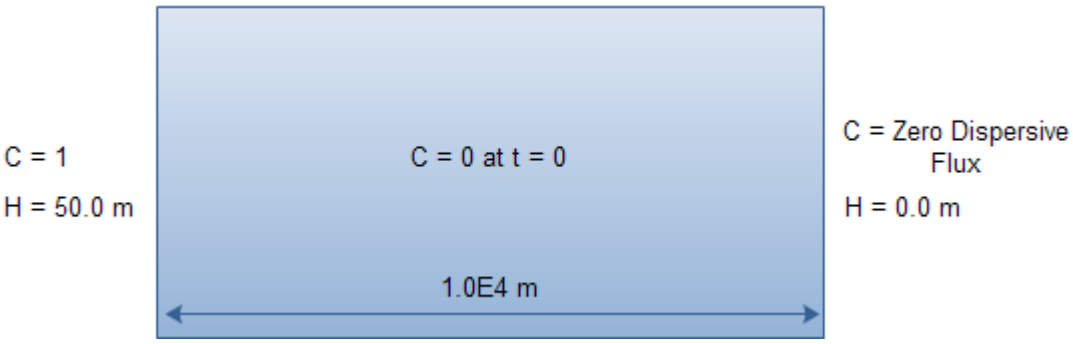

Figure 2-39 Schematic of problem definition

Table 2-17 Input parameters

Symbol	Parameter	Value
K	Rock permeability	**1.0E-11 m^2**
D	Salt diffusion coefficient	**1.0E-9 m^2/s**
ρ	Density	**998.3 kg/m^3**
ρ_{max}	Saltwater density	**998.3 kg/m^3**
α_L	Longitudinal dispersivity	**100 m**
α_T	Transverse dispersivity	**10 m**
ϕ	Fracture porosity	**0.01**
μ	Viscosity	**1.0E-3 Pa.s**
τ	Tortuosity	**1.0**
ϕ_m	Matrix porosity	**0.3**
D_i	Intrinsic diffusion coefficient	**5.0E-11 m^2/s**
σ	Fracture surface area per unit volume.	**2 m^{-1}**

In this case the rock matrix diffusion slows down the increase in salinity in the fractured rock, as a proportion of the salinity is diffusing into the surrounding rock matrix. The time taken for the mid-point relative concentration to reach 0.99 is increased by more than a factor 10 due to RMD.

2.9.3 Variations

2.9.3.1 Crank Nicholson

In this variation the non-linear system is solved using Newton iteration on each time step for all variables as a single group. Automatic time stepping is used to gradually increase the time step size from its initial value of 1.0E6 seconds.

2.9.3.2 Sequential Inner Iteration

Sequential inner iteration solves the non-linear system of equations that arise at each time step according to a user-specified sequence of Newton iterations on subgroups of the full system of equations. In this test the pressure field is time independent, so just the salt concentration is solved for.

This setup also uses nodal quadrature in order to allow an optimized fast equation assembly process. Both the fast assembly and normal assembly were tested.

Automatic time stepping is used to gradually increase the time step size from its initial value of 1.0E6 seconds.

2.9.3.3 Increased Salt Diffusion Coefficient

The effective dispersion of concentration is given by

$$\varphi\rho(\frac{D}{\tau}+\alpha_L v)$$

Where v is the pore water velocity in the fractured rock, which for this case has a constant value of 4.981E-5 m/s. This means that $\frac{D}{\tau}$ = 1.0E-9 and $\alpha_L v$ = 4.981E-3.

This variation sets the dispersion length α_L to zero, and the salt diffusion coefficient D to 4.981E-3. This results in a modified test with the same effective diffusion and hence the same semi-analytical solution.

2.9.3.4 Finite Volume RMD

This variant uses the alternative finite volume RMD method in ConnectFlow that provides an explicit discretisation of the rock matrix into a 1D column of cells at each solution node in the model. The discretisation is specified by the user, e.g. Figure 2-40. This method provides computational efficiency with reasonable accuracy for a given level of refinement. Unlike the original RMD method, this method is compatible with reactive transport. The model used for verification is the same as the base case, but with a matrix porosity of 0.3.

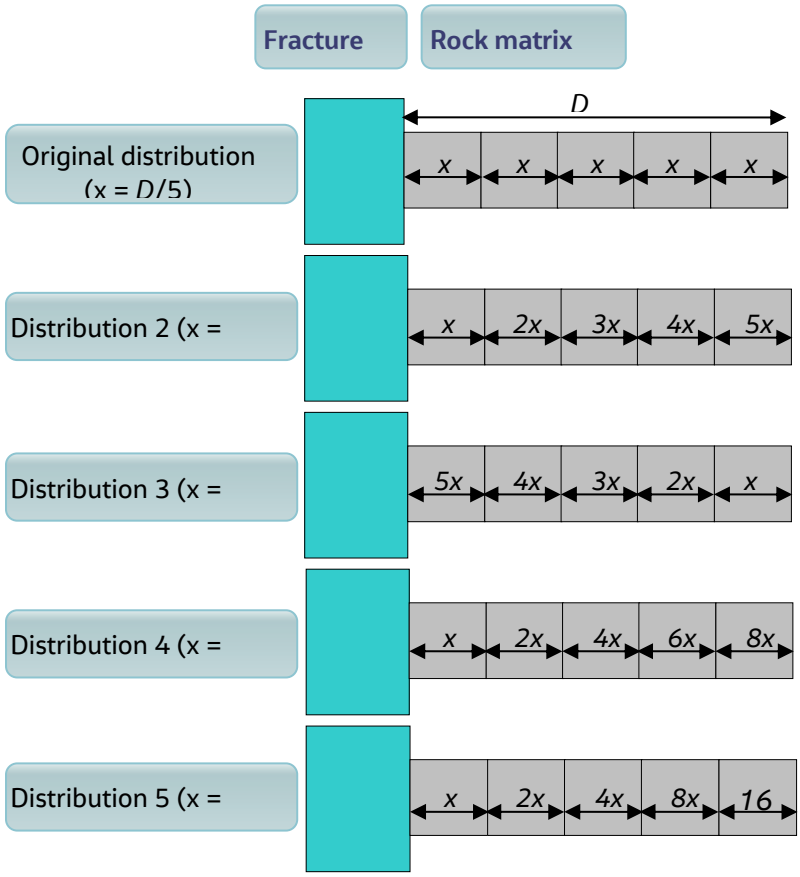

Figure 2-40 Schematic of the distribution of cell sizes in the rock matrix.

2.9.4 Results

The semi-analytical solution is derived using Laplace transforms, which are then inverted numerically. The details of this process are covered in [xv].

The results show good agreement with the semi-analytical solution, the ConnectFlow concentrations being within 1% of the semi-analytical solution for all variations. The concentration profiles for three time values are shown in Figure 2-41.

The results for the finite volume RMD method are shown in Figure 2-42 to Figure 2-44. There is good agreement with the analytical solution, but accuracy increases as the cell sizes closest to the fracture decrease in size, either due to an increase in the number of cells or by using a distribution that increases in cell size with distance from the fracture.

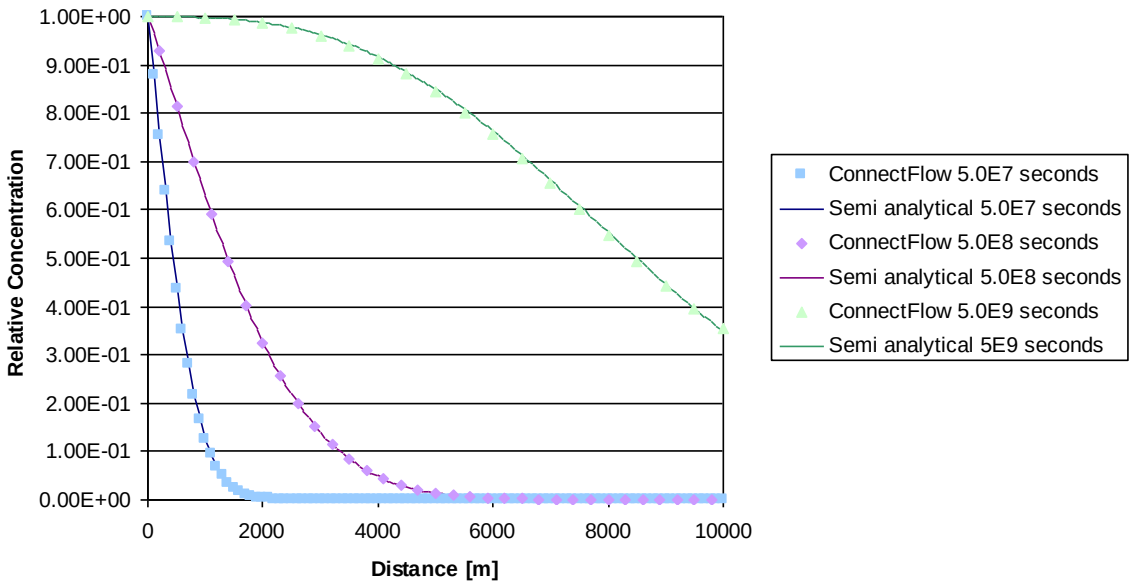

Figure 2-41 Crank Nicholson - Relative concentration

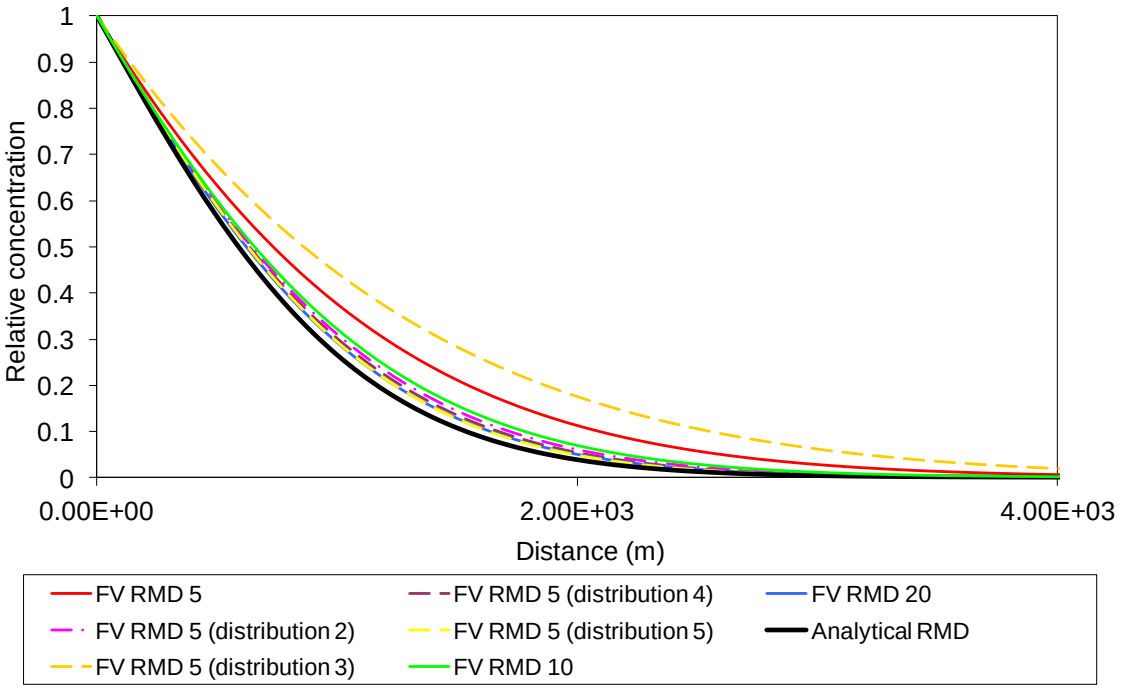

Figure 2-42 Relative concentration along the column at time t=1.0·108 s, using finite volume (FV) rock matrix diffusion (RMD) with varying number of matrix cells and different cell sizes compared to an analytical solution.

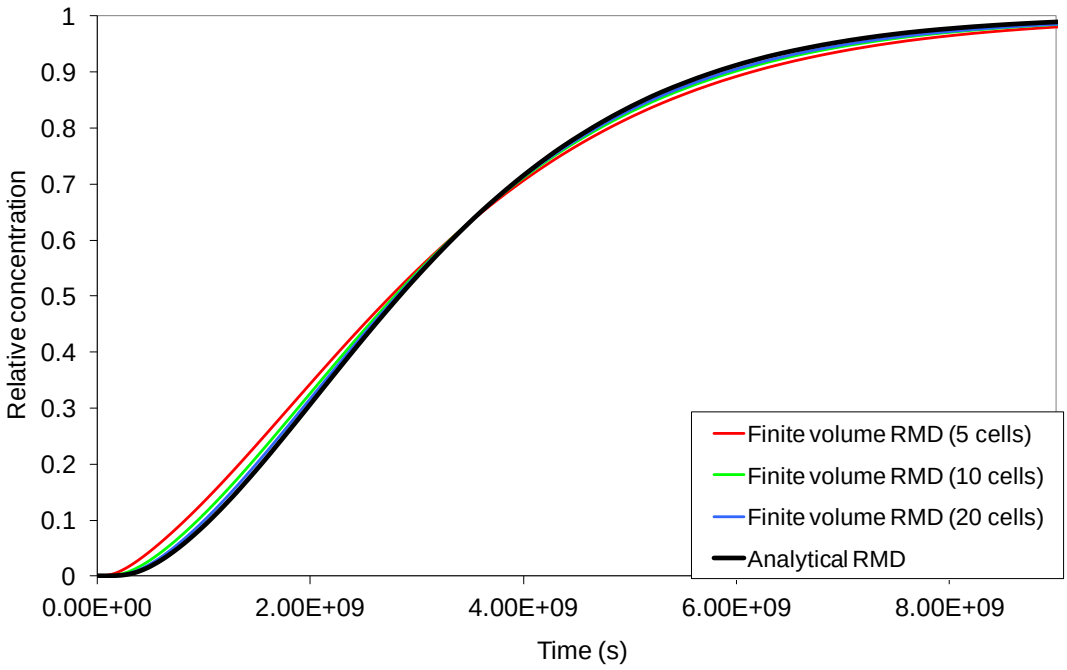

Figure 2-43 Relative fracture water concentration midway along the column against time, using finite volume rock matrix diffusion with varying number of rock matrix cells compared to an analytical solution.

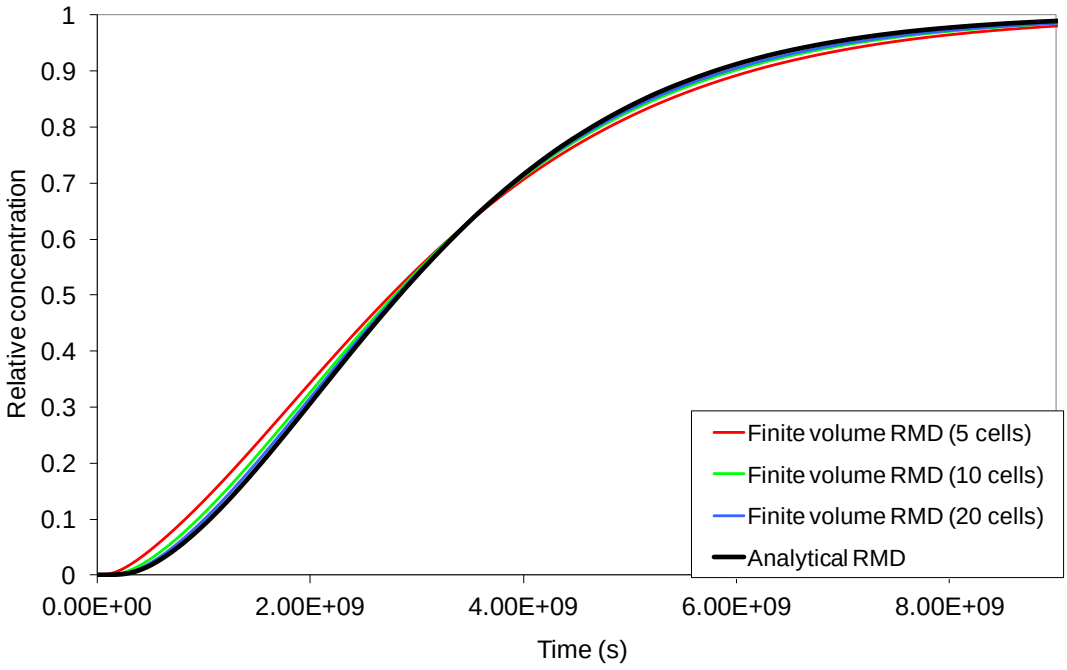

Figure 2-44 Relative fracture water concentration midway along the column against time, using finite volume rock matrix diffusion with varying number of rock matrix cells compared to an analytical solution.

2.10 1D Nuclide Transport with Sorption and Decay

2.10.1 Overview

This case considers transient one-dimensional nuclide transport due to advection and diffusion. Both sorption and decay are considered.

The test case is taken from [xvi] and has an analytical solution.

2.10.2 Problem Definition

Figure 2-39 depicts the modelled 1D domain.

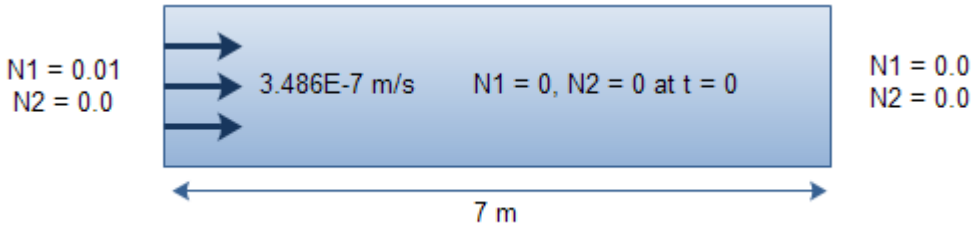

Figure 2-45 Schematic illustration of the problem definition

Table 2-18 Input parameters

Symbol	Parameter	Value
k	Rock permeability	**1.24E-9 m^2**
U	Darcy velocity	**3.486E-7 m/s**
D	Nuclide diffusion coefficient	**1.162E-7m^2/s**
α_L	Longitudinal dispersivity	**0 m**
α_T	Transverse dispersivity	**0 m**
R_{n1}	Retardation factor nuclide 1	**2.0**
R_{n2}	Retardation factor nuclide 2	**1.0**
λ_{n1}	Decay constant nuclide 1	**4.011E-7 1/s**
λ_{n2}	Decay constant nuclide 2	**1.0E-20 1/s**
τ	Tortuousity	**1.0**
ρ	Density	**1000.0 kg/m^3**
μ	Viscosity	**1.0E-3 Pa.s**
ϕ	Porosity	**0.3**

Constant pressure boundary conditions are applied to generate the desired Darcy velocity. The timescale modelled is 20 days which also corresponds to the half life of the parent nuclide N1.

The mesh consists of 100 CB08 elements along the length of the flow domain, and the time step is taken to be 1E4 seconds.

2.10.3 Variations

2.10.3.1 Fast Linear Transport

Four runs are carried out to illustrate the effect of sorption and decay on the solution.

- No decay or sorption
- Sorption only
- Decay only
- Sorption and decay

2.10.3.2 Crank Nicholson

This variation repeats the sorption and decay case using the Crank Nicholson transient solver.

2.10.4 Results

The results show excellent agreement with the analytical solution [xvii]. The concentration of the parent nuclide N1 is compared with the analytical solution for each of the four fast linear transport runs in Figure 2-46, Figure 2-47, Figure 2-48 and Figure 2-49.

The Crank Nicholson results were very close to the Fast Transient results, with the peak daughter nuclide concentration being 1% higher and the parent nuclide concentration being identical.

Figure 2-50 shows the ConnectFlow daughter nuclide N2 concentration for the sorption and decay case.

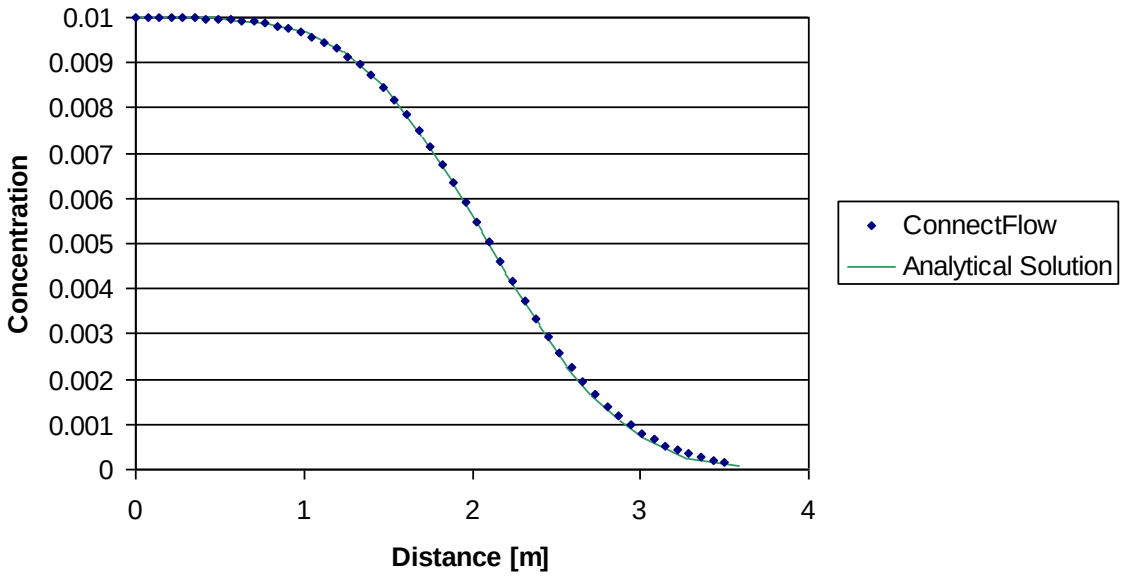

Figure 2-46 N1 concentration with no sorption or decay

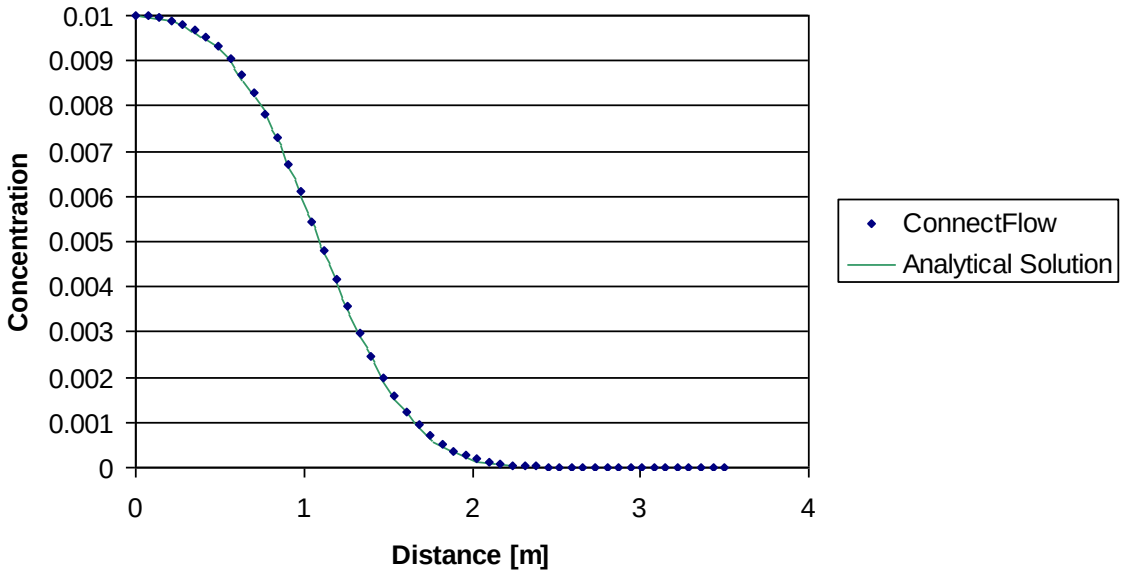

Figure 2-47 N1 concentration with sorption only

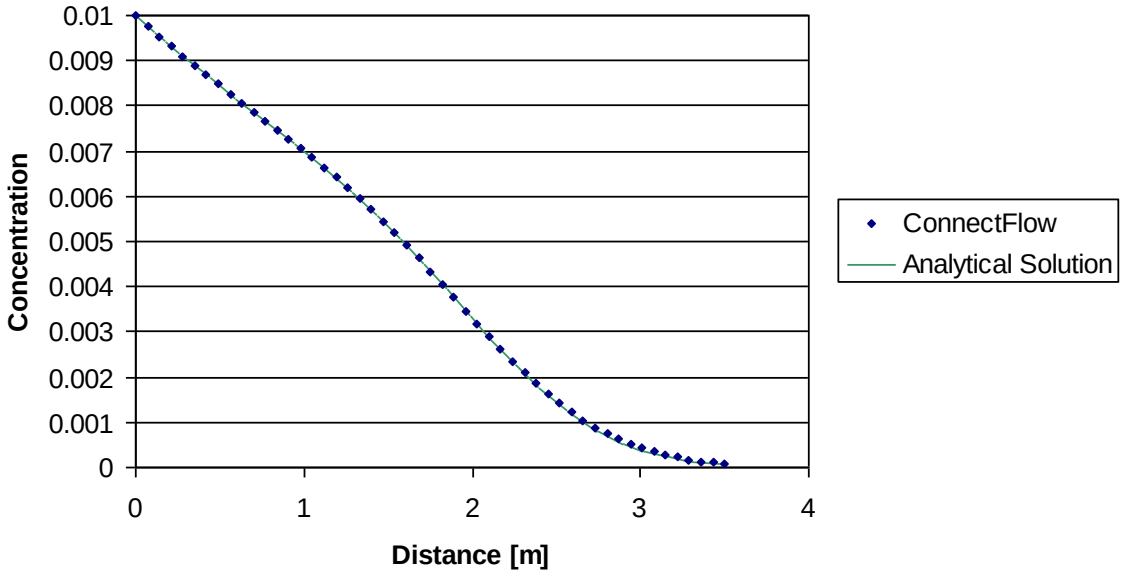

Figure 2-48 N1 concentration with decay only

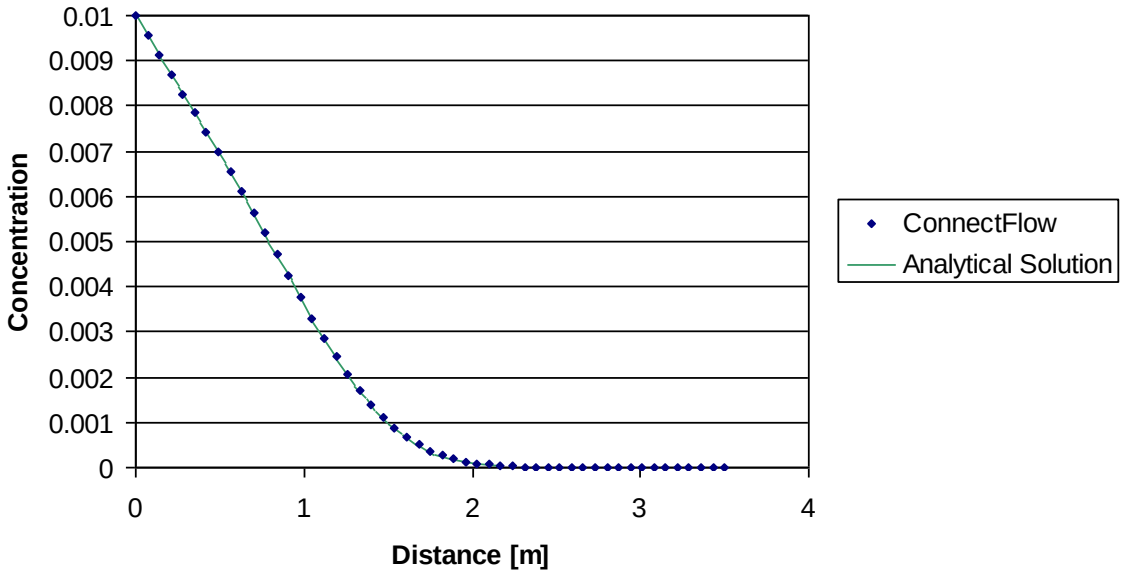

Figure 2-49 N1 concentration with both sorption and decay

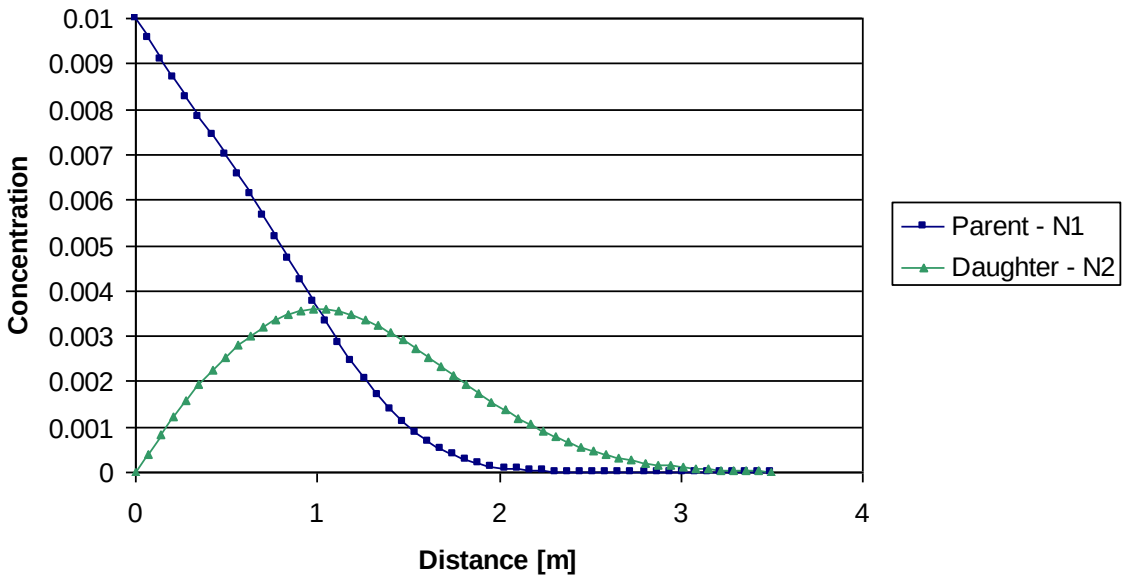

Figure 2-50 Parent and daughter concentrations for the sorption and decay case

2.11 Mass Flux Calculations

2.11.1 Overview

The mass conserving algorithm was originally implemented in ConnectFlow for particle tracking calculations. The fluxes generated during particle tracking are useful in their own right for calculating the flux passing through a particular region of a CPM model. This verification case compares a flux calculation using the mass conserving algorithm with an analytic solution to the same problem.

2.11.2 Problem Definition

Consider the following 3D CPM model,

- A regular mesh of 4 layers of 16 x 16 cuboidal (CB08) finite elements, oriented parallel to the x-y plane. The dimensions of each finite element are 100 m x 100 m x 100 m giving a model with dimensions 1600 m in the x and y directions and 400 m in the z direction.
- The finite elements consist of rock 1 with permeability $1x10^{-14}$ m^2 except for a vertical column of 64 finite elements (4 layers of 4 x 4) which consist of rock 2 with permeability $1x10^{-12}$ m^2 (see Figure 2-51).
- Pressure (Dirichlet) boundary conditions are applied to the top (z=400 m) and bottom (z=0 m) of the model and no-flow boundary conditions are applied to the other sides of the model. These provide a pressure gradient along the z-axis of 250 N/m.

The symmetry of the problem allows an analytic solution to the flow through each finite element using the following expression

$$F = \frac{k}{\mu}\frac{dp}{dz}A\rho$$

where

A is the area = 10,000 m^2.

k is the permeability

μ is the viscosity = 0.001 Ns/m^2

ρ is the density = 1000 kg/m^3

dp/dz is the pressure gradient = 250 N/m.

F is the mass flux through the element.

Thus the vertical flux through the finite elements of rock type 2 is 2.5 kg/s and the vertical flux through each of the other finite elements is 0.025 kg/s. The total flux through all of the elements in each layer is then 43.6 kg/s.

2.11.3 Results

Using the command, >> CALCULATE CONSERVED MASS FLUX, ConnectFlow recreates the analytic solution to this problem exactly.

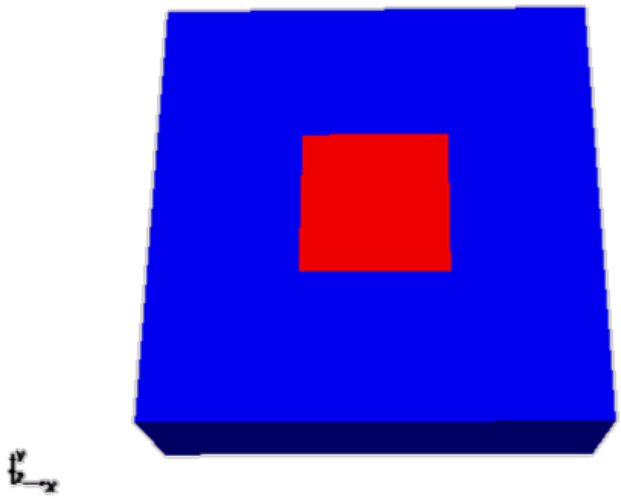

Figure 2-51 The rock types used for the mass flux verification test. Red represents rock type 2 and blue denotes rock type 1. Note that the rock types are constant along the z-axis.

2.12 Reactive Transport

2.12.1 Overview

This case considers transient one-dimensional, multi-component reactive transport due to advection and chemical reactions [xviii]. The results are compared with equivalent calculations carried out by Phast [xix] and contrasted with ConnectFlow calculations without reactions included.

2.12.2 Problem Definition

For each case, a horizontal column, 10 m in length and 1 m in width and height, of grid cells is considered, as shown in Figure 2-52. The grid is discretised into cells that are 0.05 m in each dimension, giving 80,000 cells in total. The properties used are given in Table 2-19. Note that the spatial discretisation schemes used by Phast leads to numerical dispersion equal to half the cell size and therefore it is necessary to take this into account when setting the dispersion lengths, although it is a small effect relative to the diffusion in these cases. The dispersion length in Table 2-19 includes this numerical dispersion. The fluid density is held constant and is uniform across the model.

The column is initially filled with a water (aqueous solution) in equilibrium with one or more mineral phases. Then a second water with a different composition is introduced at the upstream end of the column and allowed to flow advectively into it. The flow is specified as a flux boundary condition at the inflow end of the model and a zero pressure boundary condition at the outflow end, which also has an outflow (zero dispersive flux) boundary condition to allow the solutes to flow advectively from the model. The advective transport velocity is 0.1 m/y and the simulation is run for 120 years, allowing more than sufficient time for the incoming water to be advectively transported along the full length of the column, although dispersion and diffusion processes will cause some spreading out of the front. All concentrations are represented as mass fractions in kilograms per kilogram of solution (kg/kg_s).

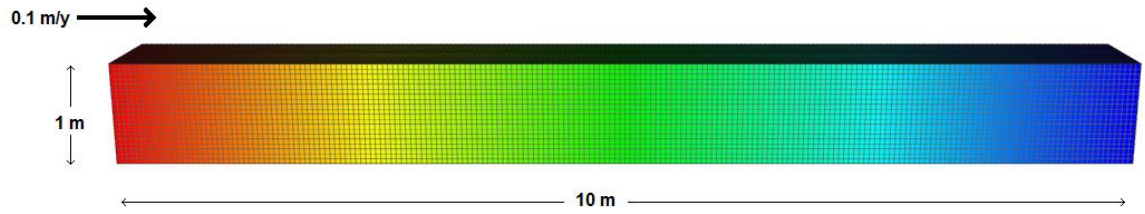

Figure 2-52 Column model used for verification of reactive transport, coloured by head.

Table 2-19 Input parameters for reactive transport verification.

Symbol	Parameter	Value
k	Rock permeability	**1.0E-17 m^2**
ϕ	Porosity	**1.0E-4**
D	Solute diffusion coefficient	**1.0E-9 m^2/s**
α_L	Longitudinal dispersion length	**0.05 m**
α_T	Transverse dispersion length	**0.05 m**
T	Temperature	**25 °C**
μ	Fluid viscosity	**1.0E-3 Pa.s**
ρ	Fluid density	**1.0E3 kg/m^3**
U	Darcy velocity	**1.0E-5 m/y**
dt	Time step size	**1.0 y**
nt	Number of time steps	**120**

2.12.3 Variations

2.12.3.1 Mineral Equilibration

This variant considers equilibration of a mixture of pure water and an oxygenated saline water with calcite and pyrite. It provides an example of a redox reaction. The following reactions are significant for calcite dissolution/precipitation and the oxidation of iron (II) and sulphide in pyrite to iron(III) and sulphate:

$$CaCO_3 \leftrightarrow Ca^{2+} + CO_3^{2-} \quad (2\text{-}1)$$

$$HCO_3 \leftrightarrow H^+ + CO_3^{2-} \quad (2\text{-}2)$$

$$4FeS_2 + 14O_2 + 4H_2O \leftrightarrow 4Fe^{2+} + 8SO_4^{2-} + 8H^+ \quad (2\text{-}3)$$

$$4Fe^{2+} + O_2 + 4H^+ \leftrightarrow 4Fe^{3+} + 2H_2O \quad (2\text{-}4)$$

Equilibration with CO_2(g) has not been considered. Both the calcite and pyrite are present in the model with a sufficient initial quantity (10.0 mol/kg$_w$) such that they will not be depleted. The compositions of the waters are given in Table 2-20. The column is initially filled with pure water that has been equilibrated with calcite and pyrite and the saline water is introduced to the upstream end. Both waters are charge balanced by adjusting the chloride mass fraction and pre-equilibrated with calcite and pyrite. The standard phreeqc.dat thermodynamic database is used.

Table 2-20 Water composition for calcite and pyrite equilibration.

	Saline water	Pure water
pH	7.00	7.00
pe	13.00	4.00
Component mass fractions (kg/kg_s)		
C	0.00	0.00
Ca	0.00	0.00
Cl	3.55E-5	0.00
Fe	0.00	0.00
Na	2.30E-5	0.00
S	0.00	0.00

2.12.3.2 Ion Exchange

This variant considers the reaction of a mixture of two aqueous solutions and an ion exchanger that is able to exchange cations. The reactions are defined in the standard phreeqc.dat thermodynamic database, using the example exchanger 'X'. The model initially contains a sodium chloride (NaCl) solution, with a small amount of potassium, and a calcium chloride ($CaCl_2$) solution is introduced at the upstream end of the column. The composition of the waters is given in Table 2-21. The column also contains the ion exchanger X with an initial quantity of 0.011 moles per kilogram of water (mol/kg_w), whose composition is initialised by equilibrium with the NaCl water.

Table 2-21 Water composition for ion exchange.

	$CaCl_2$ water	NaCl water
pH	7.00	7.00
pe	4.00	4.00
Component mass fractions (kg/kg_s)		
Ca	2.40E-4	0.00
Cl	4.25E-4	3.90E-4
K	0.00	3.91E-5
Na	0.00	2.30E-4

2.12.3.3 Kinetic dissolution of K-feldspar

This variant considers the dissolution of K-feldspar, which is a slow process and so does not tend to reach equilibrium under the timescales of interest. Therefore, it is appropriate to model this reaction using a kinetic approach. The reactions are defined in the standard phreeqc.dat thermodynamic database as follows:

$$KAlSi_3O_8 + 8H_2O \rightarrow K^+ + Al(OH)_4^- + 3H_4SiO_4 \quad (2\text{-}5)$$

The model initially contains a saline solution and a dilute acidic solution is introduced at the upstream end of the column. The composition of the waters is given in Table 2-22. There is a uniform initial quantity of 0.02 moles of K-feldspar per kilogram of water in the model. The kinetic parameters are given in Table 2-23. The rate expressions are contained in the thermodynamic database.

Table 2-22 Water composition for K-feldspar dissolution.

	Dilute water	Saline water
pH	4.00	7.00
pe	4.00	4.00
Component mass fractions (kg/kg_s)		
Al	0.00	1.17E-6
Cl	3.09E-6	3.08E-3
K	0.00	1.69E-6
Na	2.00E-6	2.00E-3
Si	0.00	3.64E-6

Table 2-23 Kinetic parameters for K-feldspar dissolution.

Parameter	Value
Time step subdivision	**10**
Runge-Kutta subintervals	**3**
P_1	**1.36E4 dm^{-1}**
P_2	**0.1**
Tolerance	**1.0E-8**

2.12.4 Results

2.12.4.1 Mineral Equilibration

Figure 2-53 shows the mass fraction profiles for iron. Iron is not present in the initial waters, hence there are no plots for the ConnectFlow case without chemistry. However, iron is produced in solution during the oxidation of pyrite by the oxygenated inflowing saline water. ConnectFlow and Phast are in excellent agreement in the calculation of the total amount of iron in solution. Figure 2-54 shows the mass fraction profiles for sulphate, again showing very good agreement between Phast and ConnectFlow. They are also in good agreement for the calculated pe values (a measure of the redox conditions), as shown in Figure 2-55.

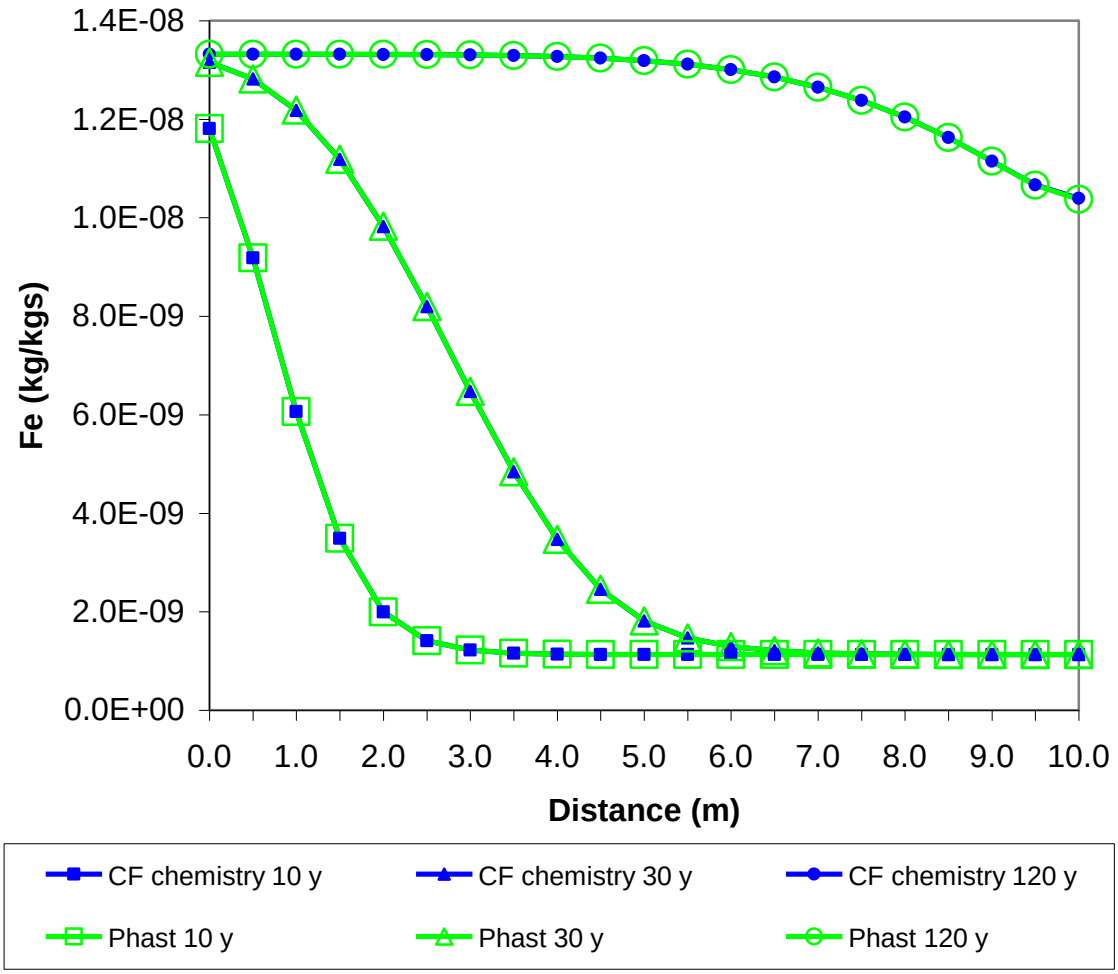

Figure 2-53 Comparison of mass fraction profiles of iron for the calcite and pyrite equilibration case between ConnectFlow (CF) and Phast. Mass fractions are sampled at 0.5 m intervals along the model column.

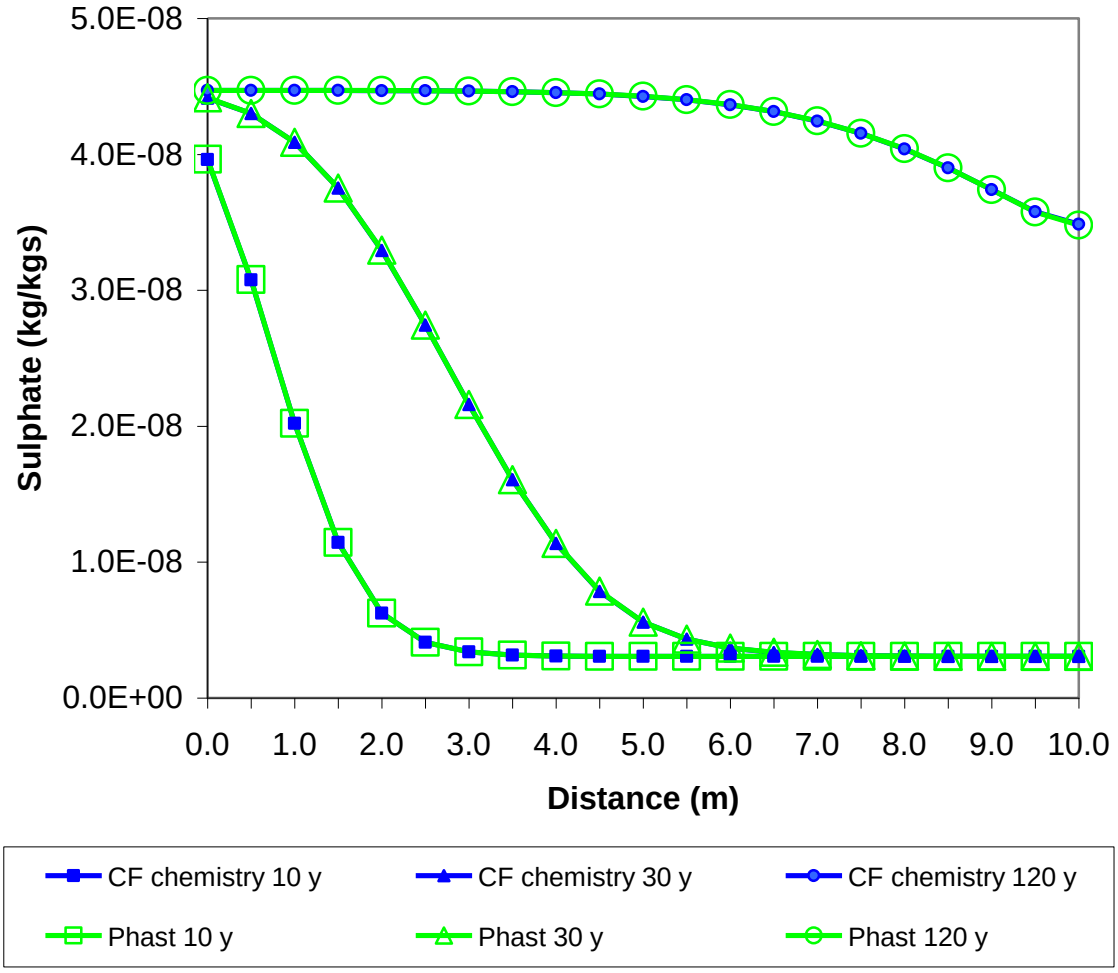

Figure 2-54 Comparison of mass fraction profiles of sulphate for the calcite and pyrite equilibration case between ConnectFlow (CF) and Phast. Mass fractions are sampled at 0.5 m intervals along the model column.

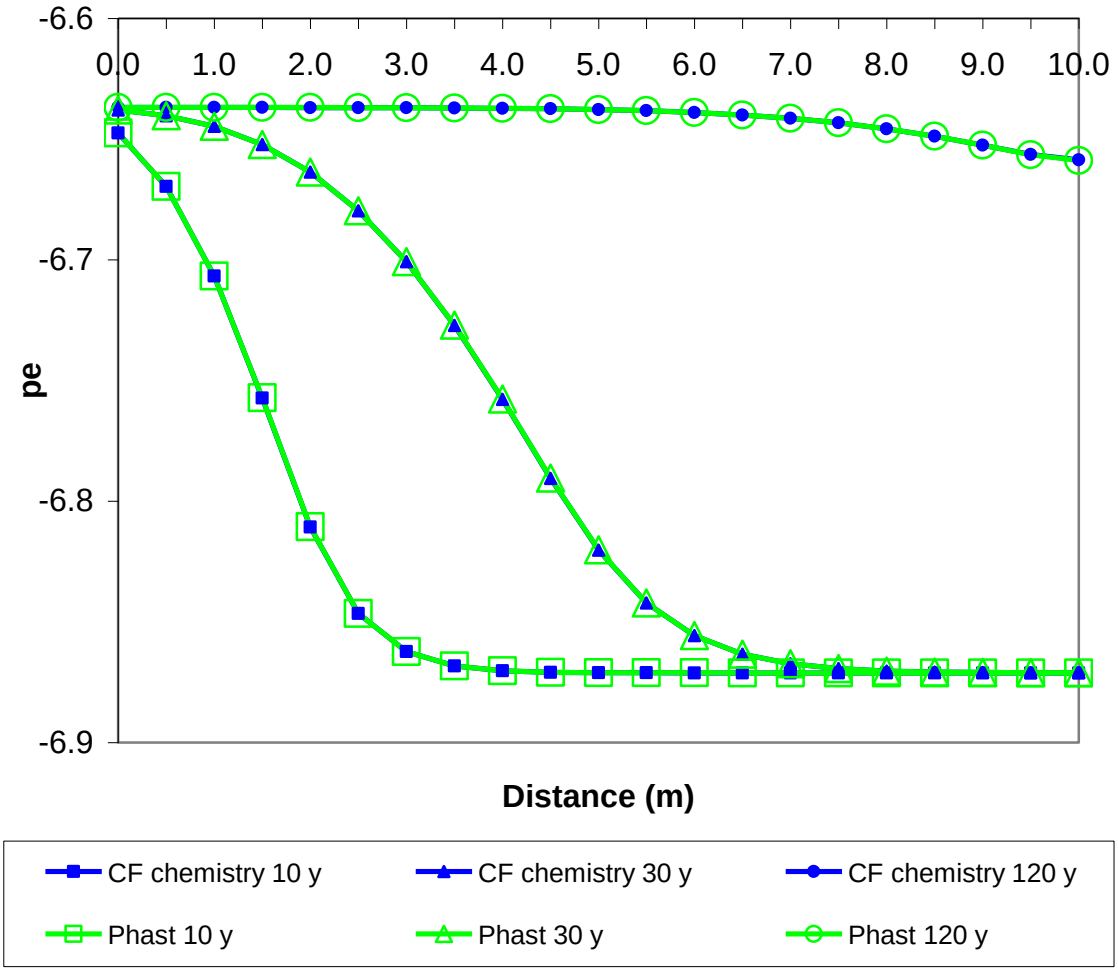

Figure 2-55 Comparison of pe profiles for the calcite and pyrite equilibration case between ConnectFlow (CF) and Phast. Values are sampled at 0.5 m intervals along the model column.

2.12.4.2 Ion Exchange

Figure 2-56 shows the mass fraction profiles of chloride for three different times. This is a non-reactive component and there is good agreement between ConnectFlow (with and without chemistry) and Phast, showing that the transport is equivalent in each calculation. Figure 2-57 shows the mass fraction profiles for calcium. This is not present in solution initially in the model, but as it is introduced in the CaCl2 water its mass fraction rises with time. However, its mass fraction is reduced compared to the ConnectFlow case without chemistry calculations because the calcium ions are taken up by the ion exchanger, which releases sodium and potassium ions as a consequence. The corresponding profiles for calcium in the exchanger are shown in Figure 2-58. There is excellent agreement between the results for ConnectFlow and Phast.

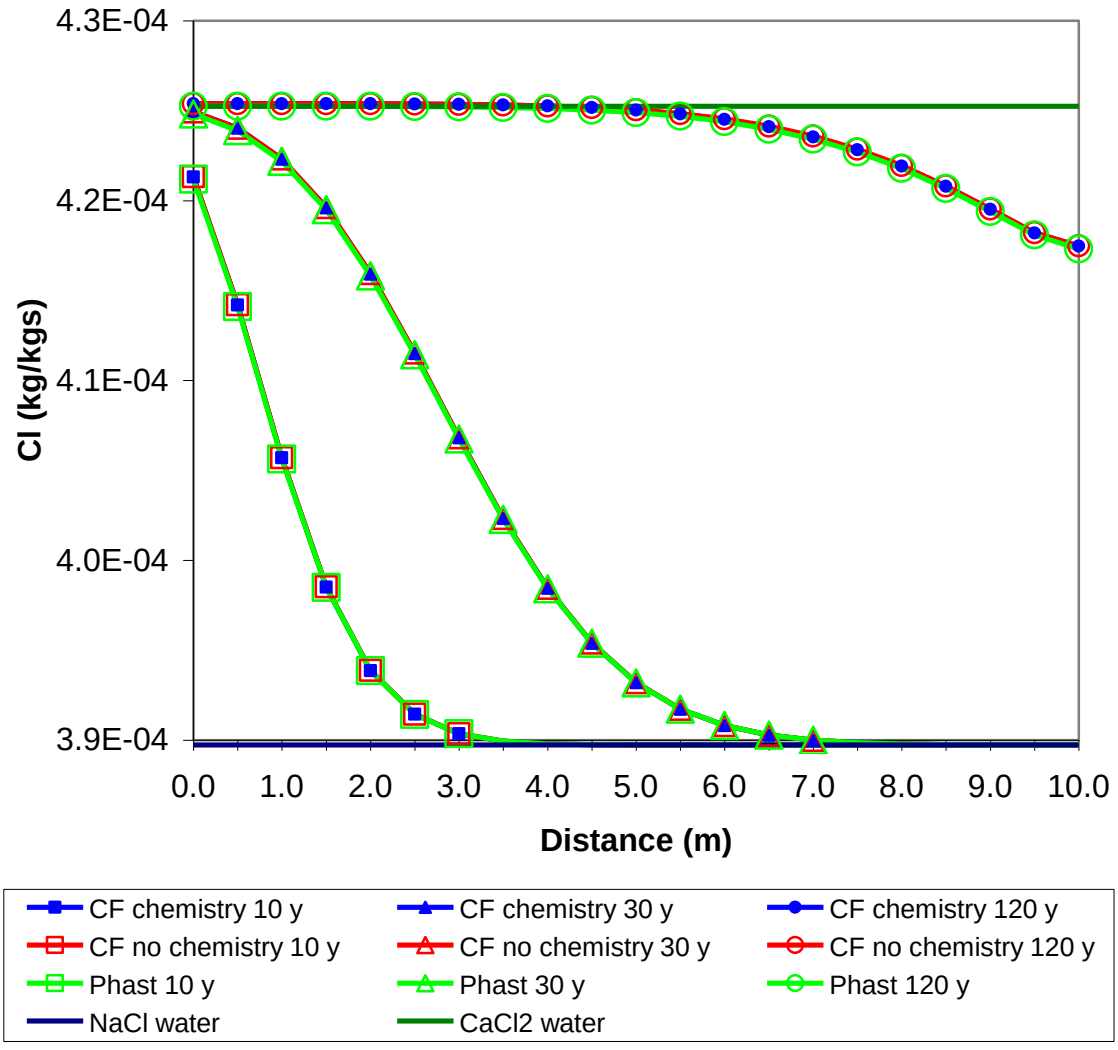

Figure 2-56 Comparison of mass fraction profiles of chloride for the ion exchange case between ConnectFlow (CF), with and without chemistry, and Phast. Mass fractions are sampled at 0.5 m intervals along the model column.

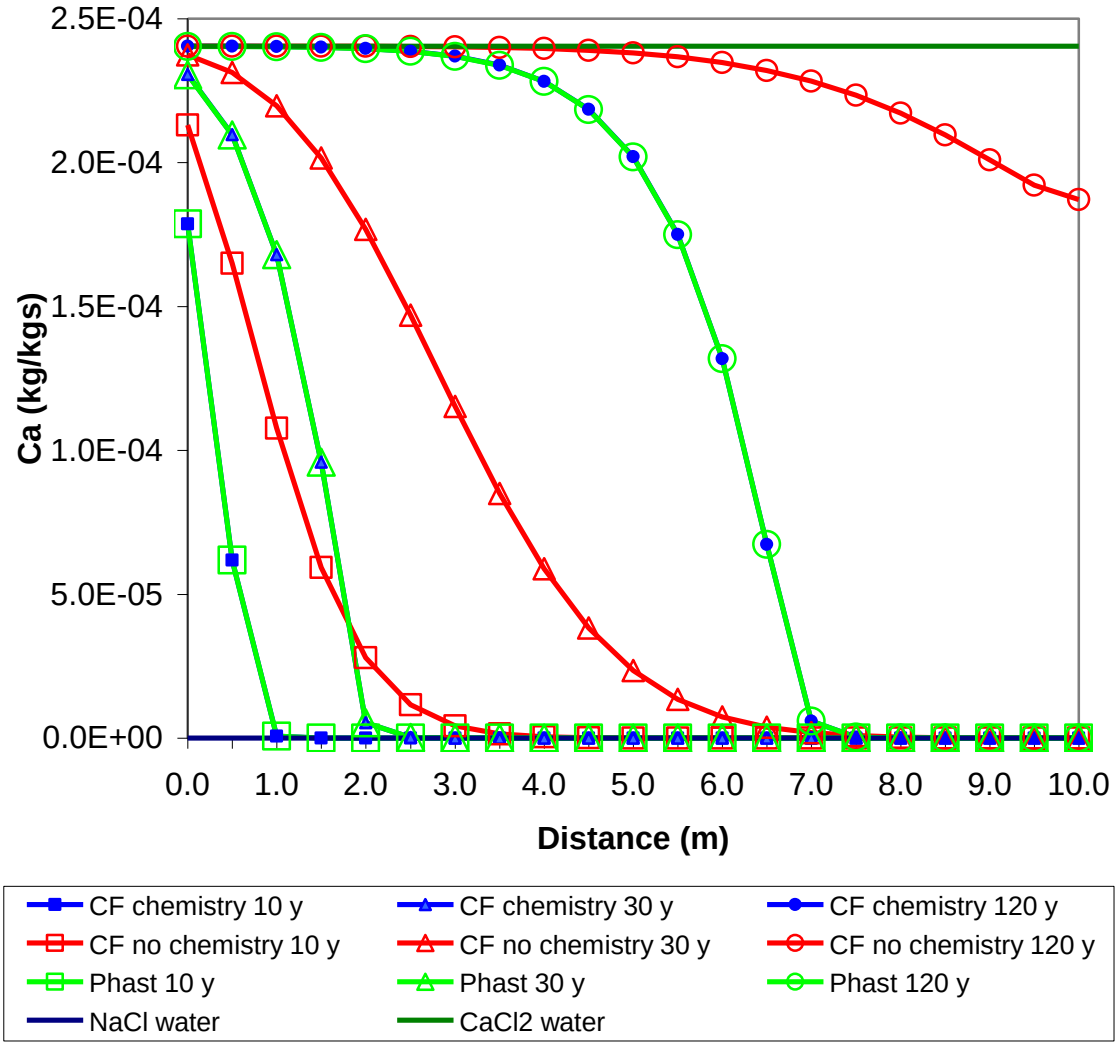

Figure 2-57 Comparison of mass fraction profiles of calcium for the ion exchange case between ConnectFlow (CF), with and without chemistry, and Phast. Mass fractions are sampled at 0.5 m intervals along the model column.

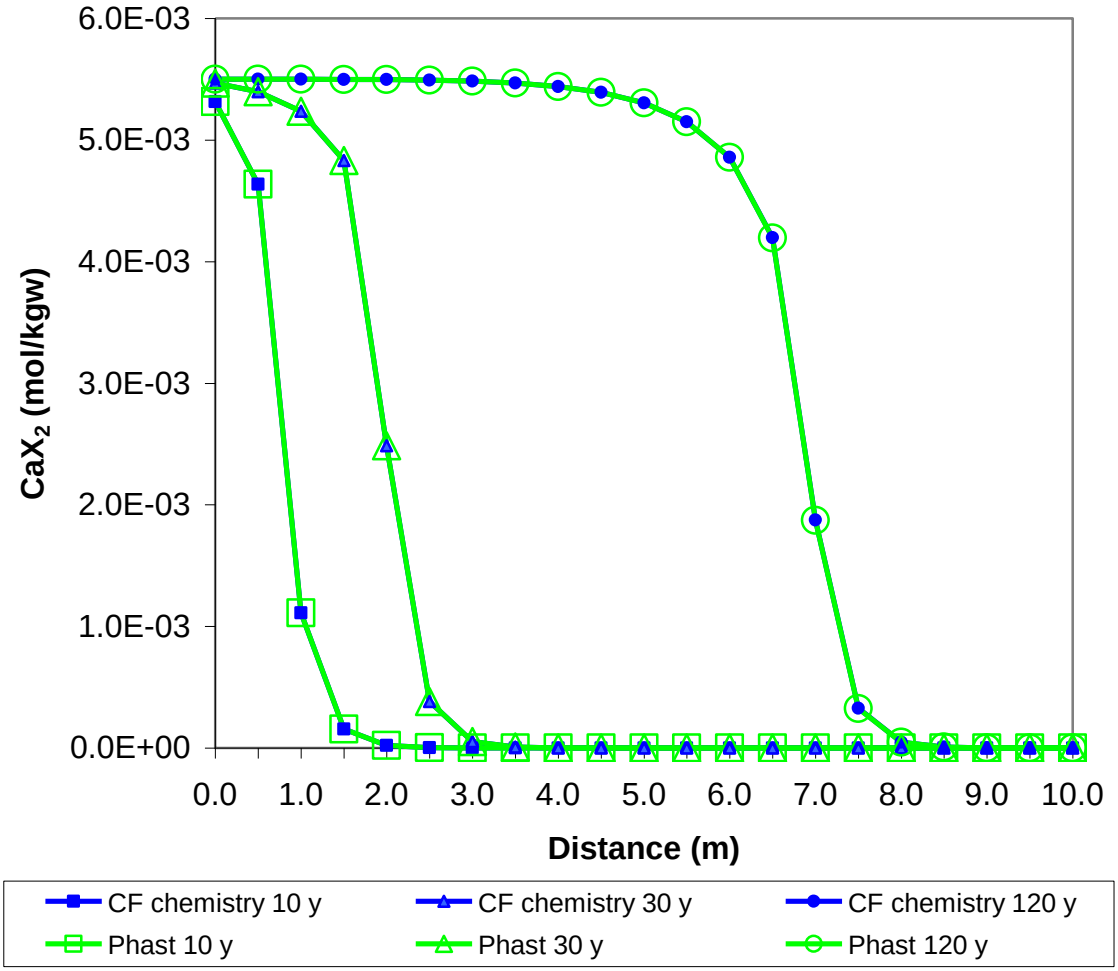

Figure 2-58 Comparison of the CaX2 distribution (in moles per kilogram of water) across the model for the ion exchange case between ConnectFlow (CF) and Phast. Quantities are sampled at 0.5 m intervals along the model column.

2.12.4.3 K-feldspar dissolution

Figure 2-59 shows the increase in the mass fraction of aluminium over time at three different times due to the dissolution of K-feldspar. The decrease in the amount of K-feldspar due to dissolution is shown in Figure 2-60. There is excellent agreement between the results for ConnectFlow and Phast.

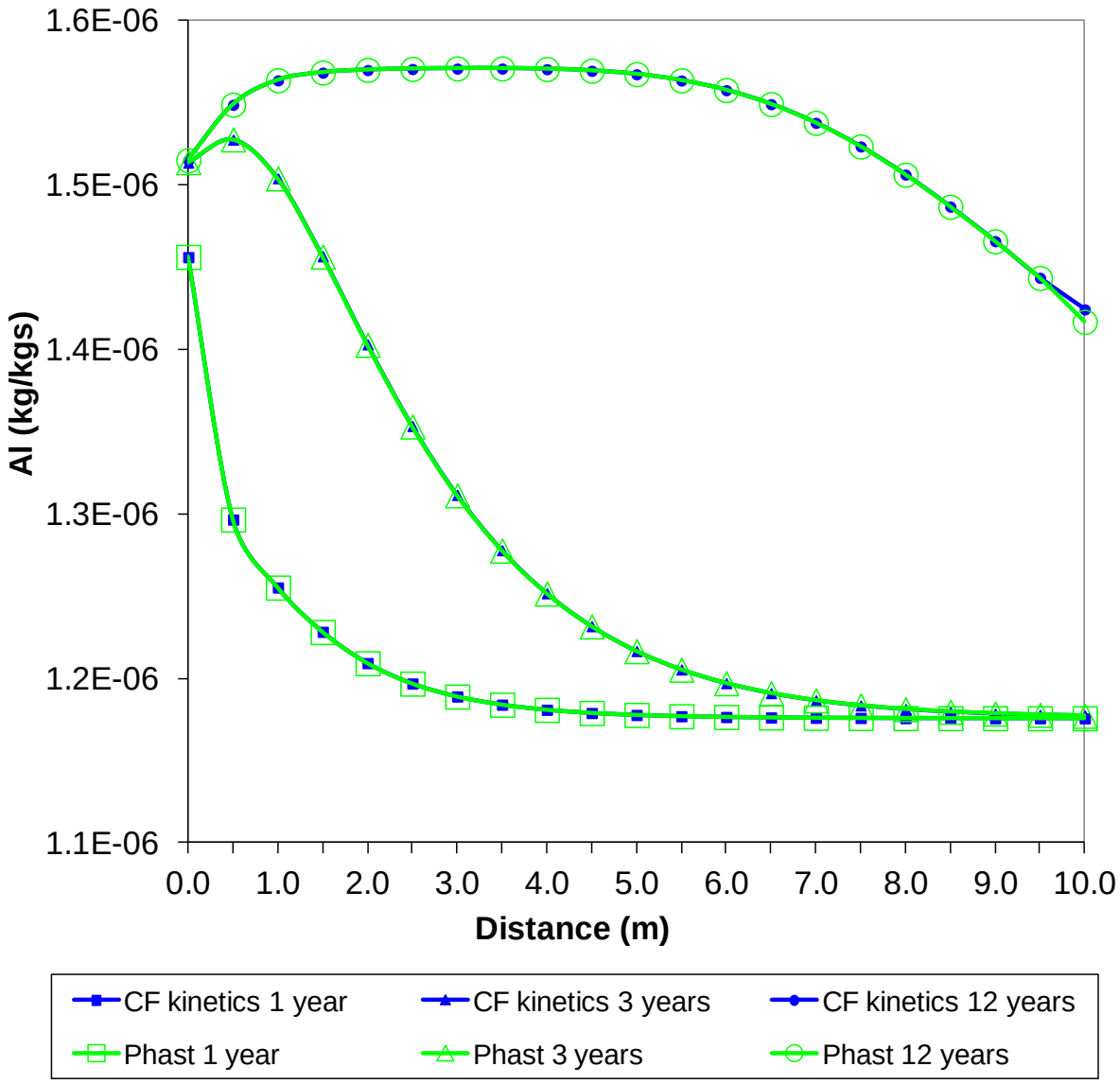

Figure 2-59 Comparison of mass fraction profiles of aluminium for the K-feldspar dissolution case between ConnectFlow (CF) and Phast. Mass fractions are sampled at 0.5 m intervals along the model column.

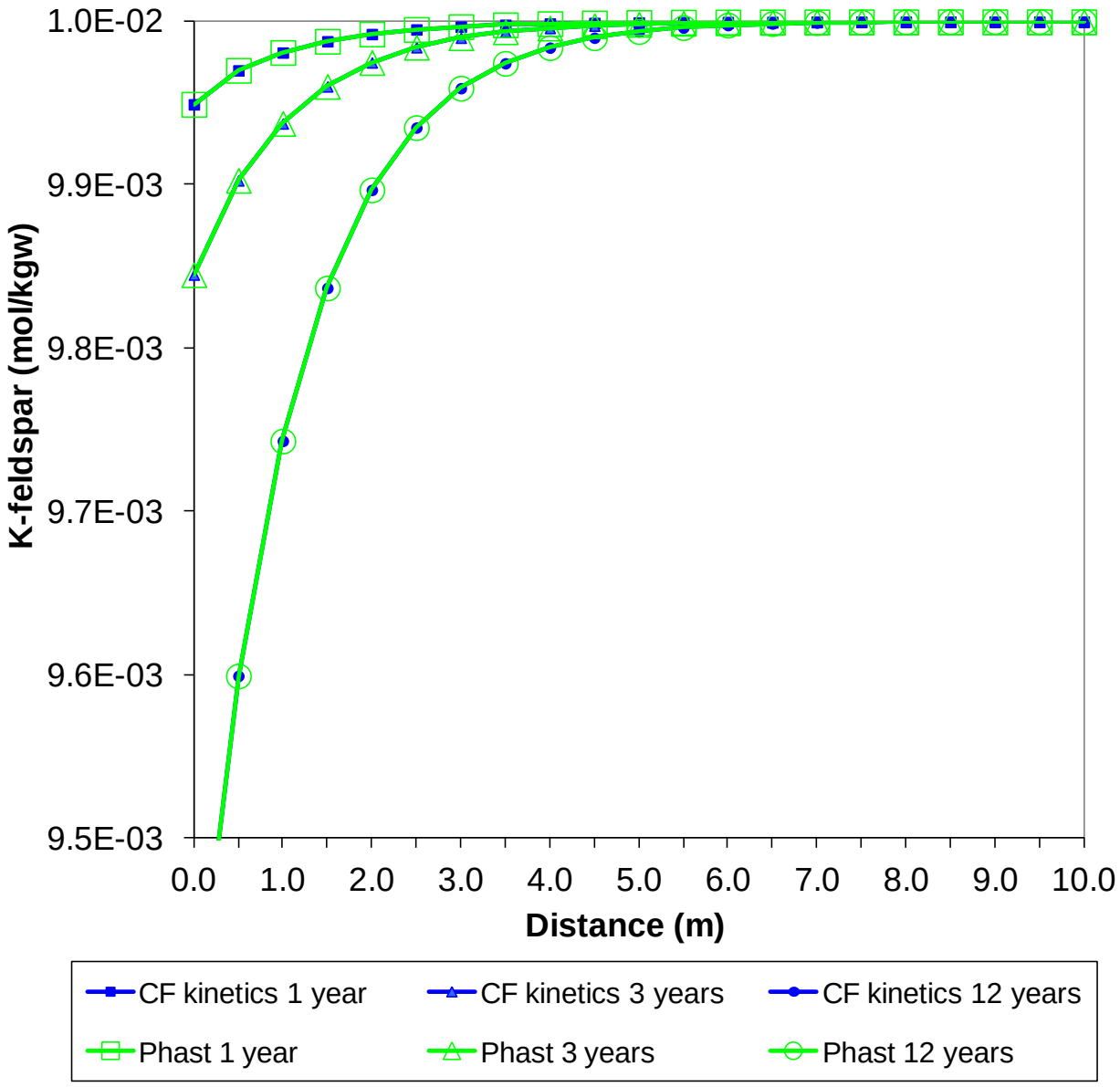

Figure 2-60 Comparison of K-feldspar quantities for the K-feldspar dissolution case between ConnectFlow (CF) and Phast. Mass fractions are sampled at 0.5 m intervals along the model column.

3. Discrete Fracture Network Verification

A summary of the DFN test cases is given in Table 3-1.

Table 3-1 DFN verification test

Case	Title	Overview
3.1	3D Fracture distributions	Generation and export of random fractures. The exported fractures are analysed to check the orientation and side length against the expected values.
3.2	3D Fracture connectivity.	Evaluation of the critical areal density in connecting 1 m square fractures, with a uniform distribution of orientations within a cube.
3.3	3D Fracture connectivity, power law distribution.	Evaluation of the critical areal density as a function of domain size for square fractures with a power law distribution exponent of 2.5 for fracture size and uniform distribution for orientation.
3.4	Upscaling from DFN to CPM.	Calculation of permeability distribution from a DFN model with and without guard zones. Import of permeability data into CPM model. Comparison of steady state flow distributions.
3.5	Radial steady state flow.	Steady state groundwater flow with a borehole used to apply the required mass flow boundary condition.
3.6	Three fracture intersections.	Steady state groundwater flow between three intersecting fractures. Forward and backward particle tracks are generated.
3.7	Steady state flow in fractured rock.	Steady state groundwater flow through intersecting fractures within a rock matrix. Rock matrix is modelled using an imported IFZ lattice and also via the in built matrix lattice option.
3.8	Henry's salt transport.	Steady state groundwater flow. Density dependent on salinity. Two variants are modelled, the first modelling the transport of salinity and the second using an imported density field.
3.9	Salt transport	One-dimensional transport of salt due to a pressure gradient
3.10	Salt upconing	Upconing of salt water into a tunnel in the centre of a thin 3D model. Comparison of CPM and DFN results.
3.11	Grouting of a single fracture.	Grouting of a fracture – external surface intersection.
3.12	Grouting of fractures intersecting a fracture in specified set.	Grouting of fracture-fracture intersections. One of the fractures is supposed to represent some physical features such as a tunnel.

Case	Title	Overview
3.13	Transient Salt Diffusion	One-dimensional diffusion of salinity in a fracture with no advective flow
3.14	1D Advection of Salinity	One-dimensional advection of salinity in a fracture
3.15	Transient Salt Upconing	Transient upconing of salt water into a tunnel in the centre of a fracture

3.1 3D Fracture Distributions

3.1.1 Overview

This case generates sets of random fractures using a number of commonly used distributions for length and orientation. The fractures are exported and analysed to verify that the observed distribution matches the expected values.

3.1.2 Problem Definition

Random fractures are generated in a 100 m x 100 m x 100 m cube. Six variations are considered with the following combination of properties.

Table 3-2 Input parameters for variations 1-3

Symbol	Parameter	Value
ψ	Dip angle	Uniform distribution 0-180 degrees
α	Dip direction	Uniform distribution 0-180 degrees
ω	Orientation	Uniform distribution 0-180 degrees
f_d	Fracture density	0.02
L1	Fracture side length 1	Truncated power law distribution
	Minimum	1 m
	Maximum	150 m
	Exponent	2.5, 3.0, 3.5 corresponding to variations 1-3
L2	Fracture side length 2	Truncated power law distribution
	Minimum	1 m
	Maximum	150 m
	Exponent	2.5, 3.0, 3.5 corresponding to variations 1-3

The range of exponents in Table 3-2 covers cases where large fractures dominate (exponent 2.5) and also where small fractures dominate (exponent 3.5). This is illustrated in Figure 3-1, Figure 3-2 and Figure 3-3.

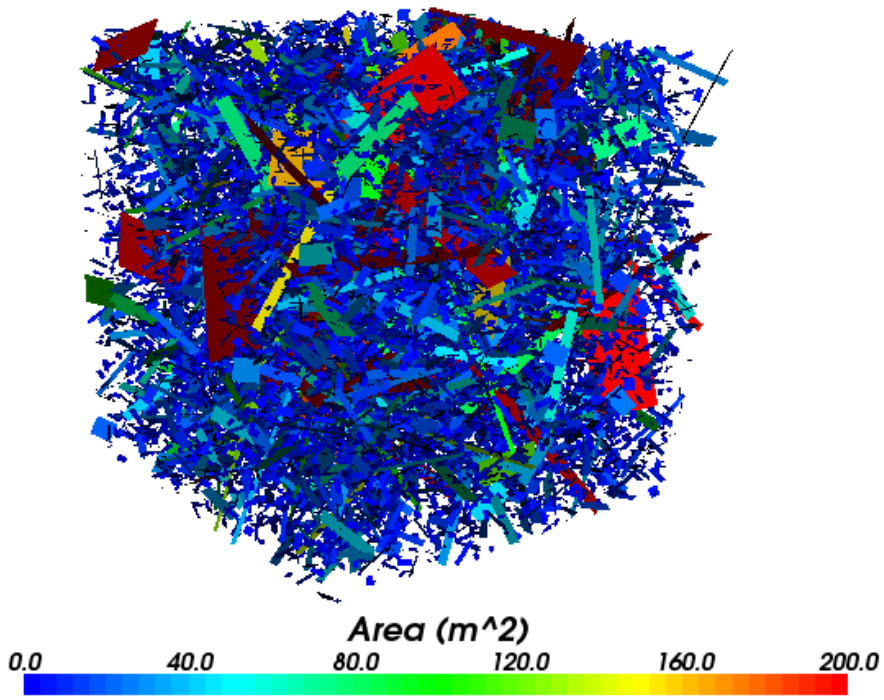

Figure 3-1 Fractures for exponent of 2.5, connectivity dominated by large fractures

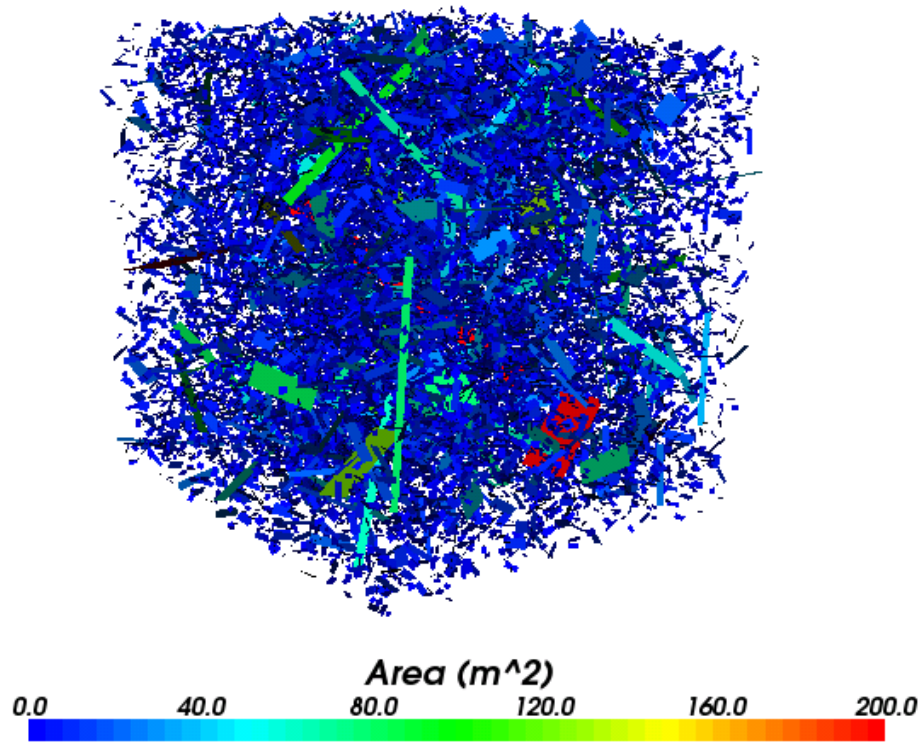

Figure 3-2 Fractures for exponent of 3.0

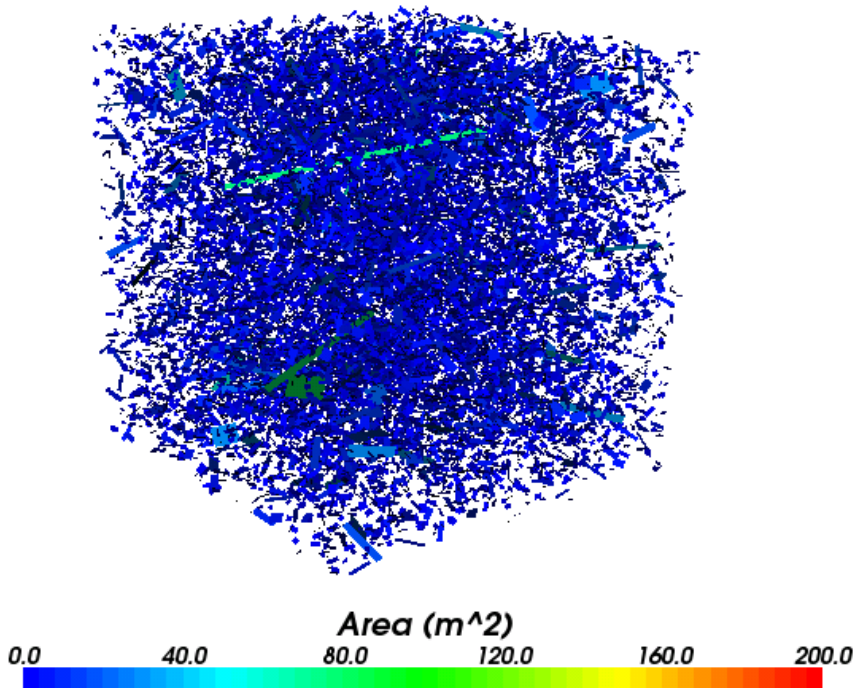

Figure 3-3 Fractures for exponent of 3.5, connectivity dominated by small fractures

Table 3-3 Input parameters for variations 4-6

Symbol	Parameter	Value
ψ	Dip angle	Fisher distribution with dispersion 5.0, 20.0, 100.0 corresponding to variations 4-6
α	Dip direction	Uniform distribution 0-180 degrees
ω	Orientation	Uniform distribution 0-180 degrees
f_d	Fracture density	0.02
L	Fracture side length of square fractures	Log normal distribution
	Mean of log(length)	2
	Standard deviation of log(length).	0.2, 0.4, 0.6 corresponding to variations 4-6

As the Fisher parameter increases in variations 4-6, the fractures become increasingly parallel. At the same time the standard deviation of the log of the length is increasing in the log normal distribution which gives rise to an increased number of larger fractures. This is illustrated in Figure 3-4, Figure 3-5 and Figure 3-6.

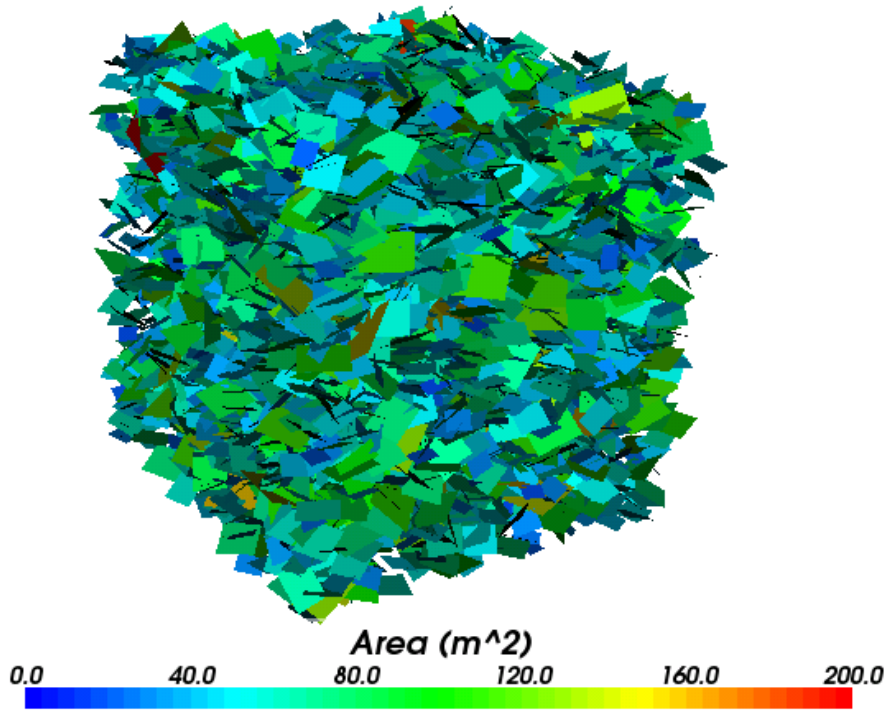

Figure 3-4 Fractures for Fisher dispersion 5.0

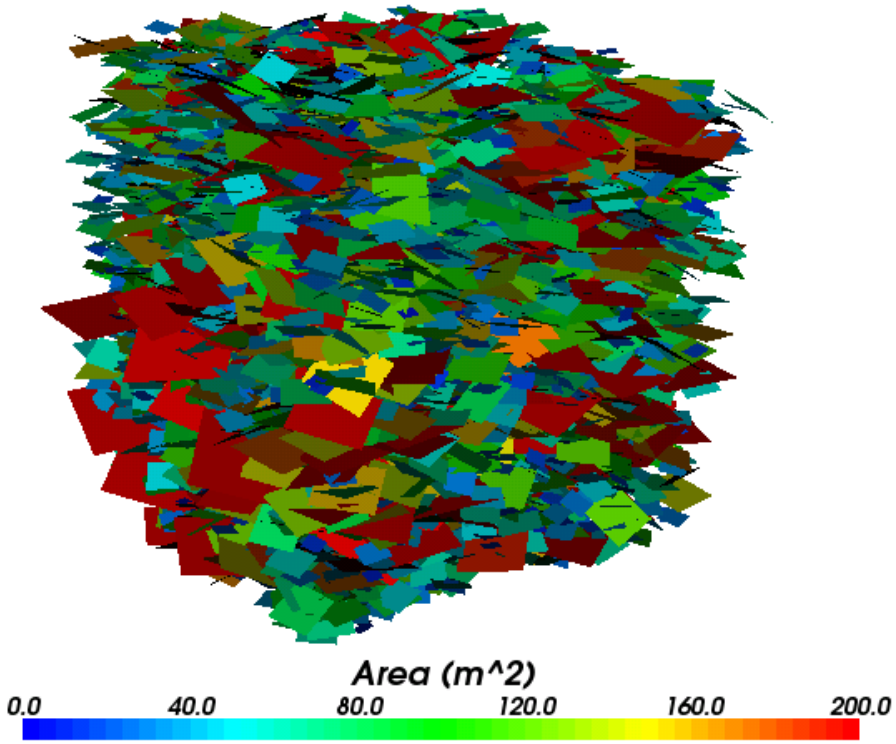

Figure 3-5 Reduced range of angles for fisher dispersion 20.0

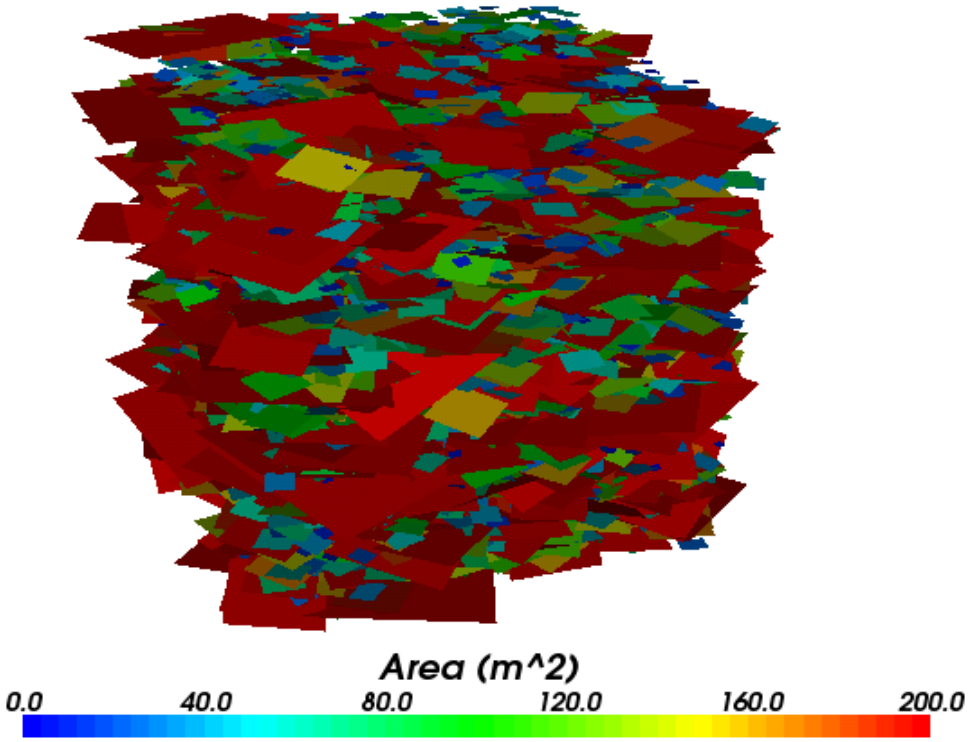

Figure 3-6 Reduced range of angles for fisher dispersion 100.0 and larger fractures due to increased standard deviation in log normal distribution.

3.1.3 Results

All results agree to within 5% of the expected values.

3.1.3.1 Variations 1-3

The volume of the region is 1.0E6 m^3, given a point density of 0.02 the expected number of generated fractures is 20000. The results for variations 1-3 are shown in Table 3-4.

Table 3-4 Number of randomly generated fractures

Variation	Expected Value	Measured Value	Error
Variation 1	20000	19743	1.29%
Variation 2	20000	20116	0.58%
Variation 3	20000	20015	0.08%

In each of these variations the fracture normal is uniformly distributed over all possible directions. This is tested by calculating the average unit normal vectors over all fractures. The magnitude of the resulting vector should approach zero as the number of fractures increases (a value of 1 would correspond to all fractures being parallel). The results for variations 1-3 are shown in Table 3-5.

Table 3-5 Magnitude of Average Fracture Normal

Variation	Expected Value	Measured Value	Error
Variation 1	0.0	0.0031	0.31%
Variation 2	0.0	0.0095	0.95%
Variation 3	0.0	0.0065	0.65%

For a set of n fractures of side length l_i and minimum side length $l_{\min}$ an estimate for the power law distribution exponent η is given in [xx] as

$$\eta = 1 + n\left[\sum_{i=1}^{n} \ln\left(\frac{l_i}{l_{\min}}\right)\right]^{-1}$$

Applying this to variations 1-3, gives the results shown in Table 3-6 and Table 3-7.

Table 3-6 Estimated power law exponent for fracture side length 1

Variation	Expected Value	Measured Value	Error
Variation 1	2.5	2.513	0.52%
Variation 2	3.0	3.035	1.16%
Variation 3	3.5	3.510	0.29%

Table 3-7 Estimated power law exponent for fracture side length 2

Variation	Expected Value	Measured Value	Error
Variation 1	2.5	2.513	0.52%
Variation 2	3.0	3.017	0.57%
Variation 3	3.5	3.514	0.40%

3.1.3.2 Variations 4-6

The volume of the region is 1.0E6 m^3. Given a point density of 0.02, the expected number of generated fractures is 20000. The results for variations 4-6 are shown in Table 3-8.

Table 3-8 Number of randomly generated fractures

Variation	Expected Value	Measured Value	Error
Variation 4	20000	19740	1.30%
Variation 5	20000	19896	0.52%
Variation 6	20000	19771	1.15%

For a set of n fractures with angle θ to the average normal, an estimate for the fisher dispersion parameter κ is given in [xxi] as

$$\kappa = \frac{R(3-R^2)}{1-R^2} \text{ where } R = \frac{1}{n}\sum_{i=1}^{n} \cos(\theta)$$

Applying this to variations 4-6, gives the results shown in Table 3-9

Table 3-9 Fisher distribution parameter

Variation	Expected Value	Measured Value	Error
Variation 4	5.0	5.14	2.90%
Variation 5	20.0	20.11	0.55%
Variation 6	100.0	100.06	0.06%

For a log normal distribution, the arithmetic mean and standard deviation are given in [xxii] as

$$\mu = e^{\mu_l + \frac{\sigma_l^2}{2}} \text{ and } \sigma = e^{\mu_l + \frac{\sigma_l^2}{2}} \sqrt{e^{\sigma_l^2} - 1}$$

Where μ_l and σ_l are the mean and standard deviation of the log of the distribution. Applying this to the fracture length distribution in variations 4-6 gives the results shown in Table 3-10 and Table 3-11.

Table 3-10 Average side length for log normal distribution

Variation	Expected Value	Measured Value	Error
Variation 4	7.53	7.48	0.68%
Variation 5	8.00	7.96	0.62%
Variation 6	8.85	8.73	1.29%

Table 3-11 Standard deviation of side length for log normal distribution

Variation	Expected Value	Measured Value	Error
Variation 4	1.52	1.54	1.17%
Variation 5	3.33	3.29	1.20%
Variation 6	5.82	5.59	3.92%

3.2 3D Fracture Connectivity

3.2.1 Overview

The DFN software has the ability to create networks of random fractures with specified properties. This case uses percolation theory to check the generation and connectivity of random fractures within a cube.

3.2.2 Problem Definition

The modelled domain is a cube of side length 20 m. This is filled with randomly generated square fractures with side length 1 m and with random orientation and position. This is illustrated in Figure 3-7.

Table 3-12 Input parameters

Symbol	Parameter	Value
ψ	Dip angle	**Uniform distribution 0-90 degrees**
α	Dip direction	**Uniform distribution 0-90 degrees**
ω	Orientation	**Uniform distribution 0-90 degrees**
l	Fracture side length	**1 m**
L	Cube side length	**20 m**

The critical areal density at which all surfaces of the cube should be connected by the fracture network is given in [xxiii] as 1.23.

3.2.3 Results

Thirty different random numbers seeds were used. For each seed a progression of areal densities were used in order to estimate the critical density. The average resulting critical density was 1.32, 7.3% higher than in [xxiii].

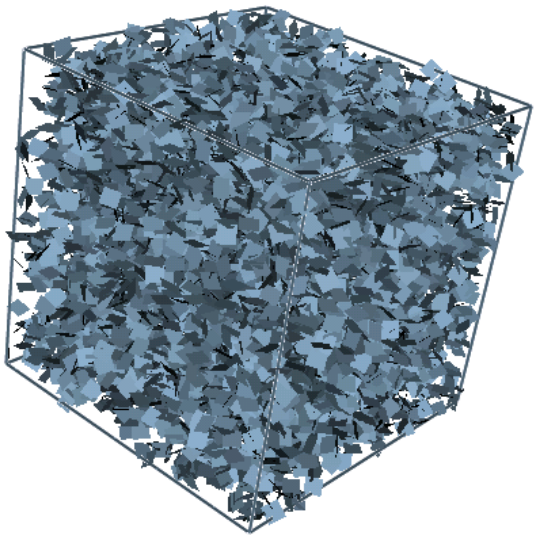

Figure 3-7 Fractures at critical areal density

3.3 3D Fracture Connectivity with a Power Law Size Distribution

3.3.1 Overview

This case considers the connectivity of random fractures within a cube, where the fracture lengths follow a power law distribution. The solution is taken from [xxiv].

3.3.2 Problem Definition

The modelled domain is a cube for a range of increasing sizes. This is filled with randomly generated square fractures with side length corresponding to a truncated power law.

Table 3-13 Input parameters

Symbol	Parameter	Value
ψ	Dip angle	**Uniform distribution 0-90 degrees**
α	Dip direction	**Uniform distribution 0-90 degrees**
ω	Orientation	**Uniform distribution 0-90 degrees**
a	Exponent in power law	**2.5**
L	Cube side length	**5 - 300 m**

When the exponent is less than 3 the critical fracture density varies with domain size and the connectivity is dominated by the larger fractures. This is illustrated in Figure 3-9.

For large values of the exponent the connectivity of the smaller fractures dominates and the critical density does not vary with domain size for sufficiently large domains. This is similar to case 0.

3.3.3 Results

A comparison of the dependence of the critical density on domain size is shown in Figure 3-8. The reference data is taken from [xxiii].

The results from ConnectFlow show good agreement, particularly in terms of the slope which, as discussed in [xxiii], varies significantly with the exponent a.

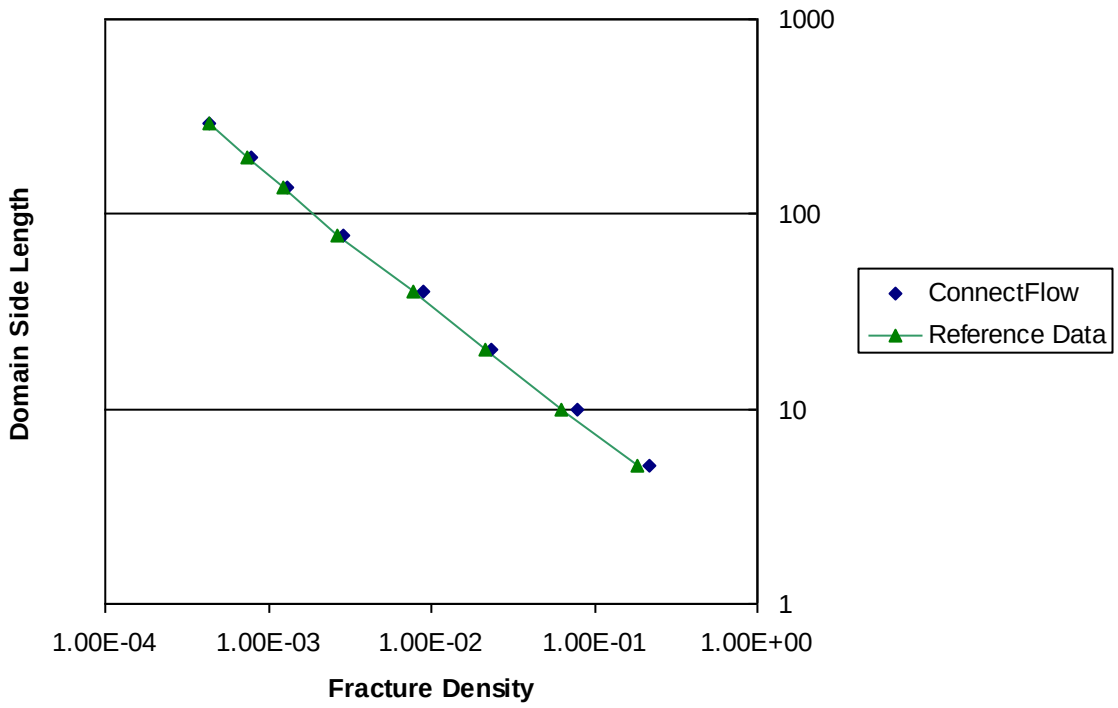

Figure 3-8 Critical fracture density variation with domain size

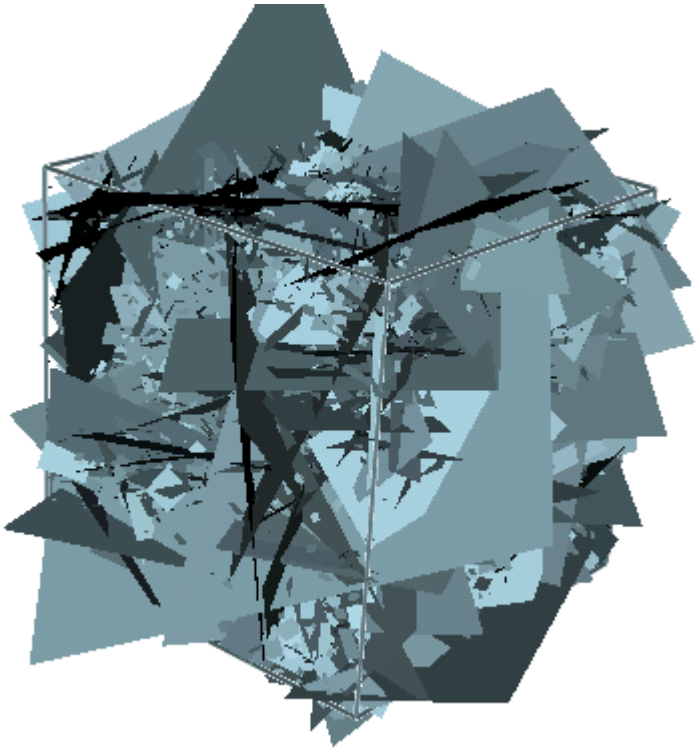

Figure 3-9 Fracture network generated using a power law size distribution (*a*=2.5)

3.4 Upscaling from DFN to CPM

3.4.1 Overview

This case is taken from the DECOVALEX Task C [xxv] and calculates the permeability through a 20 m x 20 m region of fractured rock, generated from fracture mapping data from Sellafield UK.

The fracture set consists of 7797 fractures, with lengths varying from 0.5 to >30 m, and apertures varying from 1 to 200 microns.

The upscaled permeabilties are then used in a CPM calculation and the mass flows are compared.

3.4.2 Problem Definition

The modelled domain consists of a 20 m x 20 m x 1 m region with an applied horizontal pressure gradient of 1.0E4 Pa/m, as illustrated in Figure 3-10.

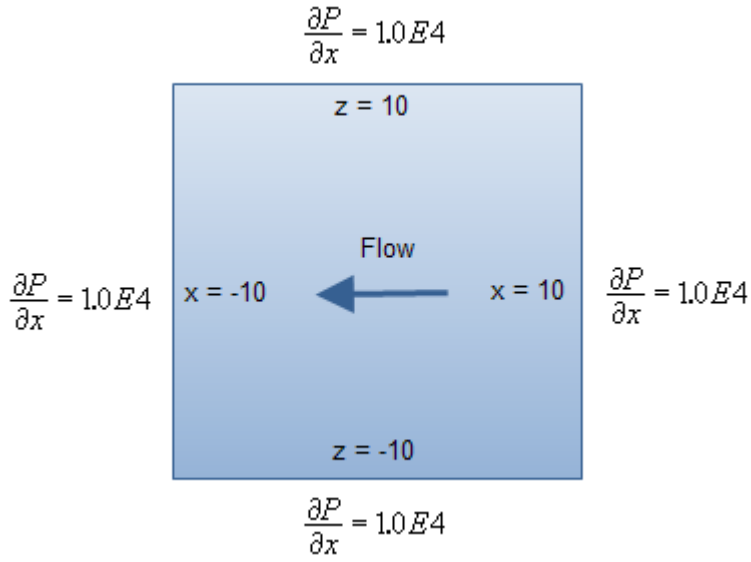

Figure 3-10 Schematic of problem definition

The fracture distribution is shown in Figure 3-11 and the input parameters in Table 3-14.

Table 3-14 Input parameters

Symbol	Parameter	Value
ρ	Density	**1000 kg/m^3**
μ	Viscosity	**1.0E-3 Ns/m^2**

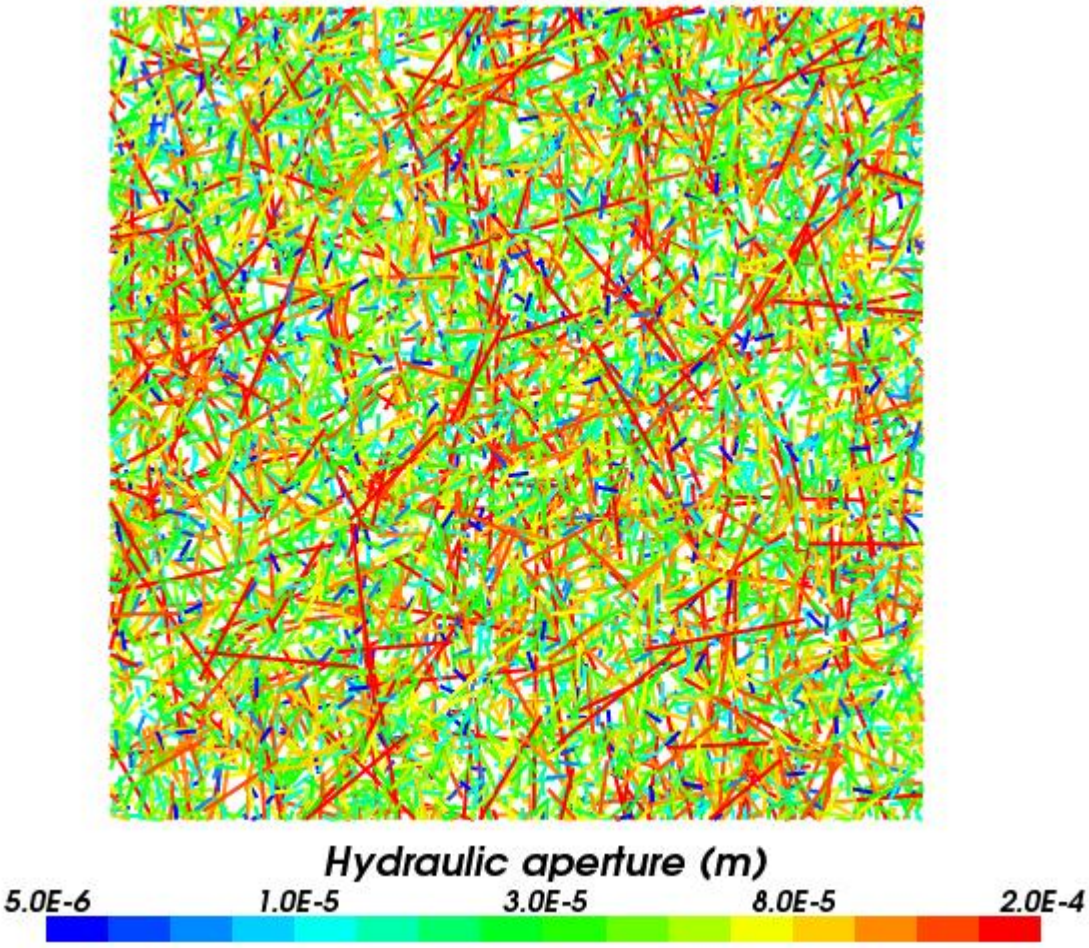

Figure 3-11 Fractured Rock

The DFN permeabilities are calculated on a regular grid of cells and the CPM calculation uses a regular grid of the same resolution. The finest grid resolution tested was 400x400 cells.

3.4.3 Variations

3.4.3.1 Cellular Model Calculation

The DFN region is overlayed with a grid of cells of the required resolution.

3.4.3.2 Cellular Model with Guard Zone

Each cell is stretched by a factor 3 in the x and z directions and then the middle section is used to export permeabilities for the area of interest. This helps improve accuracy where single fractures intersect more than one of the cells sides.

3.4.3.3 Regional Model Calculation

The DFN model region is used to define the grid of cells.

3.4.4 Results

The overall flow through the left hand boundary x=-10 is compared against the stress free TUL results from [xxv] and the upscaled CPM results (with guard zone). The CPM result is 3% larger than the TUL result.

Table 3-15: Flow through left-hand boundary at X = -10

Approach	Flow X=-10
TUL	**9.40E-5 m^3/s**
ConnectFlow DFN	**9.67E-5 m^3/s**
ConnectFlow CPM (400 x 400 upscaling)	**9.71E-5 m^3/s**

DFN and CPM Results without guard zones agreed to within 6%, whether calculated through region elements or through cellular model calculation.

The distribution of outflow at x = -10 m is compared between DFN and CPM models in Figure 3-12 for a range of upscaling resolutions. The data is averaged over 1 m intervals in order to better compare the bulk profile. Flow orthogonal to the pressure gradient at the outflow boundary z = 10 m is shown in Figure 3-13.

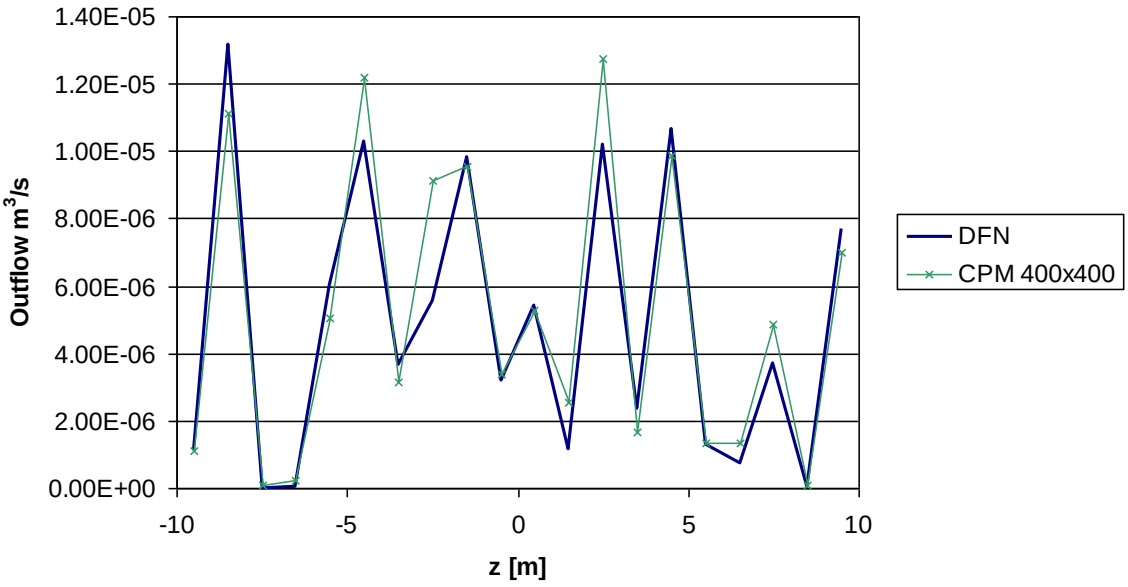

Figure 3-12 Outflow distribution at left boundary (X=-10 m) for cellular model upscaling with no guard zone

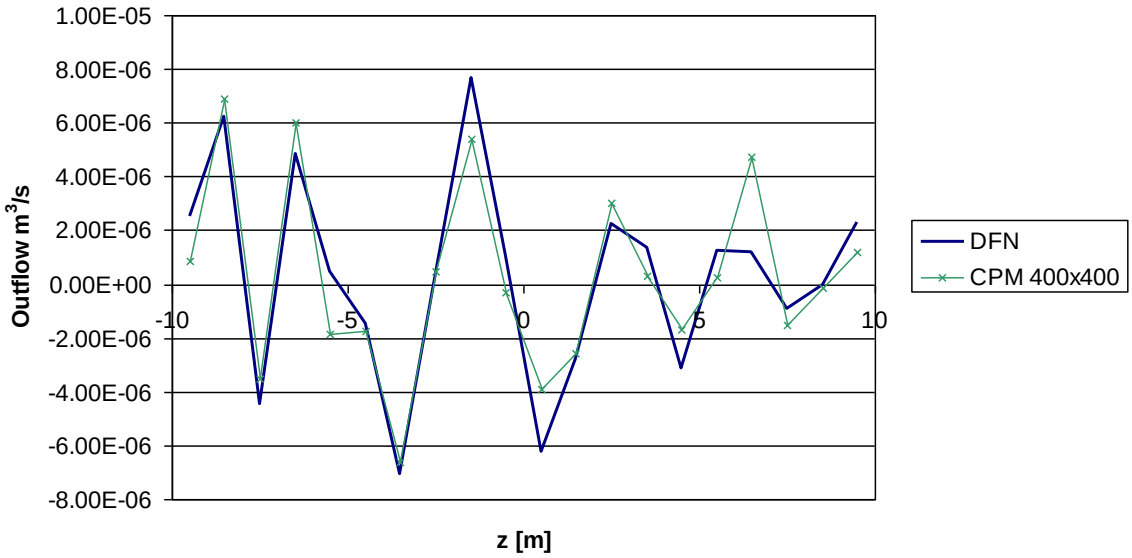

Figure 3-13 Outflow distribution at top boundary (Z=10 m) for cellular model upscaling with no guard zone

The overall outflow through the 20 m top surface is 5.45E-6 m3/s as computed by the DFN model and 6.01E-6 m3/s as computed by the CPM 400x400 model. This is around 1/20th of the outflow in the direction aligned with the pressure gradient.

Figure 3-14 compares the outflow distribution across the three variations in 3.4.3 for an upscaling resolution of 400x400. The Cellular and Model Region variations are virtually identical as expected. Use of the guard zone improves the agreement as compared with the DFN solution.

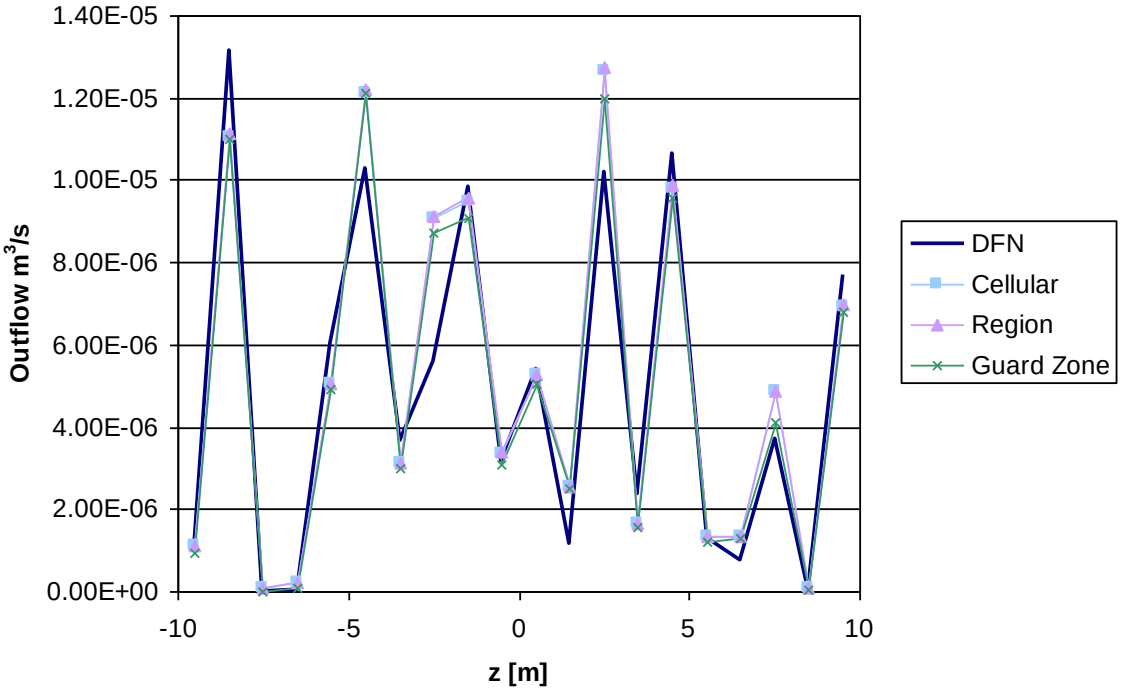

Figure 3-14 Comparison of outflows at left boundary (X=-10m) using a CPM resolution of 400x400

3.5 Radial Steady State Flow

3.5.1 Overview

This case models steady groundwater flow in a 2D disk where water is removed from the centre at a constant rate and the outer disk boundary is maintained at a constant head.

The example has a simple analytical solution and can be used to test a range of modelling choices.

3.5.2 Problem Definition

This case is the DFN equivalent of Case 0.

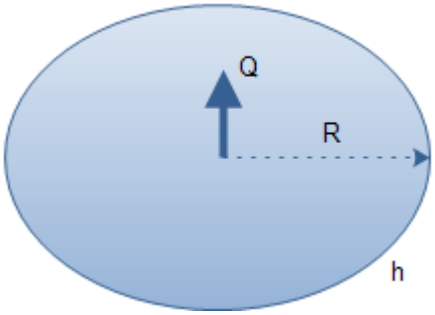

Figure 3-15 Schematic of problem definition

For a fracture, the aperture, *e*, is related to the hydraulic conductivity, *K* by

$$e = \sqrt{\frac{12K\mu}{\rho g}}$$

The values in Table 3-16 have scaled Q from 1.0E-7 in Case 0 to give an equivalent head distribution.

A 5 degree sector of the disk is modelled and is tessellated using 100 single fractures along its length. As these fractures are not rectangular, ConnectFlow breaks them up into right angle triangles as illustrated in Figure 3-16.

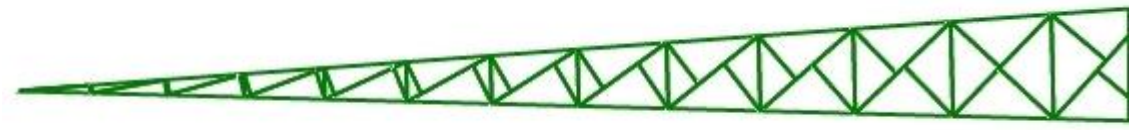

Figure 3-16 Fractures in sector of disk

The fractures used model the circumference of the sector as a straight line. As a result the accuracy of the simulation increases as the angle of the sector decreases.

The outflow at the axis is modelled using a borehole with a specified flow rate which has direction orthogonal to the disk.

Table 3-16 Input parameters

Symbol	Parameter	Value
h	Head at disk circumference	**0 m**
Q	Outflow from disk	**1.11E-14 m^3/s**
K	Hydraulic Conductivity	**1.0E-8 m/s**
R	Radius of disk	**2000 m**
e	Aperture of fracture	**1.11E-7 m**
r	Radial distance from axis	**0-2000 m**
ρ	Density	**1000 kg/m^3**
μ	Viscosity	**1.0E-3 Pa.s**
g	Gravity	**9.8 m/s^2**

3.5.3 Results

The analytical solution is given by

$$h(r) = h(R) - \frac{Q}{2\pi Kd}\ln(\frac{R}{r})$$

The results from ConnectFlow show good agreement with the analytical solution, as illustrated in Figure 3-17.

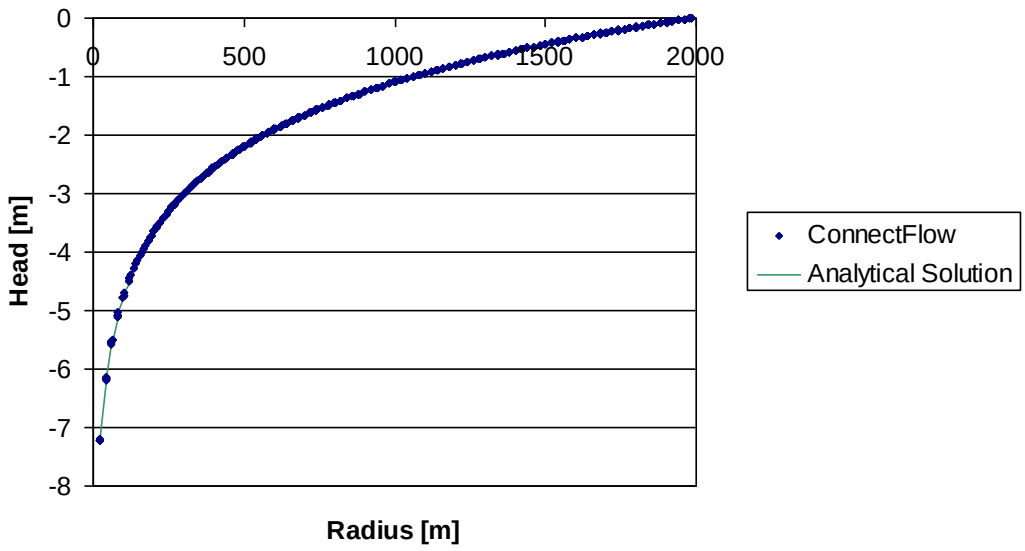

Figure 3-17 Variation of head with distance from the axis with an outflow modelled with a borehole

3.6 Three Fracture Intersections

3.6.1 Overview

This case models steady groundwater flow and particle tracking in a simple two dimensional fracture network.

3.6.2 Problem Definition

The problem is a variant of test C1 from DarcyTools [xxvi]. Three fractures are placed in a rectangular region as shown in Figure 3-18.

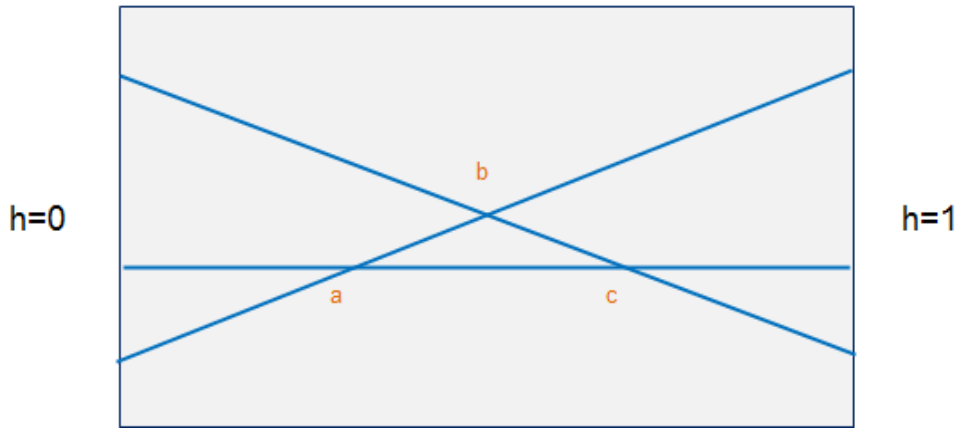

Figure 3-18 Three fracture intersections

A 3x3 system of linear equations is derived by applying mass conservation at the three fracture intersections. This is used to calculate the heads at a, b and c and hence the flow rates in each fracture segment.

The fracture geometry used for this test is defined in Table 3-17.

Table 3-17 Fracture locations

X Start	Y Start	X End	Y End
0	2	12	**5**
0	3	12	**3**
0	5	12	**2**

3.6.3 Variations

3.6.3.1 Symmetric

For the symmetric case, the fracture aperture is set to 1.0E-4 m for all three fractures. This gives an analytical flow field where the flow rates along each fracture are almost identical.

3.6.3.2 Non-symmetric

In the non-symmetric case, the fracture apertures are set to 1.0E-4 m for the fracture passing through section bc, 2.0E-4 m for section ac and 4.0E-4 m for section ab. In addition, the section of fracture passing through ab is removed as shown in Figure 3-19.

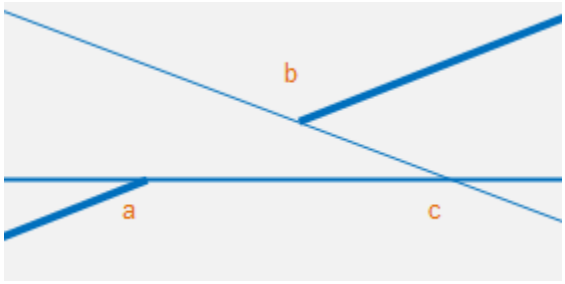

Figure 3-19 Non symmetric fractures

This arrangement means that the flow at b splits, with some of it moving to c and then a, and the rest moving directly towards the left hand boundary.

The particle tracking is tested by releasing 10000 particles at the h=1 surface, with the fraction of particles in each fracture distributed in proportion to the analytical inflow rate.

The proportion of particles leaving the geometry at Y=2, 3 and 5 should correspond to the ratio of the analytically predicted outflow rates.

Table 3-18 Analytical inflow/outflow

Y	Analytical inflow distribution at X=12	Analytical outflow distribution at X=0
2	7.9%	**77.3%**
3	64.9%	**10.0%**
5	27.2%	**12.7%**

For this test, the `APPROXIMATE PARTICLE TRACKING` model is used, with forward tracking to track from inflow to outflow and backward tracking to track from outflow to inflow.

3.6.3.3 Symmetric – Exact Particle tracking

This test is identical to the symmetric case, but using the `EXACT PARTICLE TRACKING` method instead of approximate particle tracking.

The proportion of particles leaving the geometry at Y=2, 3 and 5 should correspond to the ratio of the analytically predicted outflow rates, i.e. it should be the same in all three locations.

3.6.4 Results

3.6.4.1 Symmetric

The predicted results for head are within 1% of the analytical values.

Table 3-19 Heads at fracture intersections

Intersection	ConnectFlow	Analytical	% Error
a	0.333	0.333	**0.19%**
b	0.496	0.500	**0.89%**
c	0.667	0.667	**0.10%**

3.6.4.2 Non Symmetric

The ConnectFlow head distribution for this case is shown in Figure 3-20. Predicted results for the head and particle flows are within 5% of the analytical values.

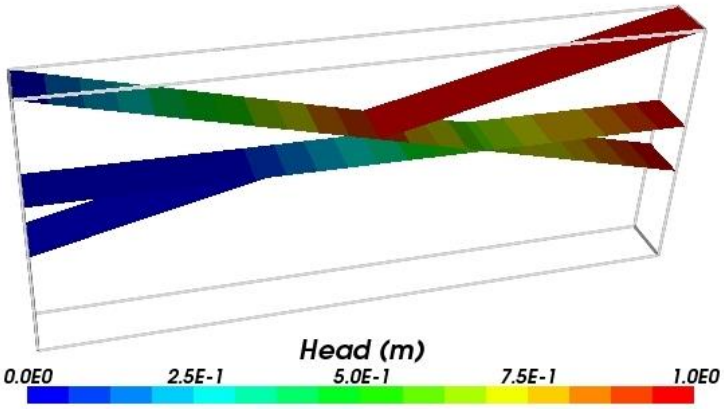

Figure 3-20 Head distribution

Table 3-20 Heads at fracture intersections

Intersection	ConnectFlow	Analytical	% Error
a	0.062	0.061	**1.49%**
b	0.937	0.968	**3.23%**
c	0.599	0.600	**0.15%**

Table 3-21 Particle flow rates (backwards)

Y at Exit	ConnectFlow	Analytical	Error
2	7.4%	7.9%	**0.5%**
3	65.6%	65.0%	**0.6%**
5	27.0%	27.2%	**0.2%**

Table 3-22 Particle flow rates (forwards)

Y at Exit	ConnectFlow	Analytical	Error
2	77.6%	77.3%	**0.3%**
3	9.5%	10.0%	**0.5%**
5	12.9%	12.7%	**0.2%**

3.6.4.3 Symmetric – Exact Particle tracking

The predicted proportions of particles leaving the model at each location are within 1% of the analytical values.

Table 3-23 Proportions of particles at each outflow point using exact particle tracking

Y at Exit	ConnectFlow	Analytical	% Error
2	33.1%	33.3%	**0.2%**
3	33.8%	33.3%	**0.5%**
5	33.1%	33.3%	**0.2%**

3.7 Steady Flow in Fractured Rock

3.7.1 Overview

The example is taken from Level 1 of the international HYDROCOIN project for verification of groundwater flow codes [xxvii] and is the same problem as CPM Case 0.

It models steady state flow in a two-dimensional vertical slice of fractured rock. The rock contains two inclined fractures which intersect one another at depth, and have a higher permeability than the surrounding rock.

The topography has been made simple so that it consists of two valleys located where the fracture zones meet the surface. To simplify the problem definition, the shape of the surface is described by straight lines. Although the surface topography is symmetric, the flow is influenced by the asymmetry of the fracture zones.

This problem is based on an idealized version of the hydrogeological conditions encountered

at a potential site for a deep repository in Swedish bedrock. A detailed three-dimensional

model of this was made in a separate study [xxviii].

3.7.2 Problem Definition

Figure 3-21 depicts the modelled domain.

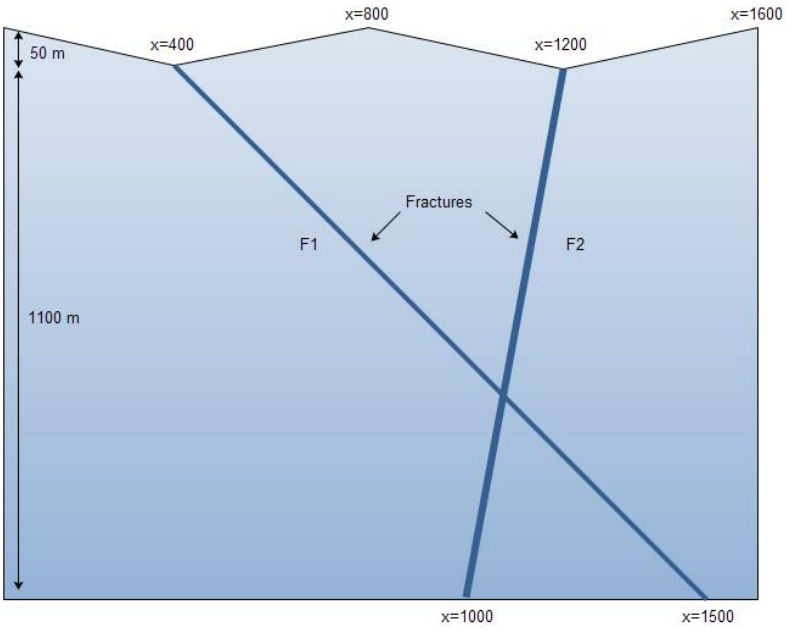

Figure 3-21 Fractured rock

Table 3-24 Input parameters

Symbol	Parameter	Value
K_r	Hydraulic conductivity of rock	**1.0E-8 m/s**
K_{rf}	Hydraulic conductivity of CPM fractured region	**1.0E-6 m/s**
e_1	Thickness of fracture F1	**2.053E-4 m**
e_2	Thickness of fracture F2	**2.620E-4 m**

The fracture apertures have been derived to match the transmissivities of the fracture regions in case 2.2.2. For the DFN model, the transmissivity is proportional to aperture cubed and for the CPM model it is proportional to the cross sectional thickness of the region representing the fracture.

The rock is modelled using an array of fractures as shown in Figure 3-22. The figure is drawn in perspective to make it easier to visualise.

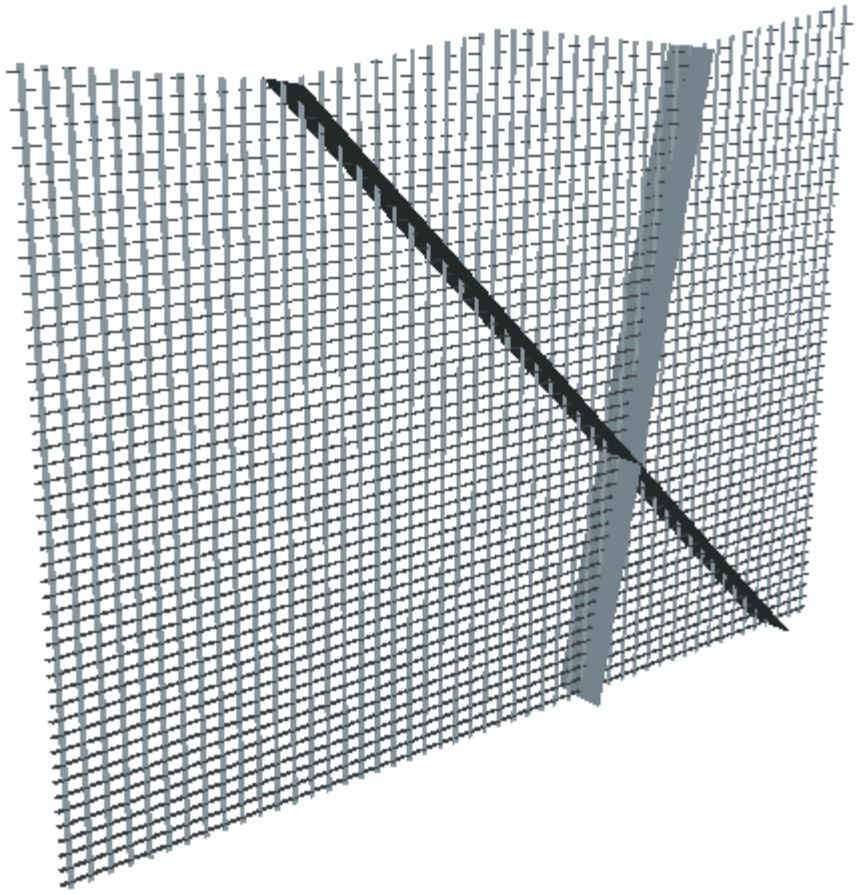

Figure 3-22 Modelled fractures

3.7.3 Variations

3.7.3.1 IFZ Rock Matrix

In this variant, the rock matrix is modelled using a two dimensional grid of fractures that are read in as an Implict Fracture Zone (IFZ) file.

3.7.3.2 Matrix Lattice Option

In this variant, the rock matrix is modelled using a three dimensional grid of fractures generated by the command `GENERATE MATRIX LATTICE`. In this case, the fracture widths are set automatically and are approximately twice as wide as that set manually in the IFZ Rock Matrix variant.

3.7.3.3 Current Value

In this variant, a subset of the domain is modelled, x = 100 to 1500 m and y = -300 to -100 m. This is illustrated in Figure 3-23.The boundary pressure is taken from the CPM solution 2.2.3.1 and applied using the `>>CURRENT VALUE` boundary condition option. The rock matrix is modelled using the same IFZ approach as in 3.7.3.1.

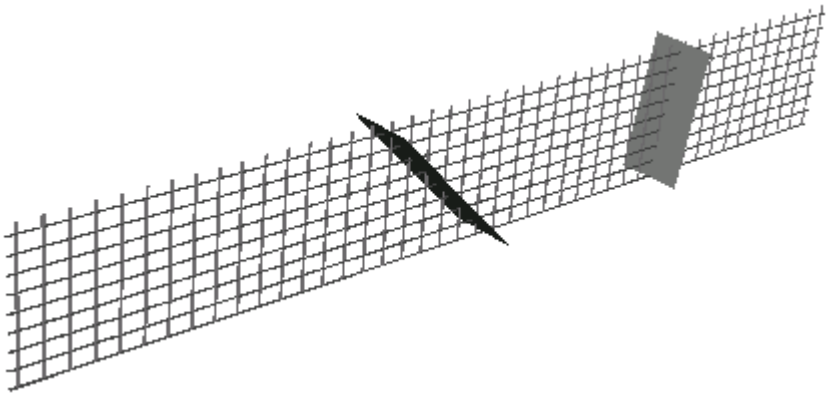

Figure 3-23 Current Value

3.7.4 Results

The results presented here compare the head profile at a height of y=-200 m and show excellent agreement with the HYDROCOIN study.

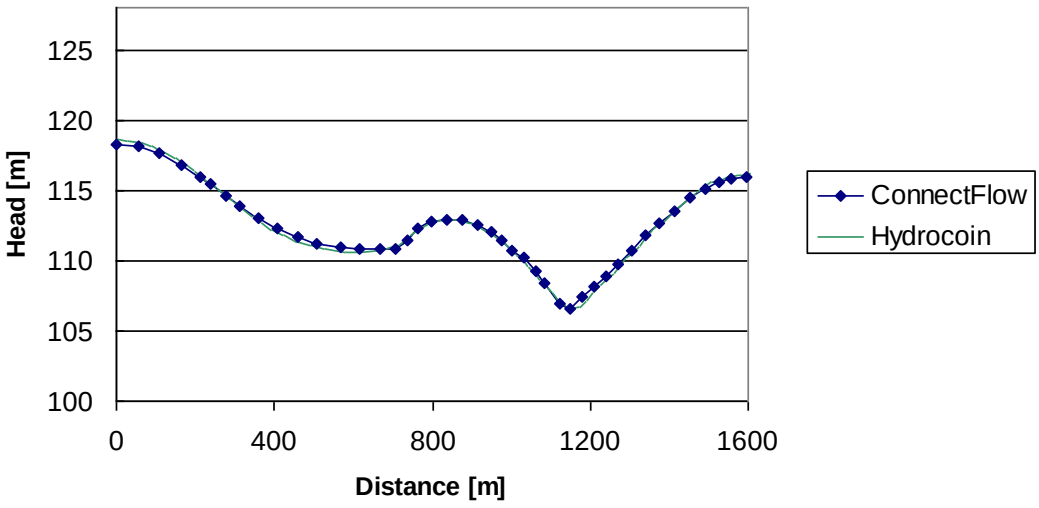

Figure 3-24 Head at height -200 m (IFZ Rock Matrix)

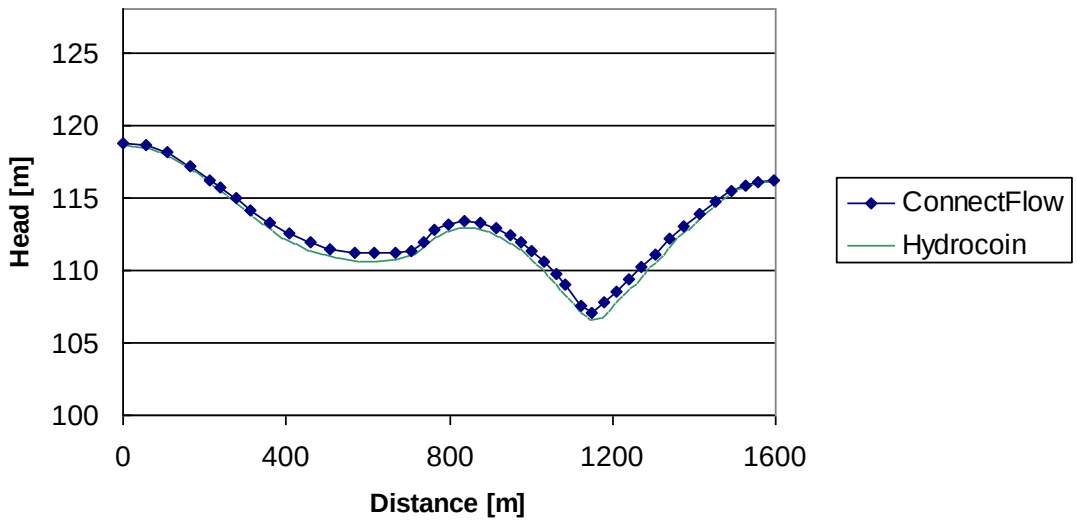

Figure 3-25 Head at height -200 m (Matrix Lattice)

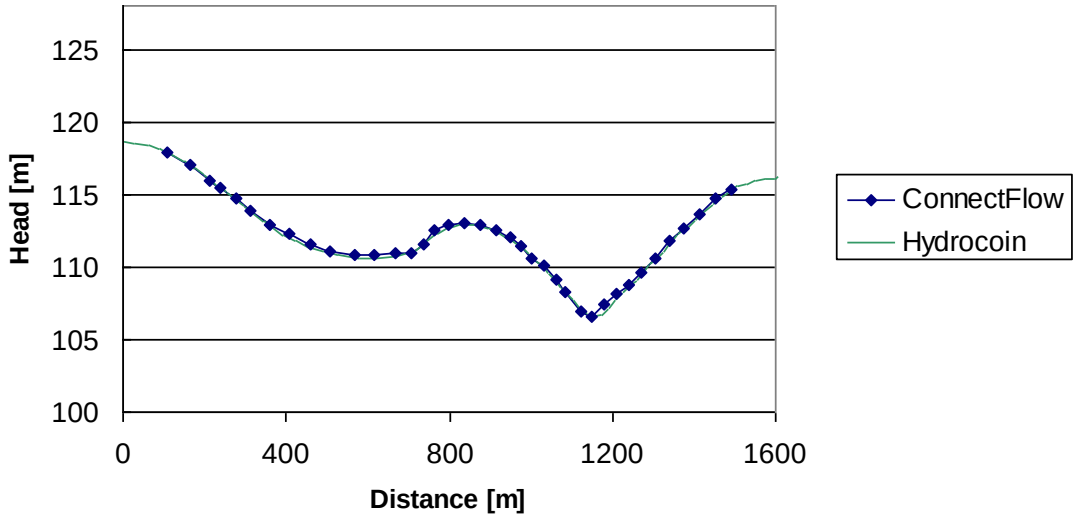

Figure 3-26 Head at height -200 m (Current Value)

In addition, the ConnectFlow results were compared against the Feftra base case results [iii], with the differences in head between the two codes being less than 0.5% for the IFZ Rock Matrix and Reduced Domain variants and less than 1% for the Matrix Lattice.

The latter is marginally less accurate due to the increased permeability contribution of the wider rock matrix fractures. This was checked by making the fractures in the IFZ Rock Matrix variant deliberately wider and the same trend was seen.

Figure 3-27 shows the head distribution through the fracture network.

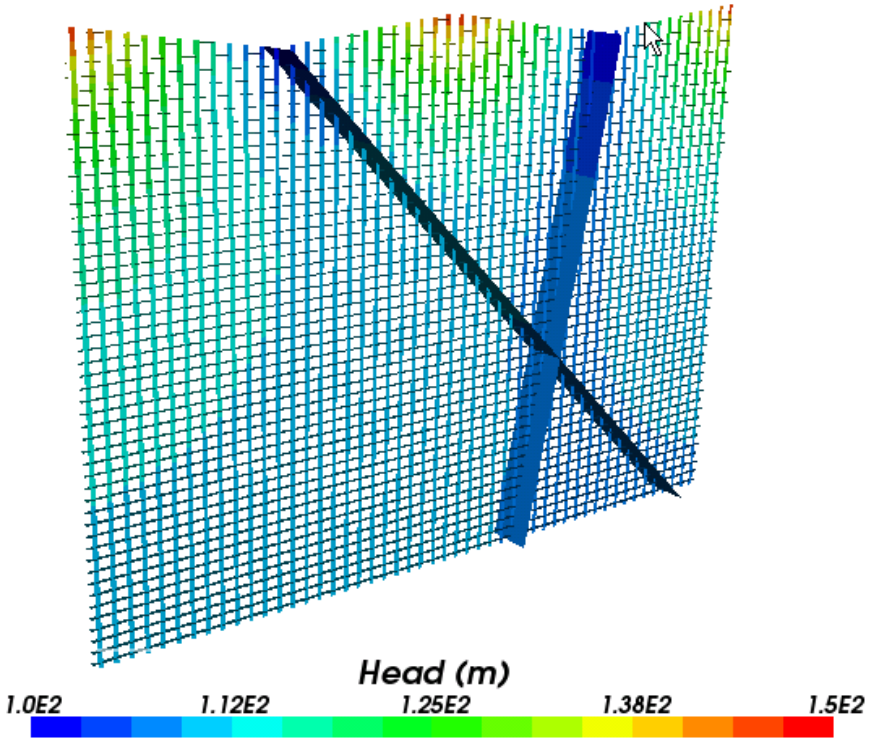

Figure 3-27 Fractures coloured by head (IFZ Rock Matrix)

3.8 Henry's Salt Transport

3.8.1 Overview

This case considers salt water intrusion into a vertical slice of an isotropic homogeneous confined aquifer.

The variant modelled is a modified version of the original Henry's test case, as recommended in [xiv]. The modified case halves the fresh water inflow rate, which increases the sensitivity of the solution to the variation in density.

This case is the DFN equivalent of Case 0.

3.8.2 Problem Definition

A schematic of the test case is shown in Figure 3-28 and the input parameters are given in Table 3-25.

Figure 3-28 Schematic illustration of the Henry test case

Table 3-25 Input parameters

Symbol	Parameter	Value
K	Hydraulic conductivity of rock	**1.0E-2 m/s**
D	Coefficient of molecular diffusion	**1.886E-5 m^2/s**
Q	Freshwater inflow per unit depth	**9.43E-5 m^2/s**
ρ_0	Reference density	**998 kg/m^3**
ρ_{max}	Saltwater density	**1023 kg/m^3**
α_L	Longitudinal dispersivity	**0 m**
α_T	Transverse dispersivity	**0 m**
ϕ	Porosity	**1**

The domain is represented by a single fracture tessellated into 0.025 m square sub-fractures. The fracture thickness is set to 1.8516E-4 m in order to generate the desired hydraulic conductivity of 1.0E-2 m/s.

The fracture has a porosity of 1.0 rather than 0.35 in [xiv]. The inflow rate is increased by a factor of 1/0.35 in order to account for this and to get the appropriate velocity field.

3.8.3 Variations

3.8.3.1 Interpolated Density

The density is interpolated from the CPM solution of test Case 0 and kept fixed throughout the calculation.

3.8.3.2 Salt Transport

The salt transport is modelled and the density calculated from the salinity.

3.8.4 Results

3.8.4.1 Interpolated Density

The interpolated density field used is shown in Figure 3-29.

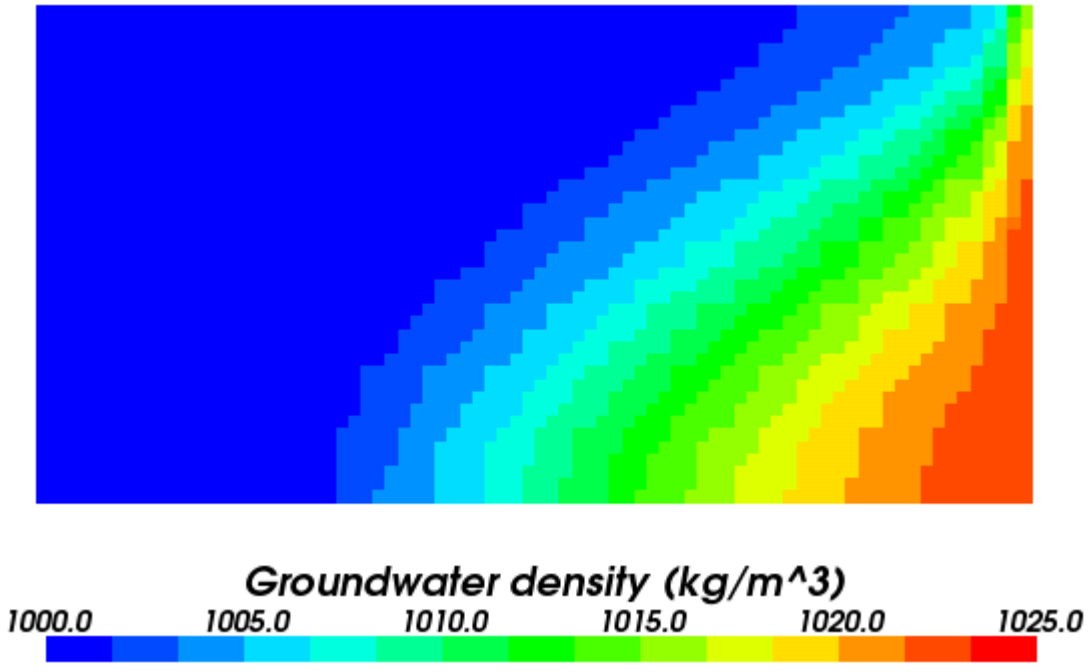

Figure 3-29 Interpolated density

The pressure field is compared against the reference CPM solution, the latter having been separately checked against the analytical solution via the salt concentration.

Plots of the two pressure fields are shown in Figure 3-30 and Figure 3-31. The pressure fields agree to within 5%.

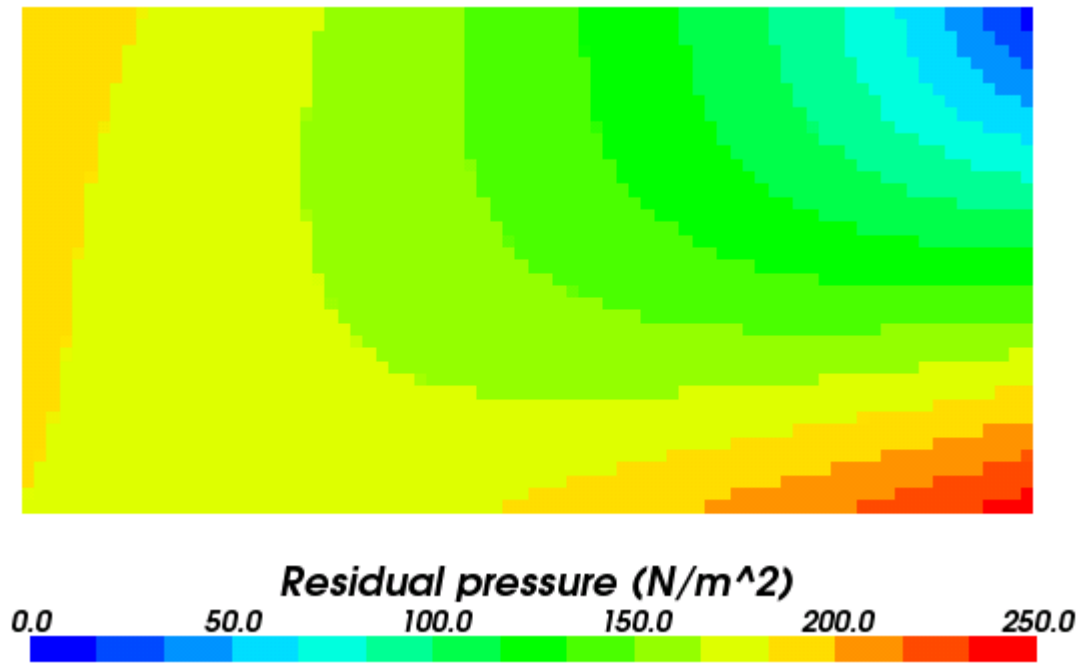

Figure 3-30 DFN residual pressure

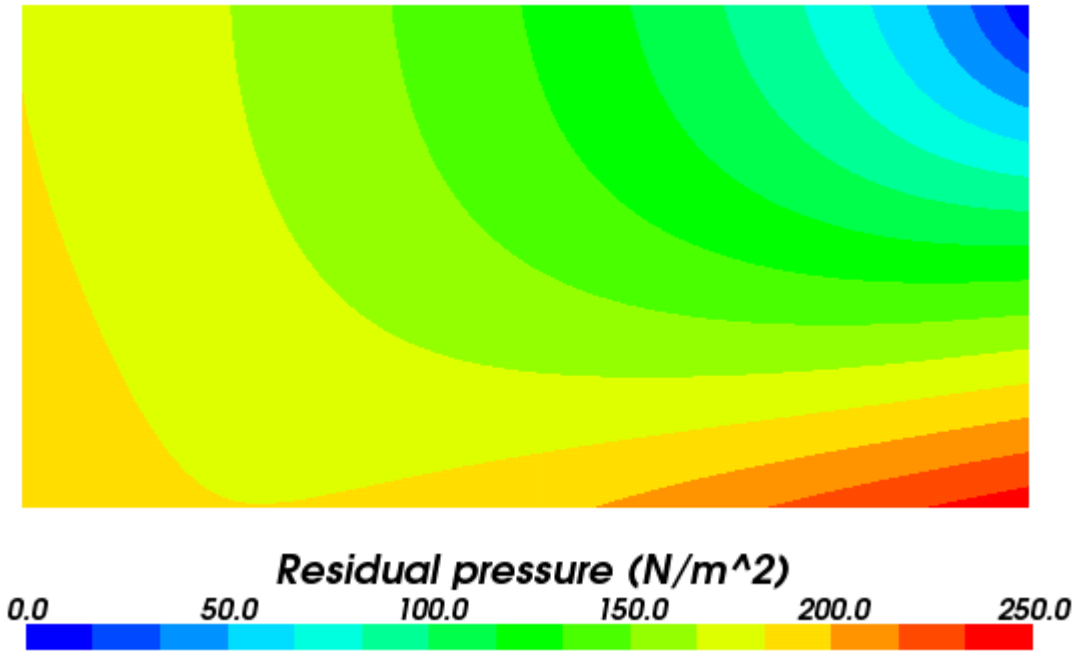

Figure 3-31 CPM Residual pressure

3.8.4.2 Salt Transport

This test case has an analytical solution, represented by an infinite double Fourier series. A truncated form of the series gives a non linear system which can then be iteratively solved. Results from this process are reported in [xiv] and these are used for comparisons in Figure 3-32. The maximum error in contour location is less than 2%.

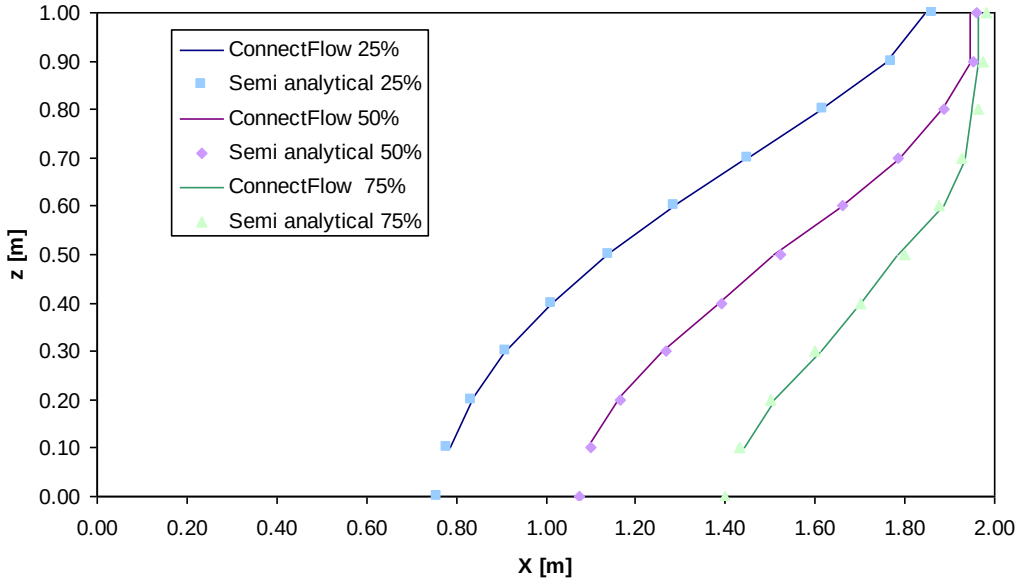

Figure 3-32 Non-dimensional concentration of salinity

3.9 Salt Transport

3.9.1 Overview

This case considers 1D transport of salt water due to a pressure gradient.

3.9.2 Problem Definition

A schematic of the test case is shown in Figure 3-33 and the input parameters are given in Table 3-26.

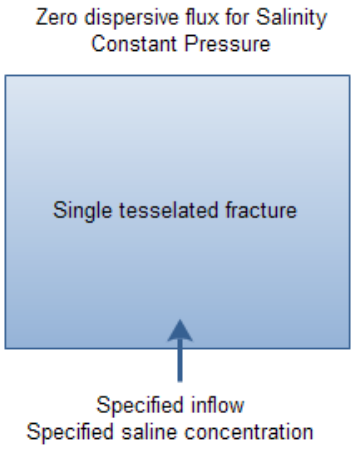

Figure 3-33 A schematic of the single fracture test case using an outflow (zero dispersive flux) boundary condition. The single fracture is 2 m wide and 1 m high, tessellated to a length of 0.025 m.

Table 3-26 Input parameters

Parameter	Value
Fracture transmissivity	**5.3E-6 m^2/s**
Freshwater inflow per unit depth	**3.49E-8 m^3/s**
Reference density	**1000 kg/m^3**
Saltwater density	**1025 kg/m^3**
Salinity dispersion	**1.886E-5 m^2/s**

The domain is represented by a single fracture tessellated into 0.025 m square sub-fractures. The fracture transmissivity is set to 5.3E-6 m^2/s. The fracture initially contains fresh water throughout, and saline water is introduced through its bottom edge. The boundary conditions are zero dispersive flux and a constant pressure on the top surface, and no flow on the sides of the fracture.

3.9.3 Results

A steady state salt transport calculation was carried out, the anticipated solution being a constant salinity of 1.0 throughout the model. Results agreed with this solution to within 2%.

3.10 Salt Upconing

3.10.1 Overview

This case considers the upconing of salt water into a tunnel in the centre of a thin 3D model (representing a 2D case). To verify the case, equivalent CPM and DFN calculations were carried out to ensure that they produced consistent results.

3.10.2 Problem Definition

A schematic of the test case is shown in Figure 3-34 and the input parameters are given in Table 3-27.

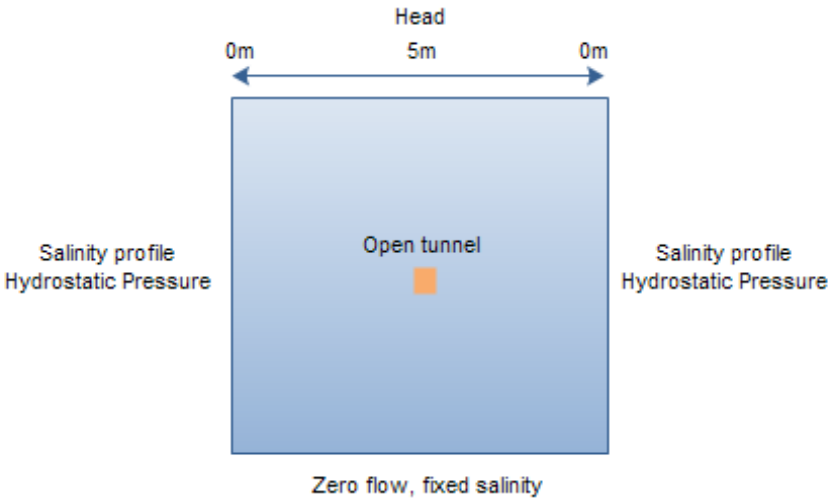

Figure 3-34 Model of a vertical cross-section, 800 m high and 1200 m wide. The open tunnel is 3 m wide and 4 m high.

Table 3-27 Salt transport input parameters

Symbol	Parameter	Value
K	Hydraulic conductivity (CPM) Equivalent hydraulic conductivity (DFN)	$K = \begin{cases} 3.9\,10^{-8}\ m/s & 0 > z \geq -50, \\ 1.6\,10^{-9}\ m/s & -50 > z \geq -150, \\ 1.2\,10^{-10}\ m/s & -150 > z \geq -400, \\ 1.8\,10^{-11}\ m/s & -400 > z \geq -800. \end{cases}$
ϕ	Porosity	$\varphi = \begin{cases} 7.90\,10^{-5} & 0 > z \geq -50, \\ 2.70\,10^{-5} & -50 > z \geq -150, \\ 1.1510^{-5} & -150 > z \geq -400, \\ 6.11\,10^{-6} & -400 > z \geq -800. \end{cases}$
D	Coefficient of molecular diffusion	**1.0E-6 m²/s**
ρ_0	Reference density	**998.217 kg/m³**
ρ_{max}	Saltwater density	**1042 kg/m³**

Symbol	Parameter	Value
α_L	Longitudinal dispersion length	**3 m**
α_T	Transverse dispersion length	**1 m**

To ensure that the same parameters are used in both cases, the conductivities are converted to transmissivities to be input to the DFN. The tunnel is represented by a void in the model, with a depth range of 400 m to 404 m in the centre of the model.

There is zero dispersive flux at the tunnel and a residual pressure of -4.0E6 Pa (atmospheric pressure). The specified initial condition is a depth-dependent salinity, equivalent in both cases. This has a salinity of:

$$s = \begin{cases} -5.172\,10^{-4} z & 0 > z \geq -400, \\ 1 - 1.983\,10^{-3}(z + 800) & -400 > z \geq -800. \end{cases}$$

The salinity profile used as the boundary condition uses the same values.

In order to achieve convergence, the model requires a parameter-stepping technique be used: the first step has D = 1.0E-4 m^2/s, and the result is used as the initial condition for a step with D = 1.0E-6 m^2/s

3.10.3 Results

The results shown in Figure 3-35 (DFN) and Figure 3-36 (CPM) are a good match and demonstrate upconing of salt into the tunnel as anticipated.

Results for the model are taken in a central line from 405 m to 800 m depth at five-metre intervals (i.e. from just below the tunnel to the bottom of the model), as plotted in Figure 3-37. The CPM and DFN results agreed to within 10%, with the largest differences close to the tunnel.

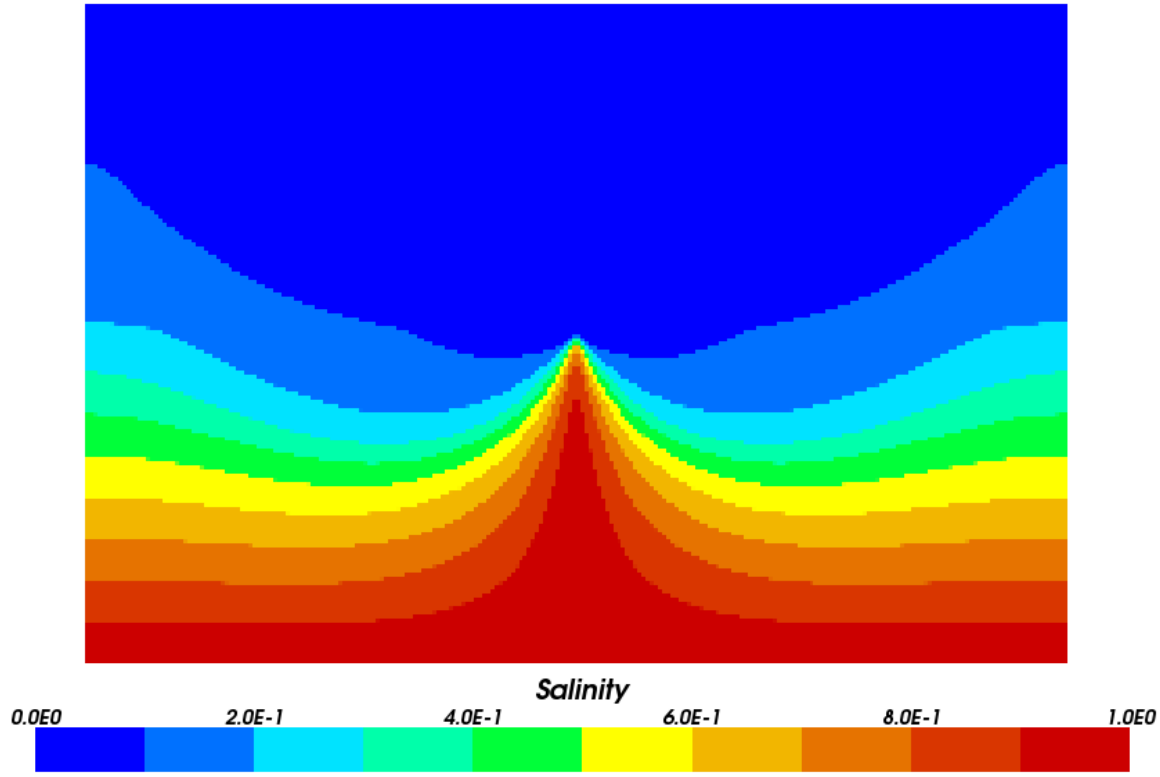

Figure 3-35 DFN Salinity profile

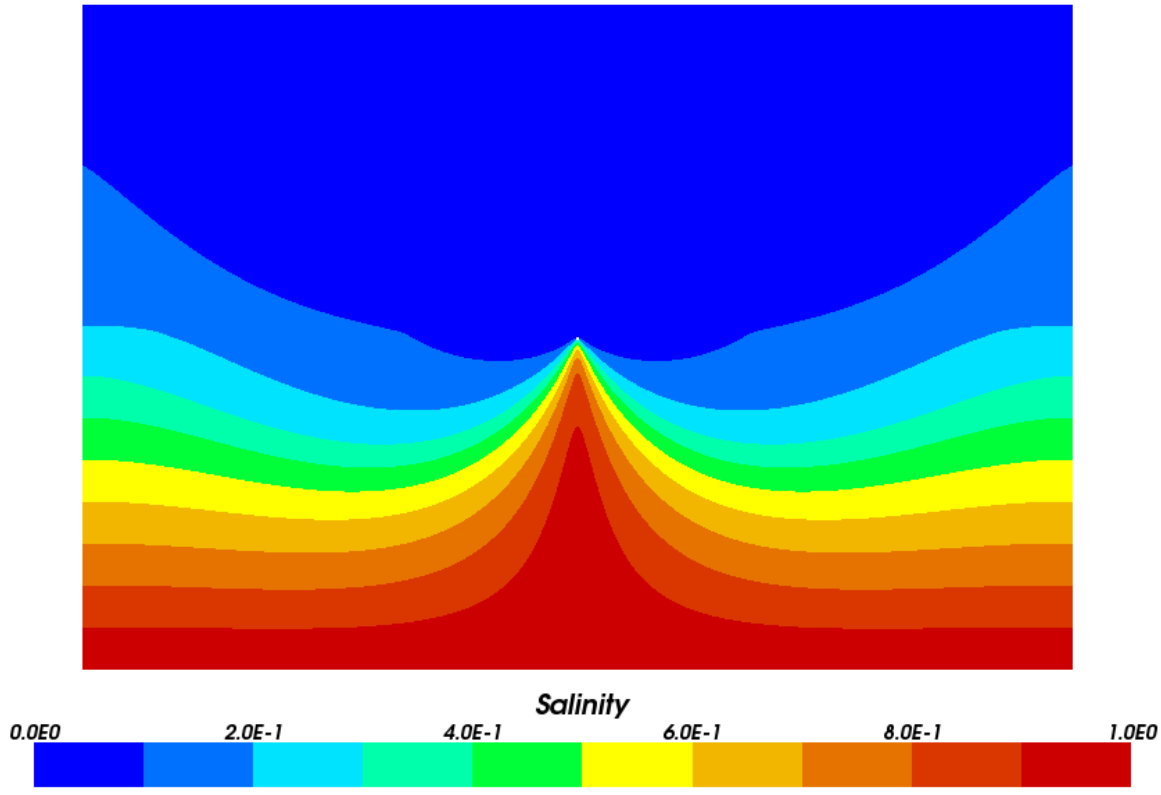

Figure 3-36 CPM Salinity profile

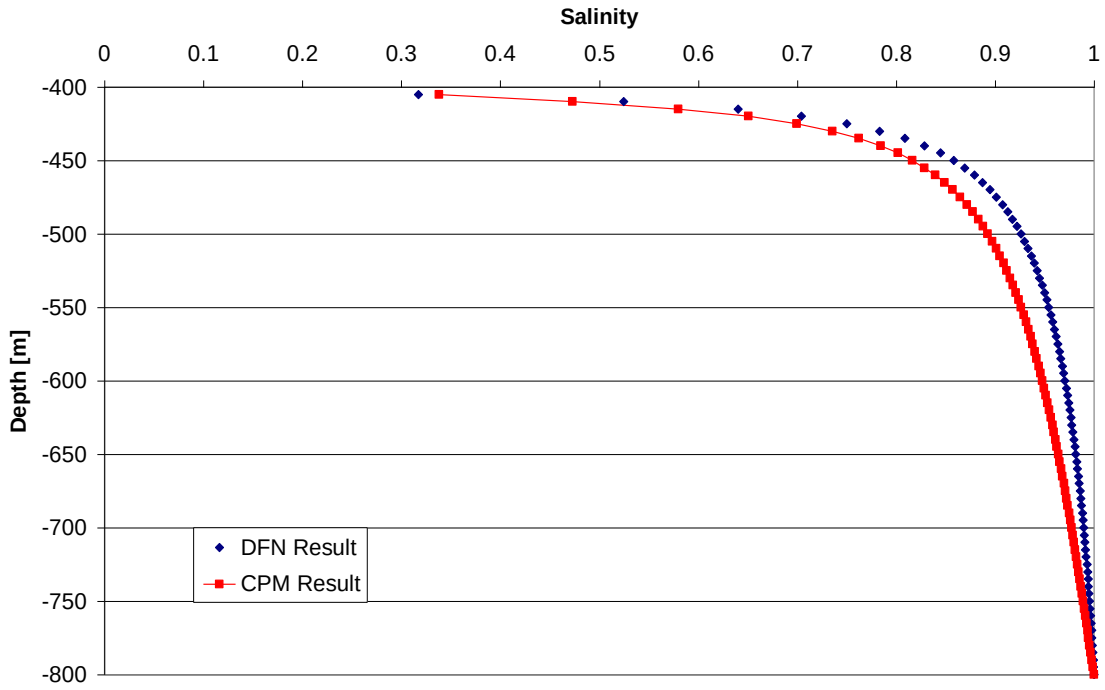

Figure 3-37 Difference between CPM and DFN results in the upconing case.

3.11 Grouting of a fracture – surface intersection

3.11.1 Overview

The grouting of the intersection of a single fracture and an external surface can be solved analytically and is used for verification of the implementation of a grouting model.

3.11.2 Problem definition

Grouting of fractures can be specified in a variety of manners. In this case a grouting efficiency (e) of 90% is used. That is, the flow after applying the grout is reduced by a factor of 10. In terms of hydraulic aperture this means a reduction of aperture by a factor f,

$$f = (1\text{-}e)^{1/3} = 0.464.$$

The model is defined as follows.

The region is a simple rectangular region with the coordinates specified in Table 3-28.

Table 3-28 Region coordinates for fracture-surface intersection grouting

	(m)
Top	0
Bottom	−10
Left	−5
Right	5
Front	−5
Back	5

One 'known' fracture is added in the yz plane, connecting the top and bottom, with a width (w) of 2.0 m. The height (h) is the distance between the intersections at the top and bottom surfaces, i.e. 10.0 m.

The pressure boundary condition at the top is zero and at the bottom it is

$$P = \rho\, g\, (h - s),$$

where ρ is the fluid density (1000 kg/m^3), g the gravitational acceleration (9.81 kg m/s^2) and s is a parameter to specify an overpressure.

For this simple problem, the Darcy flow equation can be solved explicitly and the solution is:

$$Q = -(T\, w / \rho\, g)\, (\Delta P - \rho\, g),$$

or, with the pressures shown as above:

$$Q = T\, w\, s / h,$$

where T is the transmissivity of the fracture. The ungrouted transmissivity is taken to be 10^{-4} m^2/s. The grouted transmissivity will be a factor of 10 smaller.

The overpressure parameter is 2.0 m. Note that the pressure boundary condition in a DFN model is specified in terms of residual pressure, so the value at the bottom is 19620.0 Pa.

3.11.3 Results

The results are presented in Table 3-29. The first column has the analytical results for the grouted and ungrouted flows out of the top surface .The second column is the result of a ConnectFlow calculation with the fracture untessellated and the last column is the same but with a tessellation length of 1.0 m, which leads to it being broken up into 20 tessellates. Note that a large penetration depth is used to assure that the whole fracture is grouted.

Table 3-29. Grouting results for fracture-surface intersection

	Analytical	Untessellated fracture	Tessellated fracture
Ungrouted	4.000E-5 m^3/s	4.000E-5 m^3/s	**3.997E-5 m^3/s**
Grouted	4.000E-6 m^3/s	4.000E-6 m^3/s	**3.997E-6 m^3/s**

3.12 Grouting of a fracture – fracture intersection

3.12.1 Overview

Fracture-fracture intersections will only be grouted if one of the factures belongs to a set of fractures representing some physical features, such as a tunnel, shaft or deposition hole.

3.12.2 Problem definition

The 'feature' is the horizontal fracture in the figure below. It is connected by a single fracture to the top surface and another to the bottom surface, as shown in Figure 3-38.

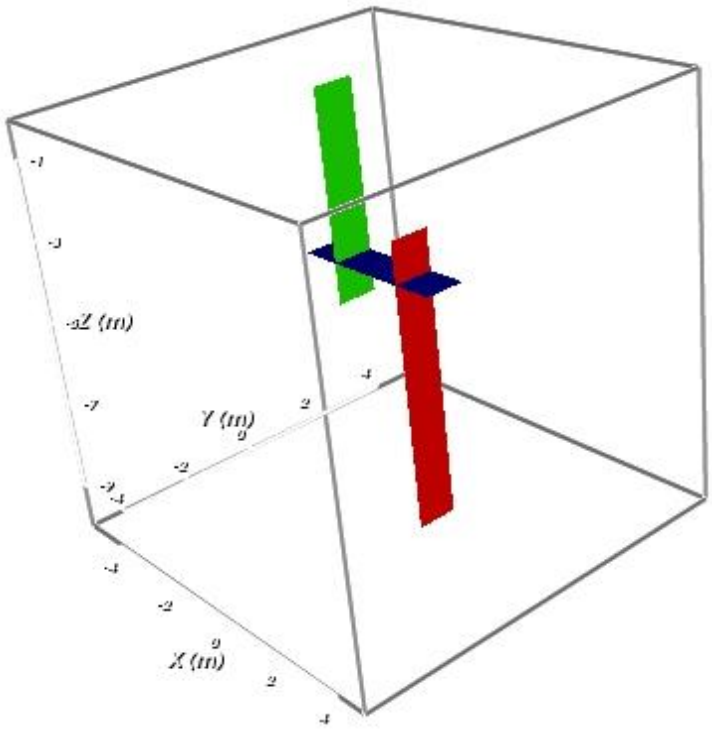

Figure 3-38. Fractures used for fracture-fracture intersection grouting

The model region is a simple rectangular volume with the coordinates specified in Table 3-30.

Table 3-30. Region coordinates for fracture-fracture intersection grouting

	(m)
Top	0
Bottom	-10
Left	-5
Right	5
Front	-5
Back	5

The Darcy flow equation for this system can be solved explicitly. The parameters used are indicated in the vertical slice in Figure 3-39.

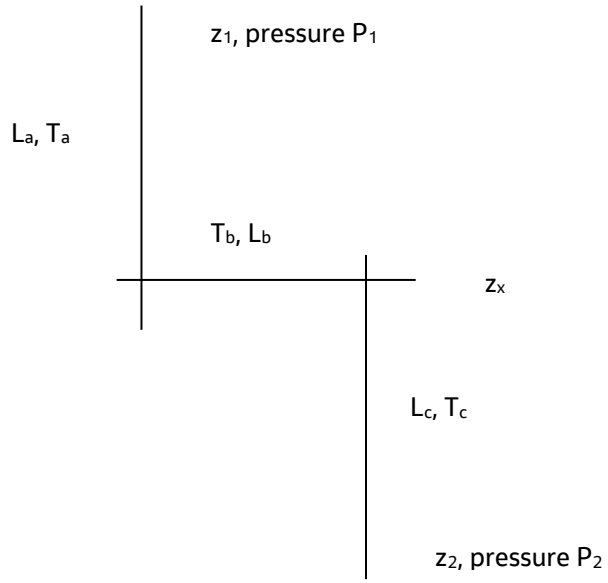

Figure 3-39. Parameters used for fracture-fracture intersection grouting shown on a vertical slice through the fractures

In terms of these z-coordinates (z), lengths between intersections (L), pressures (P) and transmissivities (T) the solution for the outflow at the top is:

$$Q = (P_1 - P_2 + \rho\, g\, (L_a + L_c)) \,/\, ((\rho\, g \,/\, w)\, (L_a/T_a + L_b/T_b + L_c/T_c)),$$

where w is the common width of all fractures. With the following choices:

$$L_a + L_b = L_c,$$

$$T_a = T_b = T,$$

$$T_c = f\, T \; (f = 1.0 \text{ or } 0.1),$$

$$P_2 = P_1 + h\, \rho\, g,$$

$$P_1 = 0.0,$$

this reduces to

$$Q = w\, T\, (L_a + L_c - h) \,/\, ((1+1/f)\, L_c).$$

Note that h is a parameter, not the distance between top and bottom. A value of h = 12.0 m is used to give an overpressure of 2.0 ρ g. Note that the pressure boundary condition in the DFN model is specified in terms of residual pressure, so a value 19620.0 Pa is used at the bottom.

3.12.3 Results

The results are presented in Table 3-31. The first column contains the analytical results corresponding to the values:

$$w = 1.0 \text{ m}$$

$$T = 1.0\ 10^{-5}\ m^2/s$$

$$L_a = 4.0 \text{ m}$$

$$L_c = 6.0 \text{ m}$$

$$f = 1.0 \text{ (ungrouted) or } 0.1 \text{ (grouted)}$$

A large penetration depth is assumed to ensure that the whole of each fracture is grouted. The second column presents the results for a ConnectFlow run with these parameters. The third column represents the same problem but with the external surface split up by planes parallel to the xz plane, using 29 subdivisions in the region specification. This leads to the intersection on the top surface being broken up into 4 intersection segments (not all the same size).

Table 3-31. Grouting results for fracture-fracture intersection

	Analytical	Simple region	Subdivided region
Ungrouted	1.667E-6 m^3/s	1.667E-6 m^3/s	**1.647E-6 m^3/s**
Grouted	3.030E-7 m^3/s	3.101E-7 m^3/s	**3.000E-7 m^3/s**

3.13 Transient Salt Diffusion

3.13.1 Overview

This case considers diffusion of salinity in a fracture (representing a 1D case) with no flow. The case was verified by comparison with an analytic solution to the 1D diffusion equation in a region with reflecting boundaries, given by:

$$C(x,t) = \frac{C_0}{\sqrt{4\pi D(t+t_i)}} \sum_{n=-\infty}^{\infty} \exp\left[\frac{-(x-x_0+nL)^2}{4D(t+t_i)}\right]$$

where C(x,t) is the salinity at position x and time t, D is the diffusion coefficient, L is the domain length, x_0 is the position of the peak, and t_i is the initial time position of the peak. C_0 is a measure of how much salinity is in the region - essentially a scale factor for the area under the curve, with units of metres. C_0 and t_i allow us to tune the initial profile such the initial salinity peak has a sensible value and shape. The sum over n represents reflections at the boundary. We only take this sum to ±3 because the higher-n the terms become vanishingly small as n increases, and to save on calculation. For the initial salinity profile only the n=0 component is used.

This case tests the diffusion part of transient salt transport calculations.

3.13.2 Problem Definition

A schematic of the test case is shown in Figure 3-40 and the input parameters are given in Table 3-32

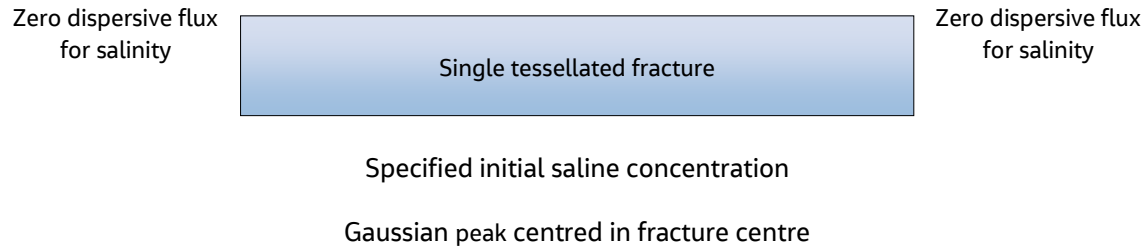

Figure 3-40 Model of domain, 2 m long and 0.05 m wide.

The domain consisted of a single fracture tessellated into 300 subfractures.

Table 3-32 Salt transport input parameters

Symbol	Parameter	Value
T	Transmissivity	**1.00E-4 m²/s**
D	Coefficient of molecular diffusion	**1.00E-3 m²/s**
ρ_0	Reference density	**1000 kg/m³**
ρ_{max}	Saltwater density	**1025 kg/m³**
α_L	Longitudinal dispersion length	**0.05 m**
α_T	Transverse dispersion length	**0.02 m**
C_0	Initial salinity	**0.12 m**

Symbol	Parameter	Value
t_i	Initial time	**1.2s**
x_0	Peak position	**1 m**
L	Domain length	**1.998 m**

There is no flow in the model (obtained by specifying the residual pressure to be 0 at both ends of the model) and zero flux boundary conditions for salinity at each end of the model. The specified initial condition is a Gaussian distribution for the salinity given by the n=0 component of the above equation.

$$C(x,t) = \frac{C_0}{\sqrt{4\pi D(t+t_i)}} \exp\left[\frac{-(x-x_0)^2}{4D(t+t_i)}\right]$$

A transient salt transport calculation was undertaken with timesteps of Δt=*0.01s* from *t=0* to *t=0.1s*, and Δt=*0.1* seconds from *t=0.1s* to *t=1*s, Δt=*1s* from *t=1* to *t=10s*, Δt=*10* seconds from *t=10s* to *t=100*s, and Δt=*100s* from *t=100* to *t=1000s*.

3.13.3 Results

The results shown in Figure 3-41 and Figure 3-42 show that the calculated results are in good agreement with the analytic solution given above. The results agree to within 5.5 %, with the largest difference being at the centre of the plume at time t=100 s.

Results for the model are taken on a line in x, through the centre of the fracture in the y and z dimensions.

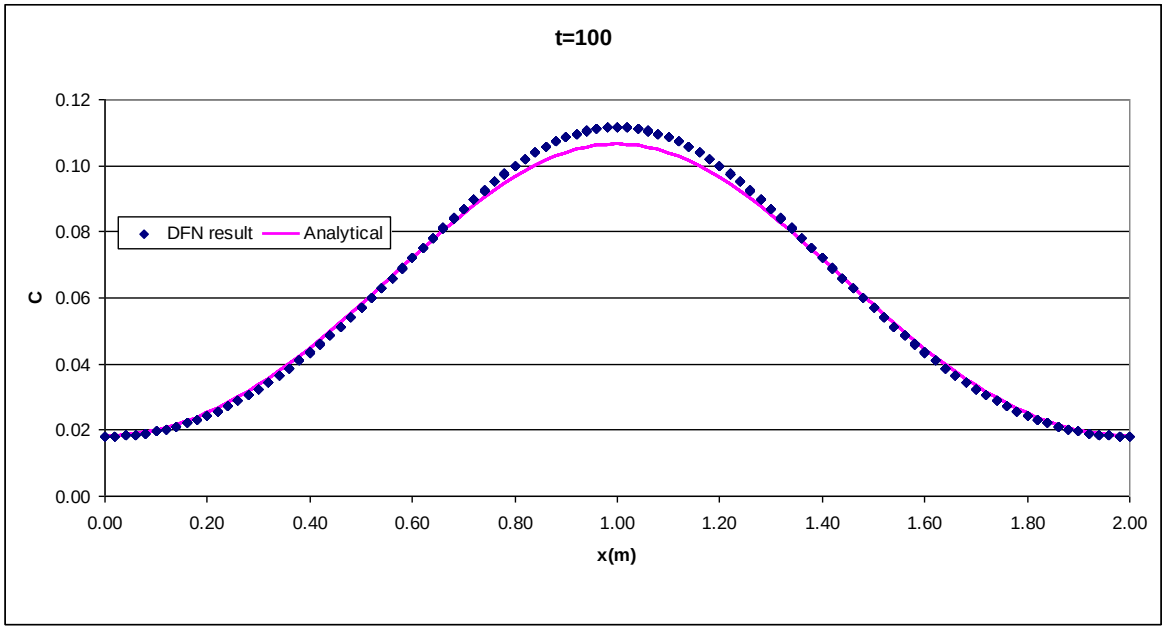

Figure 3-41 Comparison of calculated and analytic profiles at time t=100

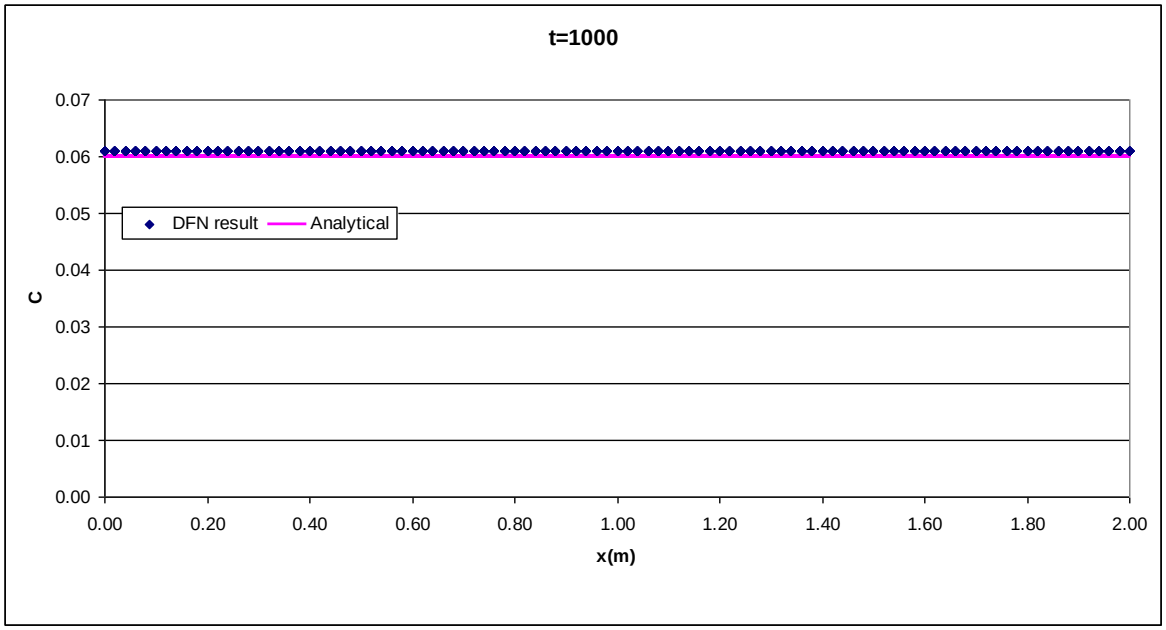

Figure 3-42 Comparison of calculated and analytic profiles at time t=1000

3.14 1D Advection of Salinity

3.14.1 Overview

This case considers advection of salinity in a fracture (representing a 1D case). The case was verified by comparison with a simple analytic solution which predicts the time taken for a saltwater/freshwater interface to flush out of the model. For a fracture which is initially full of saltwater with freshwater flowing in from one end, the time taken for the interface to flush is given by:

$$t = v / F_f$$

where v is the volume of the fracture, and F_f is the volumetric flow rate of freshwater into the fracture (m^3/s).

3.14.2 Problem Definition

A schematic of the test case is shown in Figure 3-43 and the input parameters are given in Table 3-33.

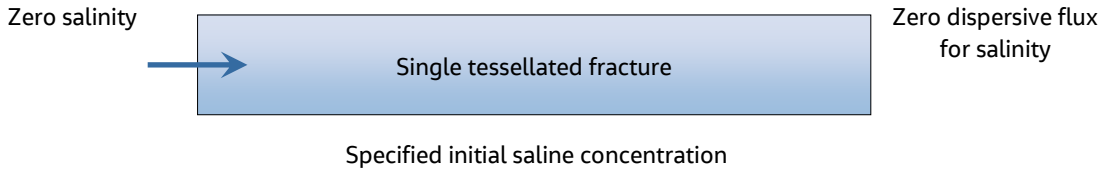

Figure 3-43 Model of domain 2 m long and 0.05 m wide.

Table 3-33 Salt transport input parameters

Symbol	Parameter	Value
T	Transmissivity	**1.00E-4 m^2/s**
a	Equivalent aperture	**4.97E-4 m**
D	Coefficient of molecular diffusion	**1E-9 m^2/s**
ρ_0	Reference density	**1000 kg/m^3**
ρ_{max}	Saltwater density	**1025 kg/m^3**
α_L	Longitudinal dispersion length	**0.0001 m**
α_T	Transverse dispersion length	**0.001 m**
J_s	Flux value at inflow model surface	**1.00E-3 $m^3/m^2/s$**
A	Model inflow surface area	**2.00E-2 m^2**
L	Fracture length	**1.998 m**
W	Fracture width	**0.05 m**

The domain consisted of a single fracture tessellated into 300 fractures.

There is a specified volumetric flux of 1.00E-3 $m^3/m^2/s$ at the left-hand end of the model, and a specified residual pressure of 0.00 Pa at the right-hand end. There is a specified salinity of C=0.0 at the left-hand end of the model and a zero dispersive flux boundary condition at the right-hand end. The initial condition for the salinity is that C=1.0 everywhere.

With the parameters described above, the analytical estimate for the time taken for the interface to flush from the fracture can be calculated. With $v = LWa$ and $F_f = J_s A$, the time taken $t = 2.48s$.

A transient calculation was carried out with timesteps of Δt=*0.1s* from *t=0* to *t=2.4s*, and Δt=*0.01* seconds from *t=2.4s* to *t=2.55s*.

3.14.3 Results

The results shown in Figure 3-44 and Figure 3-45 show that the calculated results are in good agreement with the analytic solution given above. The results agree to within 1%.

Due to the non-zero diffusion and dispersion lengths, there is a spreading of the saltwater/freshwater interface as time progresses. The interface location is taken to be the point at which salinity C = 0.5.This position is tracked by visualising the fracture with two colour bands, blue representing concentrations below 50% and red concentrations above 50%.

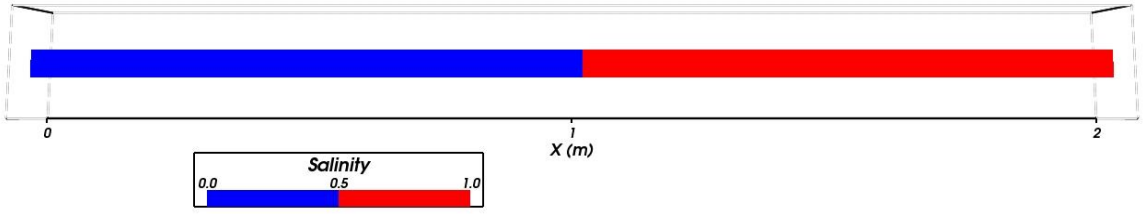

Figure 3-44 Salinity profile at time t=1.3s.

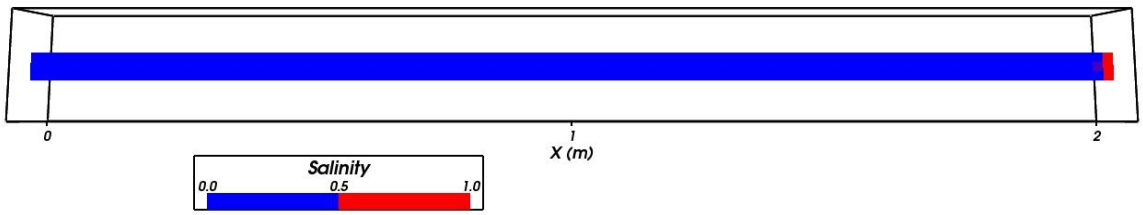

Figure 3-45 Salinity profile at time t=2.48 s

3.15 Transient Salt Upconing

3.15.1 Overview

This case considers transient upconing of salt water into a tunnel in the centre of a fracture (representing a 2D case). The results of the test case were verified by comparison with an analytic solution given by Dagan and Bear [xxix], which predicts (for small displacement) the shape of the upconed salt plume and the peak displacement of the saltwater/freshwater interface at a given time. A further check is made by verifying that the results at long time tended to the steady-state DFN calculation.

3.15.2 Problem Definition

A schematic of the test case is shown in Figure 3-46 and the input parameters are given in Table 3-34.

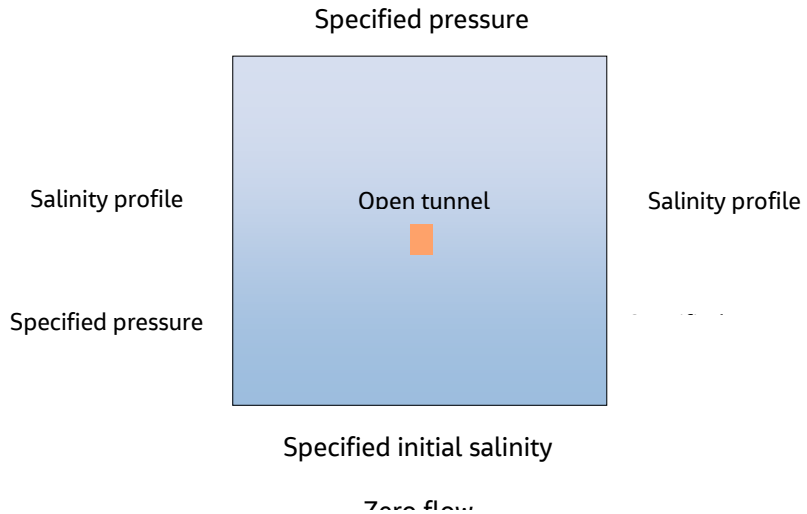

Figure 3-46 Model of a vertical cross-section, 800 m high and 1200 m wide. The open tunnel is 3 m wide and 4 m high.

Table 3-34 Salt transport input parameters

Symbol	Parameter	Value
K	Effective hydraulic conductivity of model (for comparison with analytic solution)	**2.012E-5 m/s**
a	Fracture aperture	**4.969E-6 m**
D	Coefficient of molecular diffusion	**1.0E-9 m^2/s**
ρ_0	Reference density	**988.217 kg/m^3**
ρ_{max}	Saltwater density	**1042 kg/m^3**
α_L	Longitudinal dispersion length	**2.0 m**
α_T	Transverse dispersion length	**0.5 m**
F	Mass flux at the tunnel	**6.32 E-6 $kg/m^2/s$**
A	Surface area of tunnel	**1.4 m^2**

The tunnel is represented by a void in the model, with a depth range of -400m to -404m in the centre of the model.

The boundary conditions for residual pressure are set to current value on the left-hand, right-hand and top boundaries, with an initial pressure condition set such that there is a small crossflow from left to right. The boundary conditions for salinity are set to current value on the left-hand, right-hand, top and bottom boundaries, with an initial condition set such that concentration is 0 between z=0 and z=-600m, and1 between z=-600m and z=-800m (the bottom quarter of the fracture). At the tunnel the boundary condition for salinity is set to zero dispersive flux. There is a constant mass flux boundary condition at the tunnel to represent an outflow.

A transient calculation was undertaken with a timestep beginning with Δt=4.0E7 s between t=0 and t=2E8 s, and with Δt=8.0E7 s between t=2E8 s and t=6E8 s.

3.15.3 Results

The results shown in Figure 3-47, Figure 3-48 demonstrate the comparisons between DFN transient salt simulation and the predictions of the analytic solutions [xxix]. The rate of upconing is in agreement with the analytic solution. The literature suggests that the limit of applicability of the analysis occurs for peak displacements somewhere between d/4 and d/2, where d is the distance between the original interface and the tunnel. This supports the observation of discrepancies in peak height between the analysis and the DFN model that are visible in the later times of Figure 3-47, once the peak displacement passes 50m (with d = 200 m). Comparing the gradients of both sets of data up to the d/4, we find that:

$$\left.\frac{dz}{dt}\right|_{napsac} = 1.25E^{-6}$$

$$\left.\frac{dz}{dt}\right|_{analytical} = 1.08E^{-6}$$

where z is peak height. Comparing the area under the salinity interface for time t=3.2E7 (Figure 3-48), we find an error of 13.6%. This is likely due to the fairly coarse discretisation in the z coordinate leading to a poorly resolved peak for small displacements.

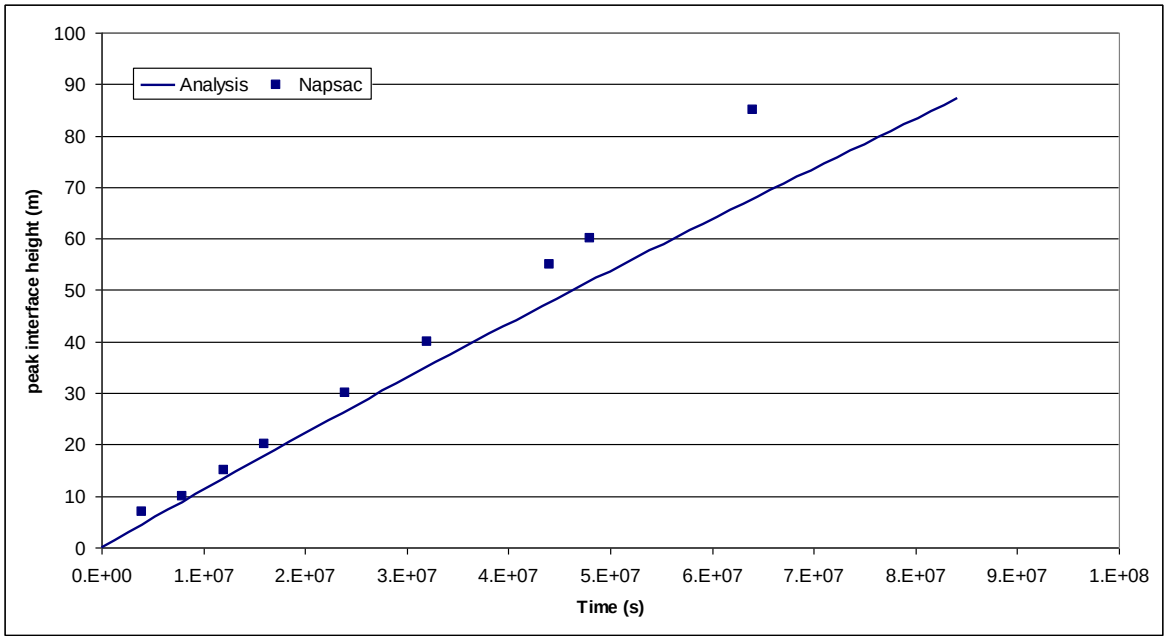

Figure 3-47 Peak interface height varying with time. Comparison between analytical result and transient DFN simulation.

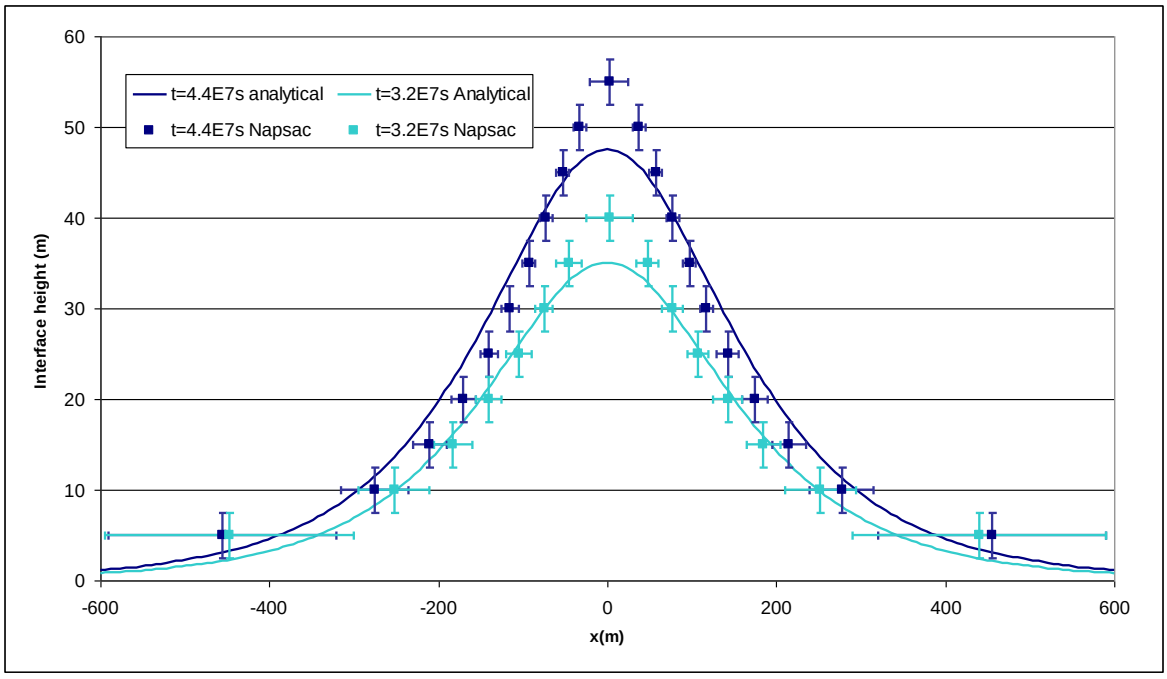

Figure 3-48 Interface height varying in x. Comparison between analytical result and DFN simulation at two different times (cf Figure 3-47)

Figure 3-49 and Figure 3-50 demonstrate upconing of salt into the tunnel as anticipated, with the long-term transient result showing good agreement with the steady state solution. The transient behaviour is also qualitatively similar to the case presented by Werner et al. [xxx], though a rigorous quantitative comparison is yet to be made.

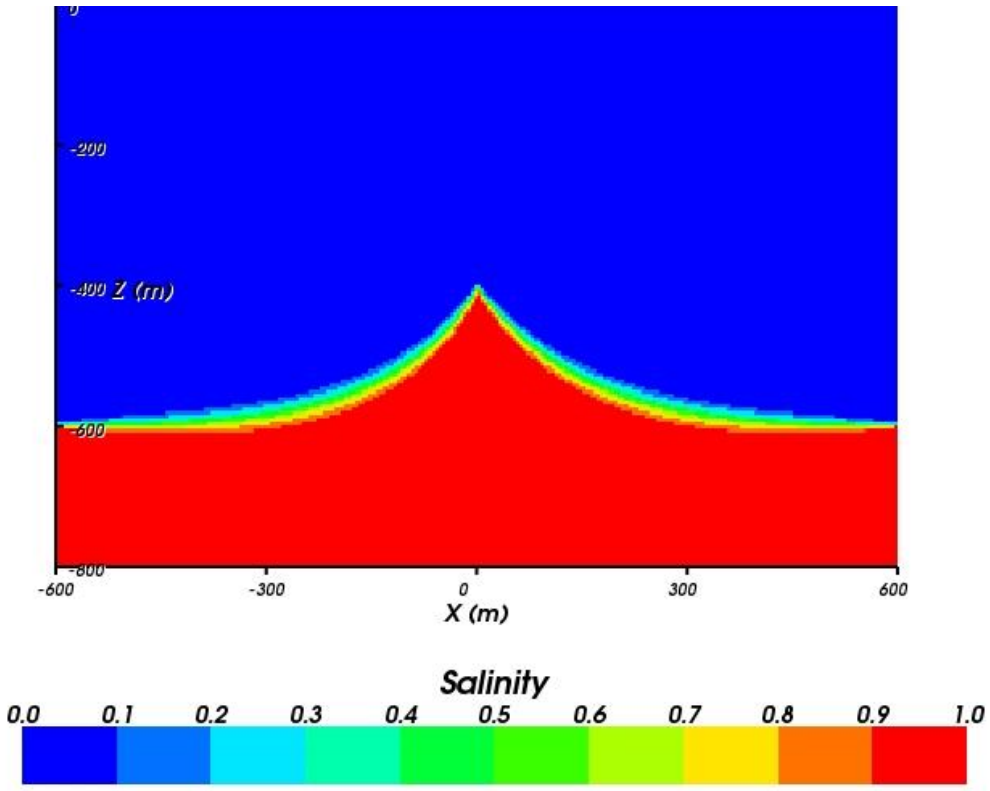

Figure 3-49 Salinity profile at time t=6.0E8 seconds.

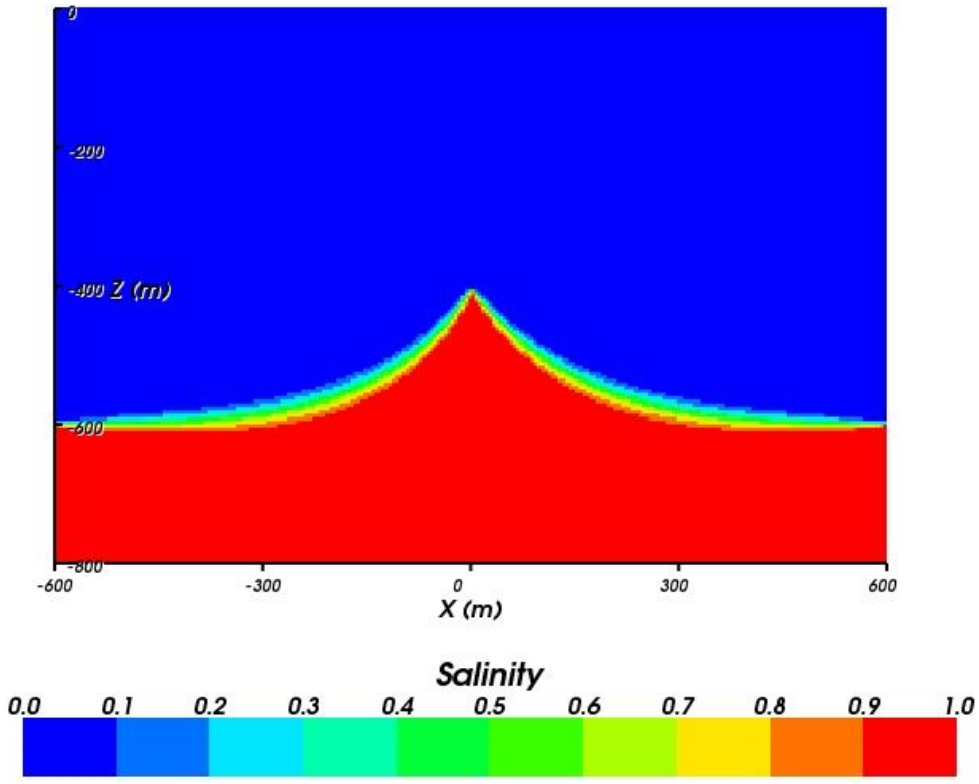

Figure 3-50 Steady state salinity profile

4. Combined DFN/CPM Verification

A summary of the DFN/CPM test cases is given in Table 4-1

Table 4-1 DFN/CPM verification tests

Case	Title	Overview
4.1	Radial steady state flow.	Steady state groundwater flow with a borehole used to apply the required mass flow boundary condition. The DFN/CPM interface is modelled using the Mass Lumped and Linearly Distributed options. Truncated variations of the domain are used to test current value boundary conditions in the DFN and CPM part of the model.
4.2	2D steady state flow	Steady state groundwater flow from a CPM region with anisotropic permeability to a DFN region.
4.3	2D steady state flow with particle tracks.	Particle tracking through steady state groundwater flow with varying permeability. Variations include mass-conserving and regular particle tracking.
4.4	2D variable density flow with particle tracks	Steady state groundwater flow with an imported spatially varying density field. Particle tracking using forward, backward, conservative and regular tracking options.
4.5	Henry's salt transport	Steady state groundwater flow. Density dependent on imported density field from CPM calculation.

4.1 Radial Steady State Flow

4.1.1 Overview

This case models steady groundwater flow in a 2D disk where water is removed from the centre at a constant rate and the outer disk boundary is maintained at a constant head.

4.1.2 Problem Definition

The problem definition and solution is taken from Feftra [iii] and is the DFN/CPM equivalent of case 0. The model domain is split up into two regions, fractured rock in the centre of the disk surrounded by porous medium rock, as is illustrated in Figure 4-1. The properties of the fractures and porous medium rock are selected such that the solution is the same as in case 0.

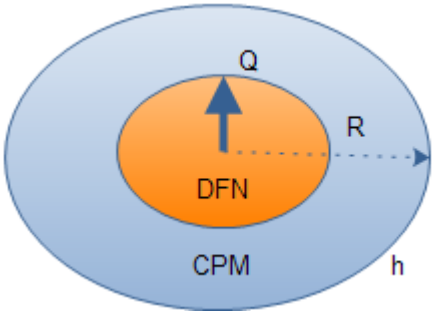

Figure 4-1 Schematic of problem definition

Table 4-2 Input parameters

Symbol	Parameter	Value
h	Head at r = R	**0 m**
Q	Outflow from disk	**8.17E-6 m^3/s**
K_f	Hydraulic Conductivity Fracture	**8.17E-3 m/s**
K_r	Hydraulic Conductivity Rock	**8.17E-7 m/s**
R	Radius of rock	**2000 m**
e	Aperture of fracture	**1.0E-4 m**
d	Thickness of disk	**1 m**
r	Radial distance from axis	**0-2000 m**
ρ	Density	**1000 kg/m^3**
μ	Viscosity	**1.0E-3 Pa.s**
g	Gravity	**9.8 m/s^2**

The product of the hydraulic conductivities and thickness are chosen to be constant across the domain, with the hydraulic conductivity of the fracture being derived from the fracture aperture as follows.

$$K_f = \frac{\rho g e^2}{12\mu}$$

The outflow rate is then set to make the solution the same as in 2.1.5.

4.1.3 Variations

The modelled domain consists of a 15 degree sector. The region r<1000 m is modelled as a planar tessellated fracture using the DFN model. The region 1000<r<2000 m is modelled as rock using the CPM model. The fractures and mesh are shown in Figure 4-2.

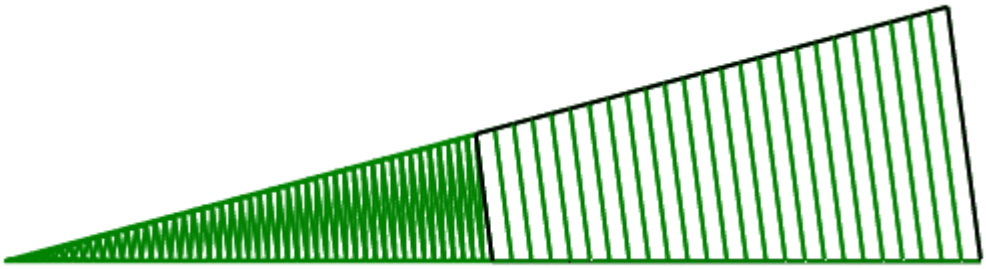

Figure 4-2 Fractures and CPM Mesh

4.1.3.1 Mass lumped ConnectFlow Fluxes

The interface between the two regions is modelled using the interface options, `CONSERVE FRACTURE FLUX` and `MASS LUMP NAPSAC FLUXES`.

4.1.3.2 Current Value in CPM Region

In this variant, the modelled domain is truncated at a radius of 1500 m, and the interpolated solution from the CPM case 2.1.3.1 is applied as a pressure boundary condition. The `MASS LUMP NAPSAC FLUXES` interface option is used.

4.1.3.3 Current Value in DFN Region

In this variant, the modelled domain is truncated at a radius of 250 m, and the interpolated solution from the CPM case 2.1.3.1 is applied as a pressure boundary condition. The `MASS LUMP NAPSAC FLUXES` interface option is used.

4.1.3.4 Linearly Distributed ConnectFlow Fluxes

The interface between the two regions is modelled using the default interface options, `CONSERVE FRACTURE FLUX` and `LINEARLY DISTRIBUTE NAPSAC FLUXES`.

4.1.4 Results

The analytical solution is given by

$$h(r) = h(R) - \frac{Q}{2\pi Kd}\ln(\frac{R}{r})$$

The results from DFN/CPM calculation show good overall agreement with the analytical solution, as illustrated in Figure 4-3 to Figure 4-6. The mass lumping method is more computationally efficient, but the linear distributed fluxes method gives a smoother and more accurate solution.

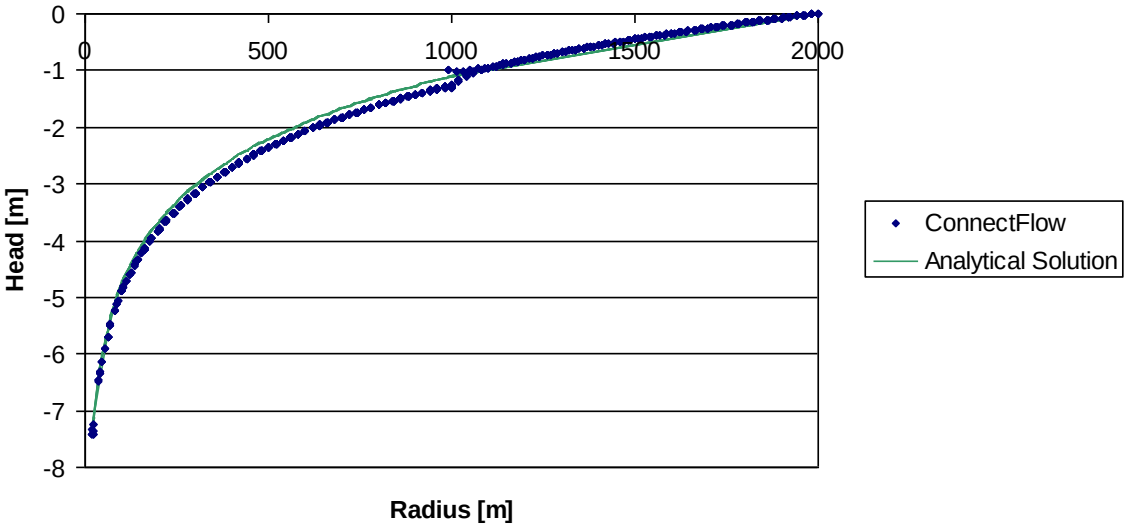

Figure 4-3 Variation of head with distance using a mass lumped DFN/CPM interface

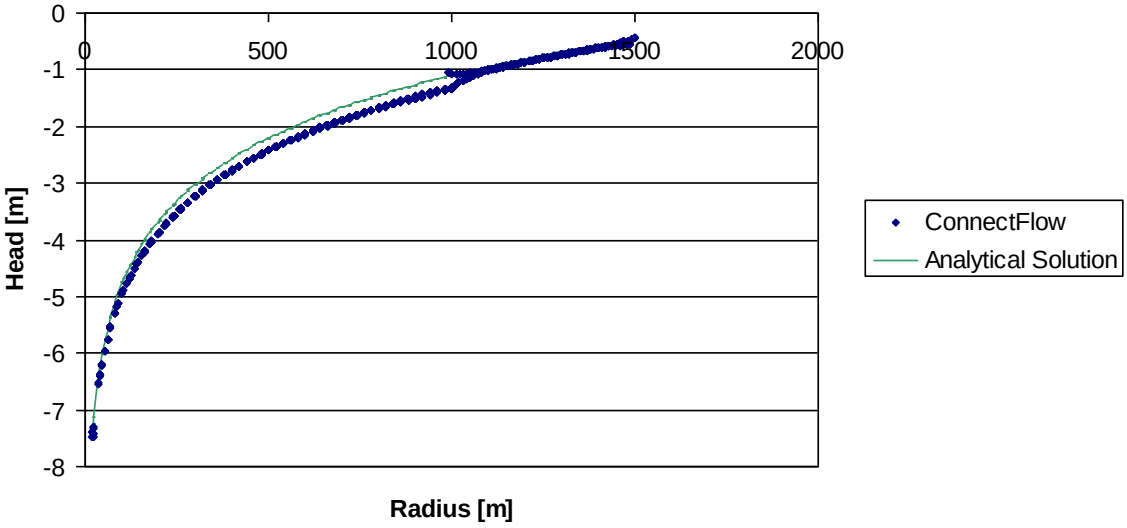

Figure 4-4 Variation of head with distance using a current value boundary in the CPM region and a mass lumped DFN/CPM interface

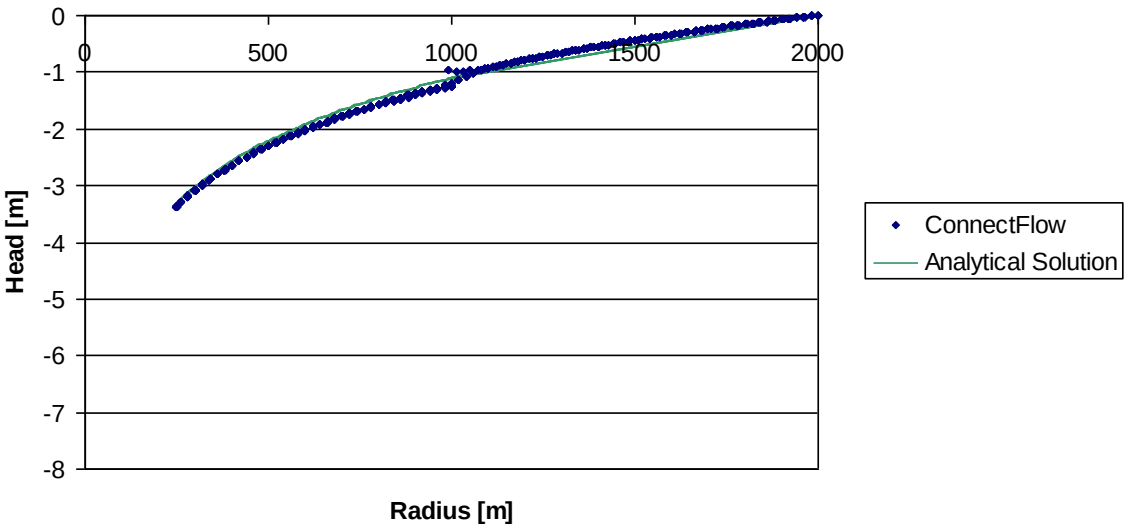

Figure 4-5 Variation of head with distance using a current value boundary in the DFN region and a mass lumped DFN/CPM interface

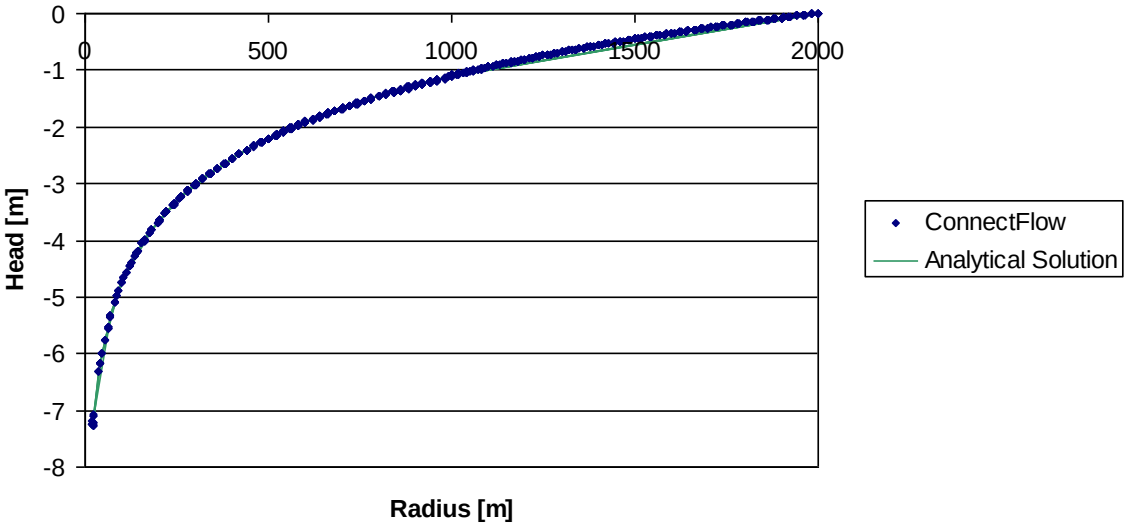

Figure 4-6 Variation of head with distance using a linearly distributed DFN/CPM interface

4.2 Flow to Fracture Network

4.2.1 Overview

This case models steady state groundwater flow in a simple two-dimensional fracture network where the flow enters the network through porous medium rock with anisotropic permeability.

4.2.2 Problem Definition

The problem is a variant of test 3.6, as illustrated in Figure 4-7.

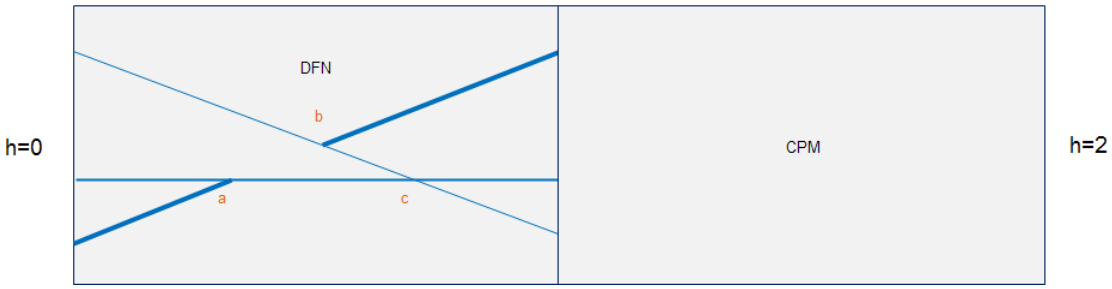

Figure 4-7 Schematic of problem definition

The fracture properties are the same as in Section 3.6.3.2.

The CPM properties are defined in such a way as to ensure the following conditions at the interface.

$$h_{DFN} = h_{CPM} = 1 \text{ m}$$

$$Q_{DFN} = Q_{CPM} = KA\nabla h$$

Where K is the hydraulic conductivity and A the cross sectional area of the CPM region.

The first equation defines the head gradient in the CPM region, and the second is then used in conjunction with the DFN analytical value of Q to obtain K.

As the flow needs to enter the DFN region through the three fractures, there will also be a vertical component to the flow in the CPM region. In order to avoid this impacting the head at the fracture inflows the vertical component or permeability is set to be 1000 times higher than the horizontal component.

4.2.3 Results

The calculated heads are all within 4% of the analytical solution.

Table 4-3 Heads at fracture intersections

Intersection	ConnectFlow	Analytical	% Error
a	0.062	0.061	**1.42%**
b	0.936	0.968	**3.36%**
c	0.598	0.600	**0.19%**

4.3 2D Steady State Flow with Particle Tracks

4.3.1 Overview

This case is taken from Level 3 of the international HYDROCOIN project for verification of groundwater flow codes [xxxi]. It models steady state flow in a two-dimensional vertical slice of rock, containing a circular region of higher permeability.

The case has a non-uniform analytical solution and is used in the HYDROCOIN study to test particle tracking.

This is the equivalent DFN/CPM test of Case 2.3.

4.3.2 Problem Definition

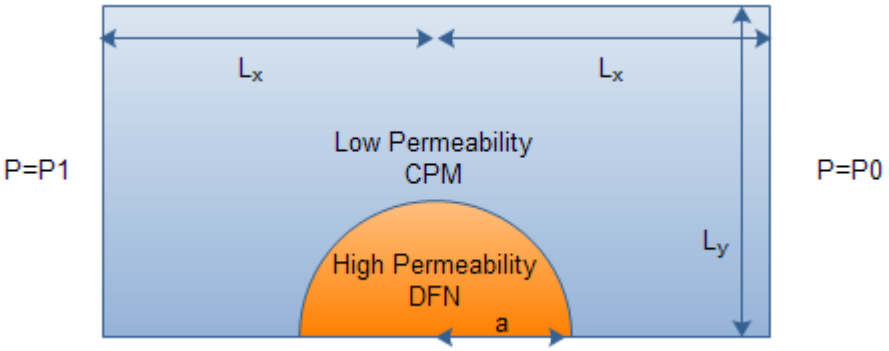

Figure 4-8 Schematic of problem definition

The DFN region is represented by a single tessellated fracture. In order to ensure that the solution is consistent with [xxxi], the following relations must hold.

Balancing the flow rate Q: $k_i d = k_f e$

Fracture permeability: $k_f = \frac{e^2}{12}$

Thickness available for flow: $d = e / \phi$

Taking ϕ from [xxxi], selecting d = 1 m and scaling the pressure gradient gives the values in Table 4-4.

Table 4-4 Input parameters

Symbol	Parameter	Value
Lx	Upstream and downstream distances	**250 m**
Ly	Vertical outer region distance	**240 m**
a	Radius of inner disk	**10 m**
P1	Upstream pressure	**3.0E-4 Pa**
P0	Downstream pressure	**-3.0E-4 Pa**
k_o	Permeability of outer region	**8.333E-7 m^2**
k_i	Permeability of inner region	**8.333E-5 m^2**
k_f	Fracture permeability	**8.333E-4 m^2**
e	Fracture thickness	**0.1 m**
d	CPM thickness	**1 m**
ϕ	Porosity	**0.1**
ϕ_f	Fracture Porosity	**1.0**
ρ	Density	**1000 kg/m^3**
μ	Viscosity	**1.0E-3 Pa.s**

Eight particle tracks are released 50 m upstream of the disk centre and at Y values of 10, 12, 14, 16, 18, 20, 22 and 24 m.

The analytical solution for the pathlines is given in the HYDROCOIN report [vii] as

$y = y_o /(1 + \frac{a^2}{r^2} \frac{(k_i - k_o)}{(k_i + k_o)})$ for r > a

$y = y_o \frac{(k_i + k_o)}{2k_o}$ for r < a

Where r is the distance from the centre of the disk and y_0 is a constant representing the height of the track a long distance away from the origin.

4.3.3 Variations

4.3.3.1 Regular Particle Tracking

Regular particle tracking was used within the CPM region. The mesh around the DFN region is shown in Figure 4-9.

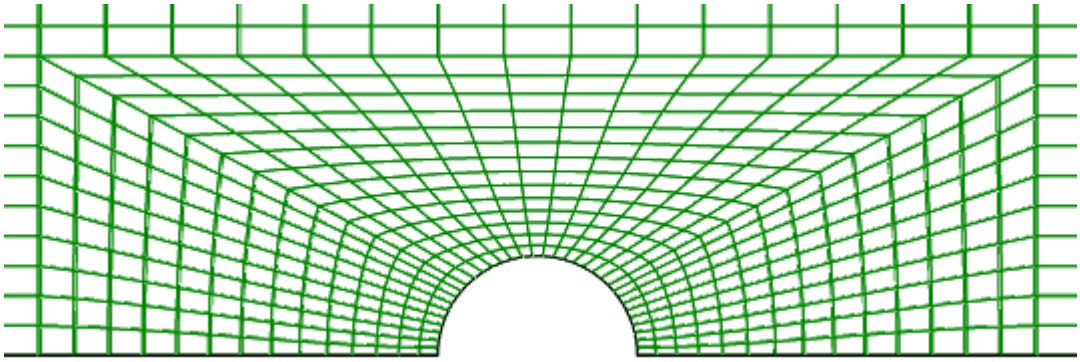

Figure 4-9 CPM wrapped mesh

The tessellated fractures within the inner region are shown in Figure 4-10.

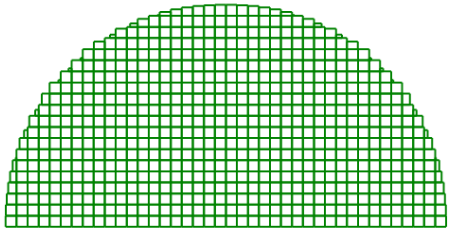

Figure 4-10 Tessellated fractures (larger scale image).

4.3.3.2 Mass Conserving Particle Tracking

Mass conserving particle tracking was used within the CPM region. The mesh around the DFN region is shown in Figure 4-11.

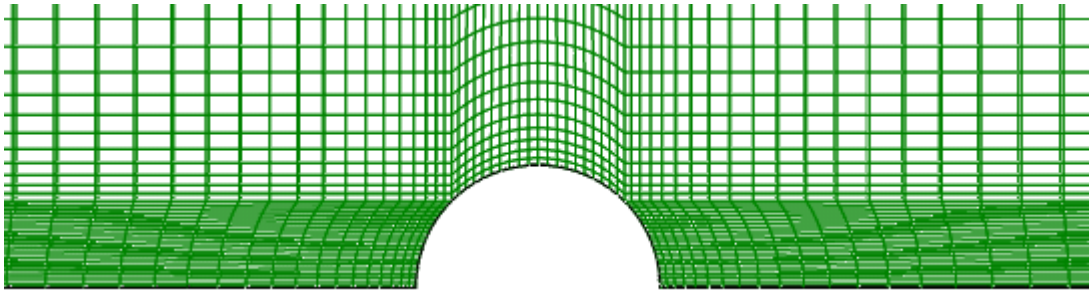

Figure 4-11 CPM regular mesh

The tessellated fractures within the inner region are shown in Figure 4-12.

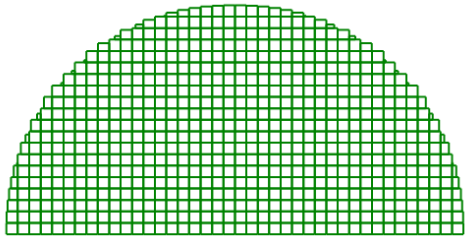

Figure 4-12 Tessellated fractures (larger scale image).

4.3.4 Results

The particle tracks within the DFN part of the model are treated in a stochastic manner, allowing different tracks to take different paths. Ten particles were released from each of the starting positions and the results for regular particle tracking are shown in Figure 4-13 and Figure 4-14.

For the tracks that do not pass through the DFN region, the results are within 1% of the analytical solution for the regular particle tracking, and within 2% of the analytical solution for the mass conserving particle tracking.

The stochastic tracks have more variation as expected, however the average tracks starting from each position also have a travel time and final location within 1% of the analytical solution for the regular particle tracks and within 2% of the analytical solution for the mass conserving particle tracking.

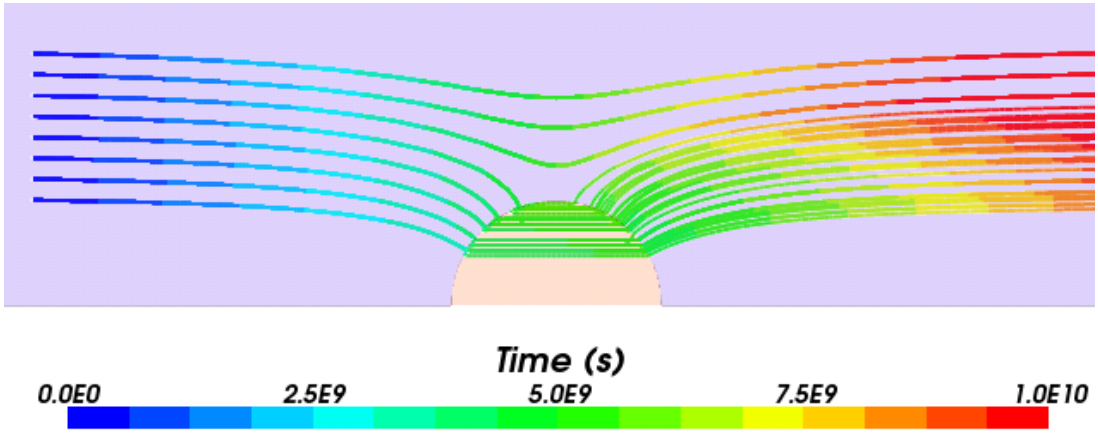

Figure 4-13 Regular particle tracks

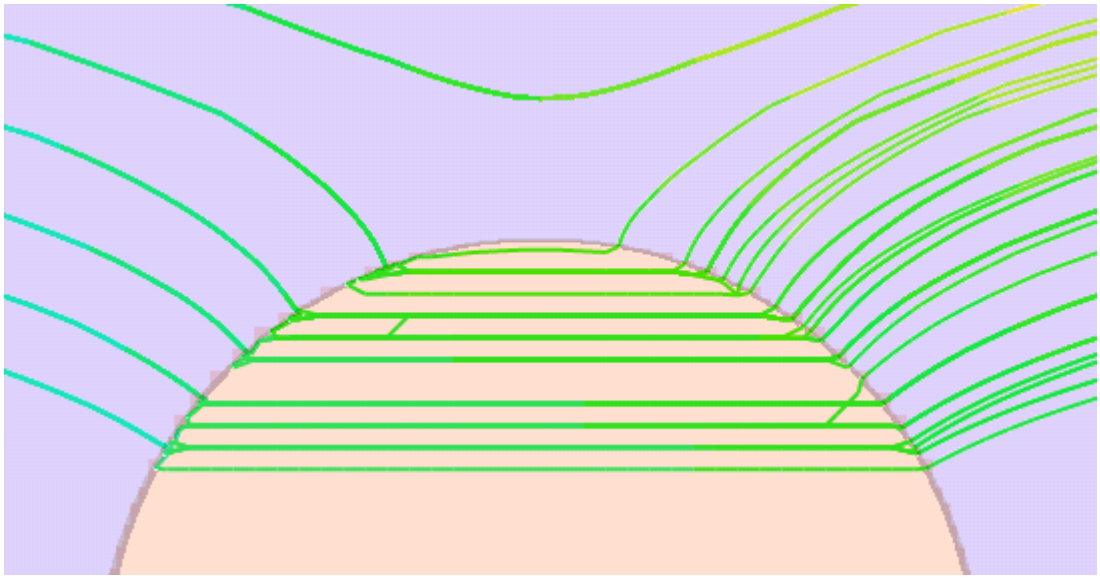

Figure 4-14 Stochastic behaviour of particle tracks

4.4 2D Variable Density Flow with Particle Tracks

4.4.1 Overview

This case uses a predefined density field, corresponding to an analytical flow solution. The resulting velocity field is used to test regular and mass conserving particle tracking.

4.4.2 Problem Definition

The modelled domain is shown in Figure 4-15. The analytical pressure field $y^2 - x^2$ is applied as a boundary condition on all four sides of the region and the density field xy is applied to the interior.

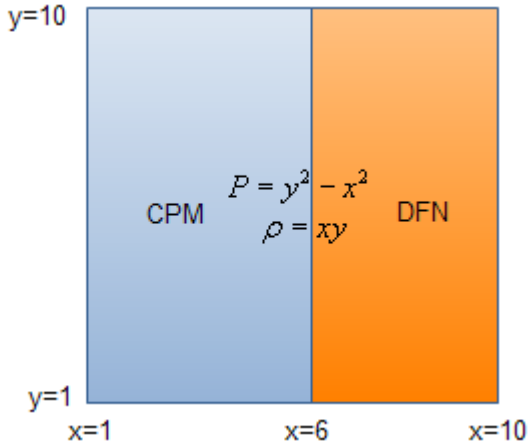

Figure 4-15 Schematic of problem definition

The DFN region is represented by a single tessellated fracture. In order to ensure that the solution is consistent with the CPM region, the following relations must hold.

Balancing the flow rate Q: $kd = k_f e$

Fracture permeability: $k_f = \frac{e^2}{12}$

Thickness available for flow: $d = e / \phi$

Taking e = 1.0E-5 and d = 1.0E-3 then gives the following values in Table 4-5.

Table 4-5 Input parameters

Symbol	Parameter	Value
k	Permeability of CPM region	**8.333E-14 m^2**
k_f	Fracture permeability	**8.333E-12 m^2**
e	Fracture thickness	**1.0E-5 m**
d	CPM thickness	**1.0E-3 m**
ϕ	Porosity	**0.01**
μ	Viscosity	**1.0E-3 Pa.s**

4.4.3 Variations

4.4.3.1 Forward Particle Tracking

This variant tracks 10 particles starting from the upper left hand corner of the CPM region at x=1.5, y = 9.5. The tracks subsequently pass through the DFN region where they behave in a stochastic manner, allowing different tracks to take different paths.

4.4.3.2 Backward Particle Tracking

This variant performs backward tracking on 10 particles ending at x=9.07, y=1.57 within the DFN region, which corresponds to the same analytical path as the forward track in variation 4.4.3.1.

4.4.3.3 Mass Conserving Particle Tracking

This variant tracks ten particles starting from x=1.5, y = 9.5 and uses the mass conserving particle tracking option. The tracks subsequently pass through the DFN region where they behave in a stochastic manner, allowing different tracks to take different paths.

4.4.4 Results

4.4.4.1 Analytical solution

Substituting the Darcy flow equation into the continuity equation gives

$$\nabla.(\rho\varphi\frac{k}{\mu}(\nabla P)) = 0$$

Gravity is omitted as $\frac{\partial\rho}{\partial z} = 0$.

Substituting in the proposed solution $\rho = xy$ and $P = y^2 - x^2$ then gives

$$\nabla.(xy(\nabla(y^2 - x^2)) = 0$$

which reduces to

$$\frac{\partial}{\partial x}(-2x^2 y) + \frac{\partial}{\partial y}(2xy^2) = -4xy + 4xy = 0$$

This confirms that $\rho = xy$ and $P = y^2 - x^2$ is a solution of the Darcy flow equations with variable density.

From the pressure field, the particle tracks can then be determined as $y = \frac{x_0 y_0}{x}$ where x_0, y_0 represents the starting location of the particle track. The corresponding travel time being $t = \frac{\mu\phi}{2k}\ln(\frac{x}{x_o})$.

4.4.4.2 Pressure and Density Fields

Figure 4-16 and Figure 4-17 show the pressure and density fields. The former being calculated and the latter being prescribed.

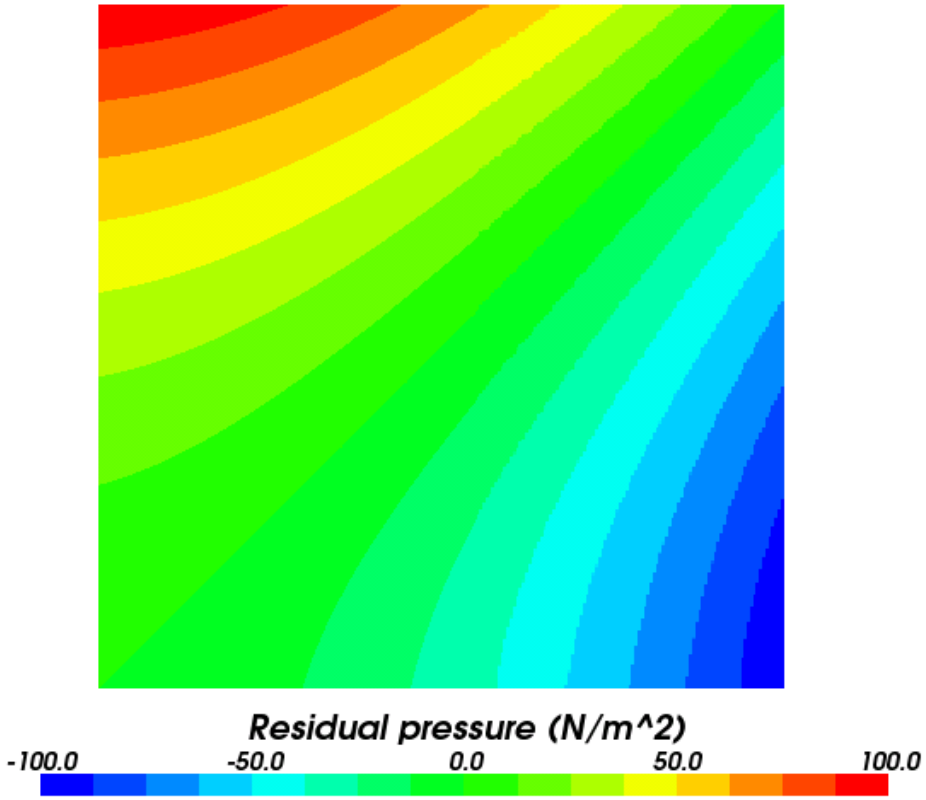

Figure 4-16 Calculated residual pressures.

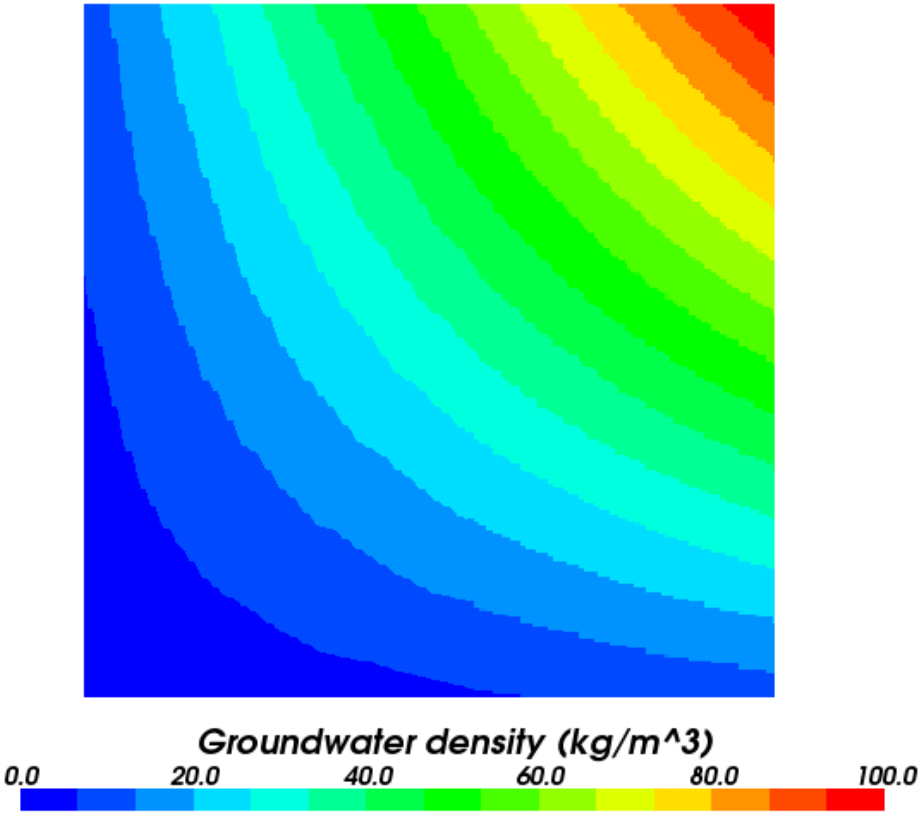

Figure 4-17 Applied densities.

4.4.4.3 Forward particle tracking

Figure 4-18 shows 10 particle tracks released from the top left corner of the CPM region. On entering the DFN region the tracks behave in a stochastic manner. The background of the plot is coloured by residual pressure.

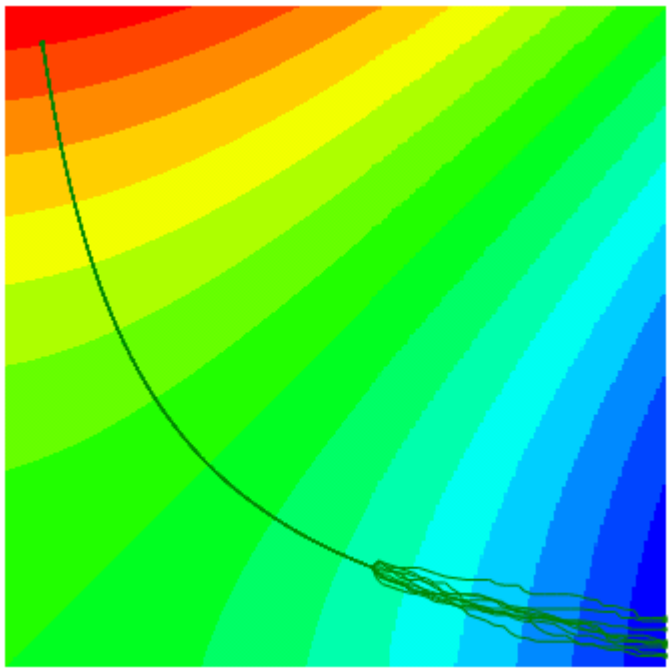

Figure 4-18 Forward particle tracks

An averaged particle track plot is compared against the analytical solution in Figure 4-19, the results agreeing to within 2% of the analytical solution for position and travel time. In order to predict travel times in the DFN region, it is necessary to set the model reference density to a value representative of that of the fluid which the track passes through.

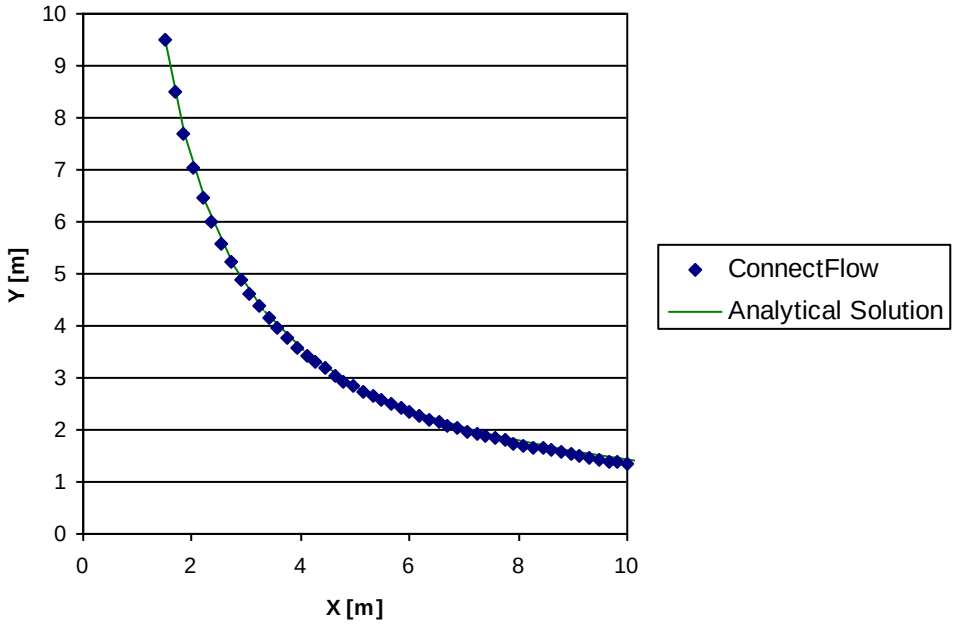

Figure 4-19 Averaged forward tracks

4.4.4.4 Backward Particle Tracking

Figure 4-20 shows 10 particle tracks tracked backwards from the lower right hand corner of the DFN region. Within the DFN region the tracks behave in a stochastic manner. The background of the plot is coloured by residual pressure.

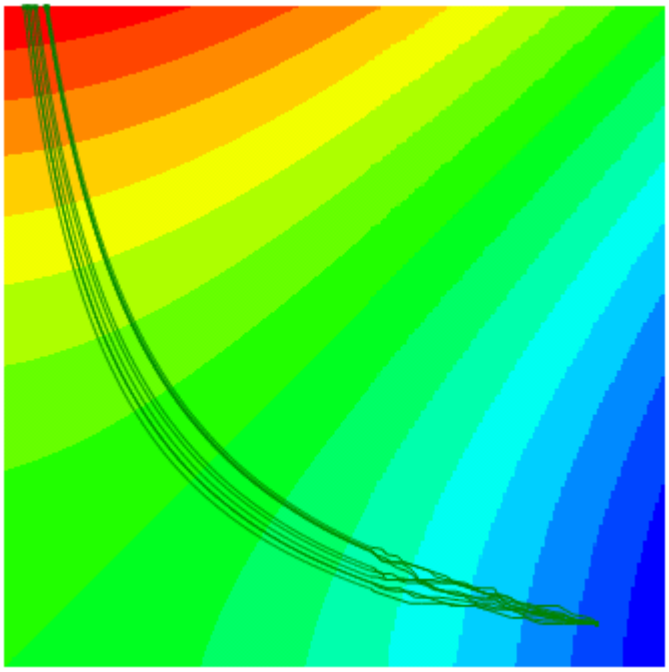

Figure 4-20 Backward particle tracks

An averaged particle track plot is compared against the analytical solution in Figure 4-21, the results agreeing to within 2% of the analytical solution for position and travel time.

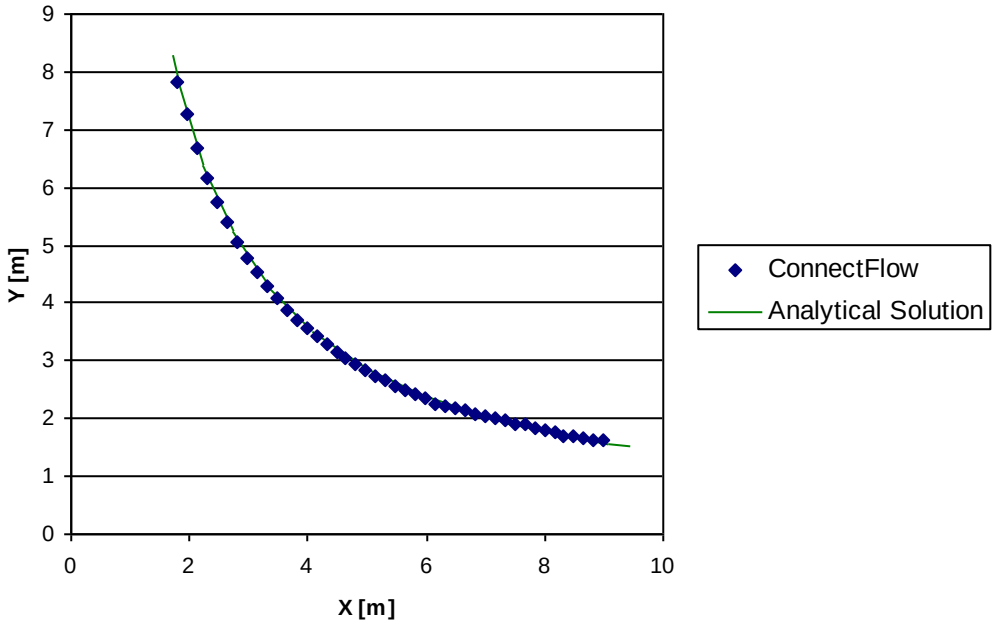

Figure 4-21 Averaged backward particle tracks

4.4.4.5 Mass Conserving Particle Tracking

The mass conserving tracks behave in a similar manner to the non-mass conserving equivalents, with the results agreeing to within 2% of the analytical solution for position and travel time

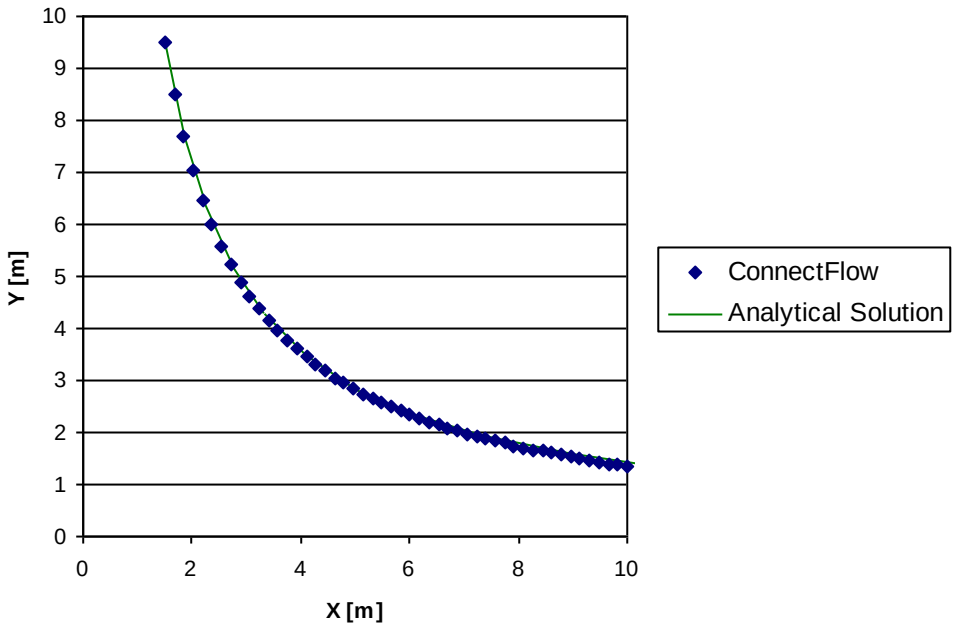

Figure 4-22 Averaged mass conserving particle tracks

4.5 Henry's Salt Transport Using Interpolated Density

4.5.1 Overview

This case considers the groundwater pressures arising from a spatially varying density field.

The geometry, boundary conditions and density field are taken from the modified Henry CPM Case 0.

4.5.2 Problem Definition

A schematic of the test case is shown in Figure 4-23 and the input parameters are given in Table 4-6.

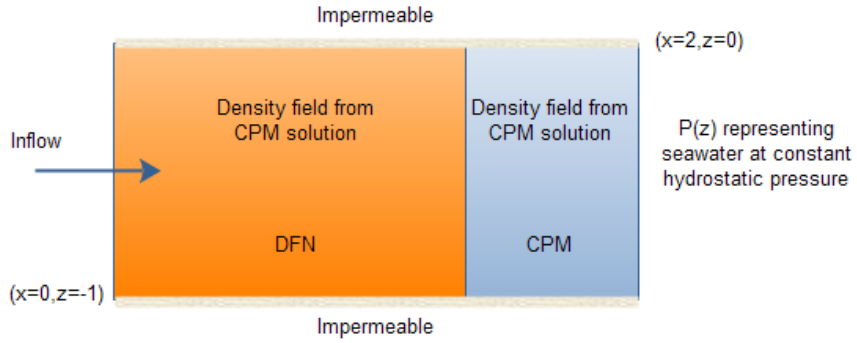

Figure 4-23 Henry's Problem

Table 4-6 Input parameters

Symbol	Parameter	Value
K	Hydraulic conductivity of rock	**1.0E-2 m/s**
Q	Freshwater inflow per unit depth	**9.43E-5 m^2/s**
ρ	Density	**Interpolated**
ϕ	Porosity	**0.35**
e	Fracture thickness	**1.8516E-4 m**

The DFN domain is represented by a single fracture tessellated into 0.025 m square sub-fractures. The fracture thickness is set to 1.8516E-4 m in order to generate the desired hydraulic conductivity of 1.0E-2 m/s. The DFN region covers the left 75% of the domain, which has been selected so that the interface between the CPM and DFN region is in a location where the density and pressure fields are rapidly changing.

The CPM region has thickness e/ϕ so that the cross sectional area available to flow remains constant. The CPM region is meshed with the same spatial resolution as the sub-fractures.

The interpolated density field used is shown in Figure 4-24.

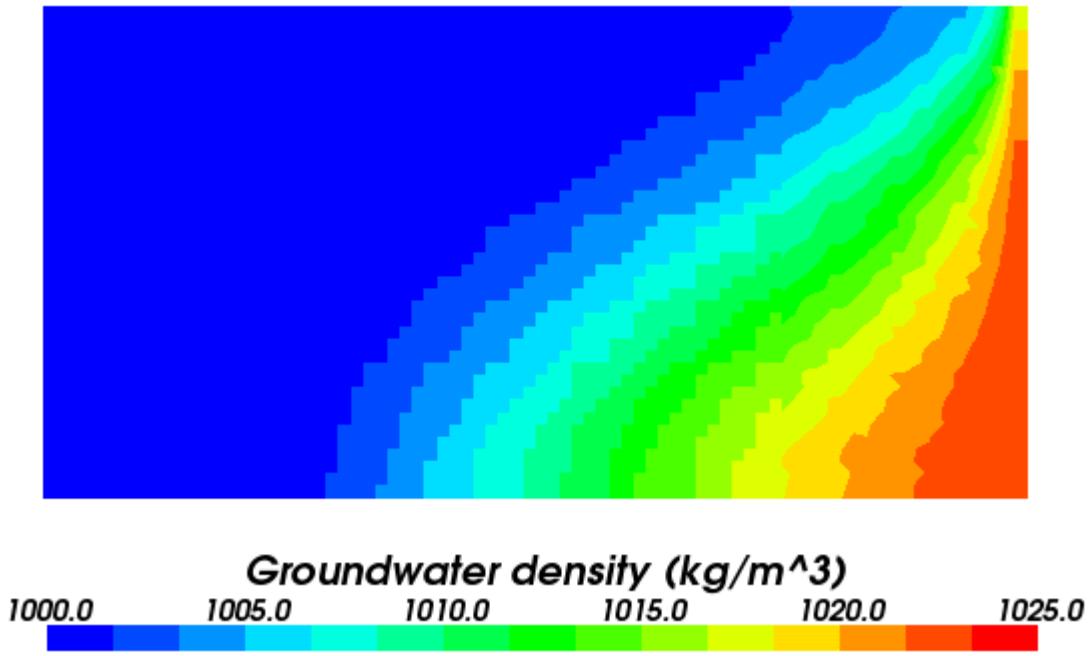

Figure 4-24 Interpolated density field

4.5.3 Results

The residual pressure field of the DFN/CPM calculation is compared against the CPM pressure field from case 0, the latter having been separately checked against the analytical solution via the salt concentration solution.

Plots of the two pressure fields are shown in Figure 4-25 and Figure 4-26. Although the pressure contours vary in shape near the inflow, in absolute terms the pressure fields agree to within 5%.

The influence of the density variation in this test case was checked by re-running with a constant average density instead of the interpolated density. In this case the difference in the pressure fields was 30% when compared with the CPM solution.

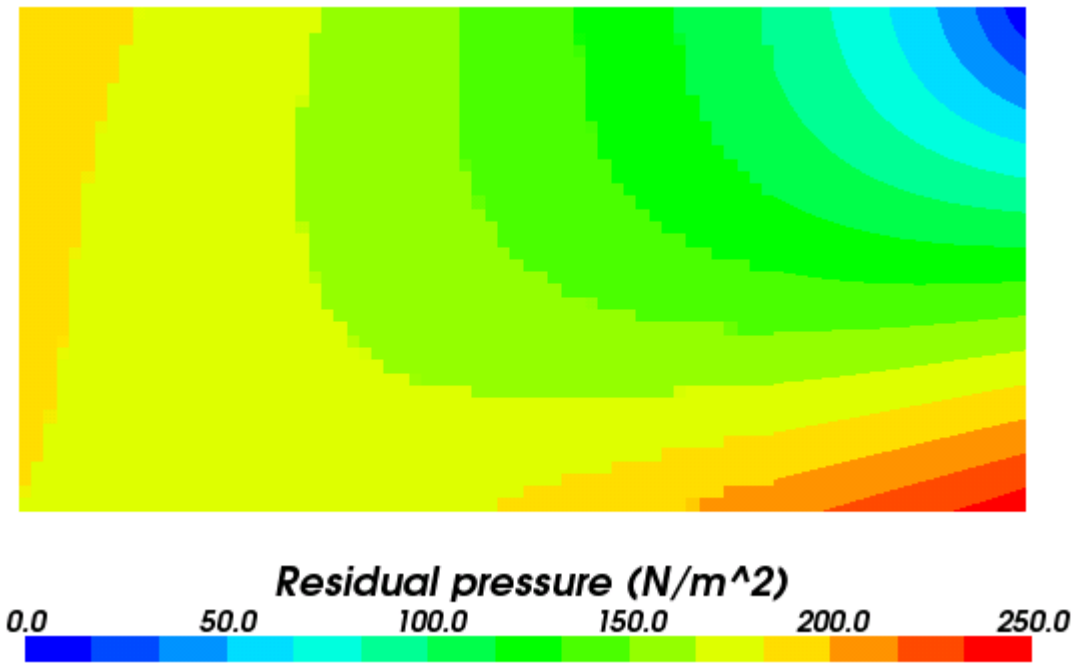

Figure 4-25 Residual pressure in the DFN/CPM model

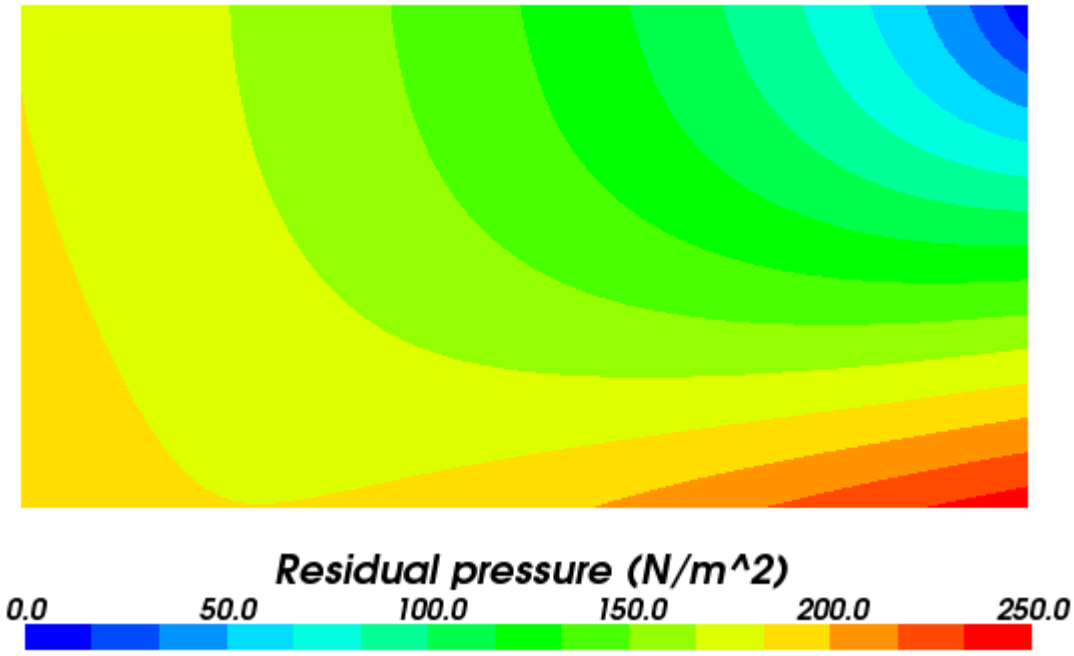

Figure 4-26 Residual pressure in the CPM model

4.6 Solute transport in Combined CPM-DFN models

4.6.1 Overview

This case considers transport of a solution through a simple combined CPM-DFN model.

4.6.2 Problem Definition

The model consists of two CPM regions of side length 9m, 10m and 10m along the X, Y and Z axes, respectively. These are joined by a single square tessellated fracture of length 10m, oriented parallel to the Y-Z plane. These three components are organised in a line along the Z-axis as shown in Figure 4-27. A pressure boundary condition of 0 Pa is applied at the bottom of the model (Z=0m) and 10 Pa is applied at the top (Z=30m). Flow therefore travels from the top to the bottom of the model. The parameters for the model are listed in Table 4-7. An equivalent CPM-only model has been created where the fracture is replaced by an equivalent set of CPM elements.

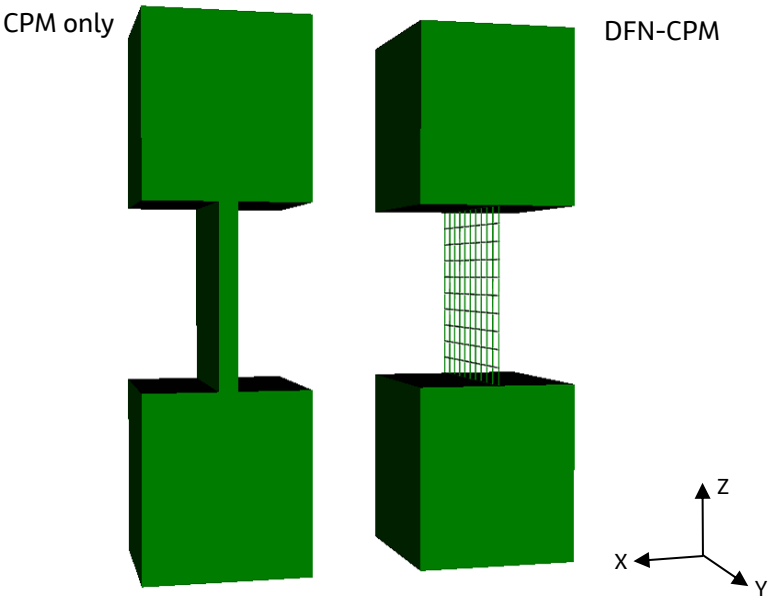

Figure 4-27: Shows the combined model alongside an equivalent CPM only model. The DFN fracture is shown in wireframe to show the tessellation.

Table 4-7 Key parameters for the DFN-CPM model and the equivalent CPM only model.

Symbol	Parameter	Value
k_v and k_h	Vertical and horizontal permeability of CPM	1.0×10^{-17} m^2 (vertical) 1.0×10^{-15} m^2 (horizontal)
a	Hydraulic aperture and transport aperture	2.31×10^{-5} m
ρ	Fluid density	1000 kg/m^3
ϕ	Porosity of CPM	0.00039
μ	Fluid viscosity	0.001 Pa s

The permeability of the CPM regions is anisotropic with much greater permeability in the horizontal direction than the vertical direction. This ensures that pressure isosurfaces are (roughly) perpendicular to the z-axis, allowing the pressure solution within the model to be approximated using simple analytic expressions:

Using Darcy's law, the flux through the bottom CPM block can be approximated by:

$$Q_1 = 90\frac{k_v}{\mu}\frac{(p_1)}{10}$$

where p_1 is the pressure at the top of the block (and bottom of the fracture). The flux through the fracture can be approximated by:

$$Q_2 = 10\frac{a^3}{12\mu}\frac{(p_2 - p_1)}{10}$$

where p_2 is the pressure at the top of the fracture (and the bottom of the top block). The flux through the top CPM block can be approximated by:

$$Q_3 = 90\frac{k_v}{\mu}\frac{(10 - p_2)}{10}$$

The three fluxes are equal $Q = Q_1 = Q_2 = Q_3$ so these three equations can then be solved for the three unknowns Q, p_1 and p_2. Thus

$$p_2 = 10\frac{0.75k_v a^3 + 81k_v^2}{1.5k_v a^3 + 81k_v^2} = 5.21\ Pa$$

$$p_1 = 4.79\ Pa$$

$$Q = 4.31\ \mathrm{x}\ 10^{-13}\mathrm{m}^3\mathrm{s}^{-1} = \ 4.31\ \mathrm{x}\ 10^{-10}\mathrm{kg\ s}^{-1}$$

Using the porosity and transport aperture, the travel time for a massless particle moving from the top of the model to the bottom can be calculated as t_f =1.63x10^{12} s.

The porewater is initially filled with a fluid A and fluid B is introduced at the top at time t=0. Using an outflow boundary condition at the bottom of the model will result in the model being filled with fluid B (and at steady state) at time t_f. Here we have assumed fluid A and fluid B have the same density and viscosity to simplify the analysis, but they can be different in a more general case.

Rock matrix diffusion is also ignored in the above example, but a second case, including rock matrix diffusion, is has also been developed. Table 4-8 shows the parameterisation for the matrix.

Table 4-8 Matrix diffusion parameters for the DFN-CPM model. (The CPM is, perhaps artificially, given matrix diffusion parameters to demonstrate the software functionality).

Parameter	Value
DFN/CPM matrix diffusion coefficient	3.0x10^{-4}/1.11x10^{-6} m^2/s
DFN/CPM matrix porosity	5.0x10^{-10}/1.11x10^{-15}
DFN/CPM matrix depth	15/15 m
DFN/CPM fracture surface area per unit volume	2 / 2 m^{-1}

Figure 4-28 shows the results comparing the combined model with the equivalent CPM model for cases with and without rock matrix diffusion. The agreement is excellent. Both models match well with the analytic calculation of the steady state flux and the model without rock matrix diffusion matches well with the analytic calculation of the time to reach steady state.

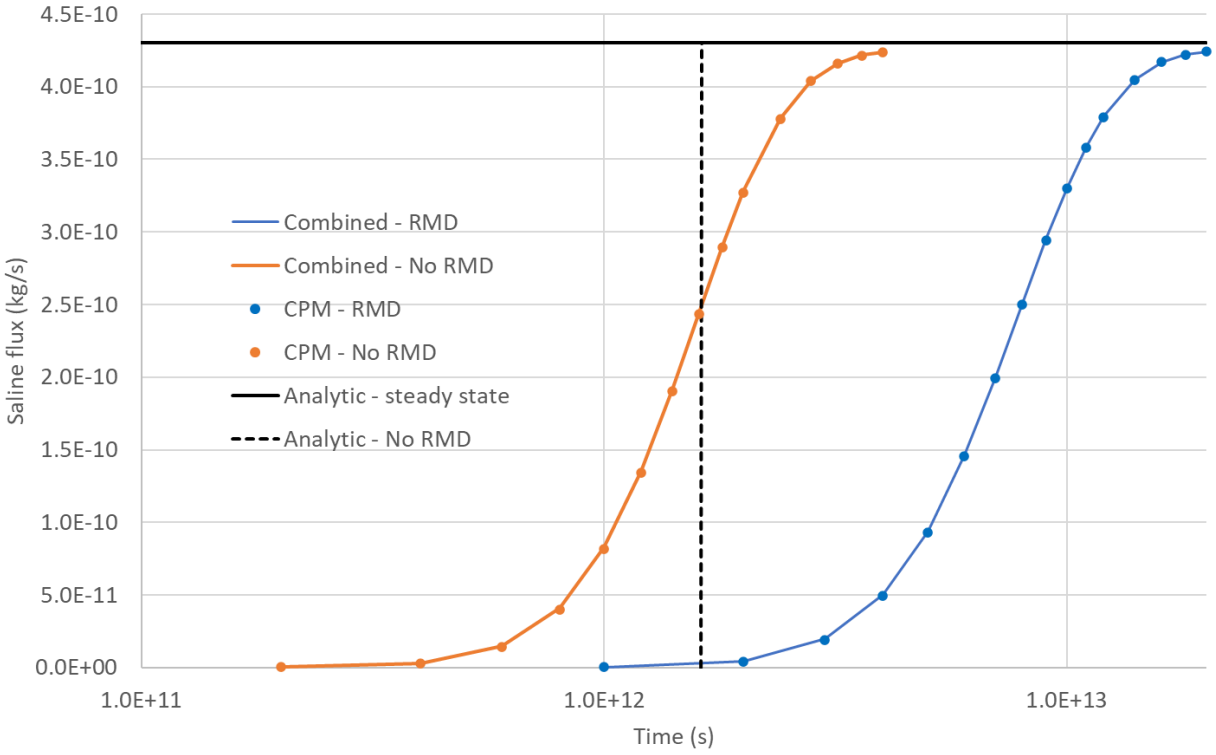

Figure 4-28: Comparison of the mass flux of fluid B through the bottom of the model. The combined DFN-CPM model and the CPM only model, are compared both with and without rock matrix diffusion. The agreement is excellent. Also shown are the steady state flux and the advective travel time, both calculated analytically.

5. Further Testing

This section references further testing that has taken place on the ConnectFlow suite of software, which complements and extends the testing covered in the earlier sections.

5.1 Continuum Porous Media

5.1.1 Verification

5.1.1.1 SKB – Implicit Representation of Fractures

Section 3.3 of SKB report R-01-49 [xxxii] describes the modelling of a set of fractures within a background rock matrix by modifying CPM permeabilities. The approach is tested on a simple 3D case with a semi-analytical solution. The results are all within 20% of the expected solution, with the accuracy improving for larger features. The algorithm allows small features to be modelled more accurately but with increased computational cost.

5.1.1.2 SKB – Heat Transport

Appendix F of SKB report R-06-98 [xxxiii] describes three verification tests on heat transport in ConnectFlow. The first case models 1D heat conduction with a time-varying temperature boundary condition. The second case models 1D heat conduction with a specified heat flux boundary condition. The final case models the HYDROCOIN Level 1 Test Case 5 for transient thermal convection in a saturated permeable medium containing a heat source with decaying power output. The first two cases have an analytical solution and the third a semi-analytical solution. In all cases ConnectFlow shows excellent agreement with the expected solutions.

5.1.1.3 SKB R-09-24

Appendix G of SKB report R-09-24 [xxxiv] describes a comparison of DarcyTools and ConnectFlow in modelling the inflow of fresh water into a repository under open repository conditions. The ConnectFlow simulation modeled the repository region as a combined DFN/CPM, with boundary conditions being applied from a separate DFN site scale model. DarcyTools used a single regional-scale ECPM model with fine grid refinement around the tunnels. Both models used the same Hydro-DFN data. The overall inflow to the repository agreed to within 20%.

5.1.1.4 ANDRA

A verification exercise for ConnectFlow has been performed for ANDRA [xxxv]. Cases covering a range of groundwater flow and radionuclide transport problems were investigated. The exercise included cases that were diffusion dominated, cases that were advection and dispersion dominated, cases in two- and three-dimensions, and cases with permeability contrasts between regions of the models such that the dominant flow and transport processes differed between the regions. With appropriate choices of the grid, the initial and boundary conditions, and the time-stepping scheme, ConnectFlow was found to accurately reproduce the analytical solutions given for all cases considered.

5.1.1.5 KBS-3

ConnectFlow has also been used in two reviews of repository assessments. These reviews compared the results obtained using different programs for the same finite-element model. In a review of the Swedish KBS-3 study [xxxvi], the groundwater heads obtained using ConnectFlow were compared with those obtained using the

program GWHRT, for several different cases. In every case, the results agreed to at least six significant figures (the number of figures listed for the output from GWHRT). This gives great confidence that both programs were coded correctly.

5.1.1.6 Gewähr

Results obtained using ConnectFlow were also compared with results obtained using the FEM301 program for the Swiss Project Gewähr [xxxvii]. Initially, the results obtained using ConnectFlow differed slightly from those obtained using FEM301. These differences were traced to discrepancies between the FEM301 program and its documentation, and differences between ConnectFlow and FEM301 in the treatment of highly distorted elements. When an appropriate temporary modification was made to ConnectFlow to enable it to mimic the behaviour of FEM301, the results obtained agreed to within five significant figures with those obtained from FEM301. It should be stressed that the initial differences were not due to any problems with ConnectFlow.

5.1.1.7 Nirex

The results of a Monte-Carlo study of dispersion in a heterogeneous porous medium [xxxviii] provides a useful and quite stringent test of the groundwater flow and particle transport algorithms used in ConnectFlow. The fact that good agreement could be obtained between the analytical and numerical results for the dispersion of the particles indicates that ConnectFlow provided an accurate solution for the groundwater flow in a heterogeneous permeability field. This case therefore also builds confidence in the correctness of ConnectFlow.

5.1.1.8 Olkiluoto Site

A site scale comparison of FEFTRA and ConnectFlow was carried out as part of the FEFTRA verification [iii]. The study showed good agreement with regard to borehole pressures and flow rates near the repository. Flow path positions near the repository were also in good agreement although the travel times were shorter in FEFTRA as compared with ConnectFlow.

A further study [xxxix] has compared modelling of pressures and salinity distributions in 15 deep core drilled boreholes between the codes and measurements based on simulations of the evolution of coupled groundwater flow and solute transport over the last 8000 years.

5.2 Discrete Fracture Network

5.2.1 Verification

5.2.1.1 Stripa

This testing exercise formed part of an OECD/NEA [xl] project relating to the final disposal of highly radioactive waste in crystalline rock, that involved a detailed characterisation of the granite formation in an abandoned iron ore mine at Stripa in central Sweden.

The testing compared fracture generation, steady state flow and particle tracking for the fracture flow codes ConnectFlow, FracMan/MAFIC and FMG.

Eight test cases were considered and the ConnectFlow results compared well with available analytical solutions and the results of FracMan/MAFIC and FMG (when a formulation of the test case was possible).

5.2.1.2 Nirex

This study [xli] compared transient flow for the fracture flow codes ConnectFlow and FracMan/MAFIC for six test cases. ConnectFlow and FracMan/MAFIC gave qualitatively similar results. However, significant quantitative differences were observed even for quite simple test networks. These are thought to be due to inadequate mesh discretisation of the source zone in FracMan/MAFIC. The ConnectFlow results for the early time behaviour compared well with the available analytical solutions, whereas FracMan/MAFIC gave source zone responses that were inaccurate. The asymptotic ConnectFlow results were shown to tend to the steady state solutions.

5.3 Automated Testing

The test cases presented in this document can be automatically re-run to check the results against the analytical and benchmark data.

This complements the regular ConnectFlow regression test suite, which consists of more than 200 tests and is used to comprehensively check results from new releases of the software against previous versions.

5.4 Peer Review

ConnectFlow is used by a wide variety of organisations with an interest in radioactive waste disposal. There are representatives of both the regulatory bodies and the nuclear utilities. Many of these participate in the iConnect club and provide valuable feedback that helps enhance the software quality.

6. References

i NAMMU Technical Summary, SA/ENV/CONNECTFLOW/8 May 2010

ii NAPSAC Technical Summary, SA/ENV/CONNECTFLOW/12 May 2010

iii FEFTRA Verification, VTT Research Notes 2385, Espoo 2007.

iv de Marsily, G., 1986. Quantitative Hydrogeology – Groundwater Hydrology for Engineers. Academic Press INC, Orlando.

v NEA/SKI, The International HYDROCOIN Project, Level 1: code verification, OECD Publications, 1988.

vi R. Atkinson, T.P. Cherill, A.W. Herbert, D.P. Hodgkinson, C.P. Jackson, J. Rae and P.C. Robinson, Review of the groundwater flow and radionuclide transport modelling in KBS-3, UKAEA Report AERE-R. 11140, 1984

vii NEA/SKI, The International HYDROCOIN Project, Level 3: uncertainty and sensitivity analysis, OECD Publications, 1991.

viii A. Schäfers. Task Force on Engineered Barrier Systems, "Code Validation". Code Validation Task Description. 2014.

ix Richards, L.A., 1931. Capillary conduction of liquids through porous mediums. Journal of Applied Physics, 1(5), pp.318-333.

x Zarba, R.L., Bouloutas, E.T. and Celia, M., 1990. General mass-conservative numerical solution for the unsaturated flow equation. Water Resources Research WRERAQ, 26(7), pp.1483-1496.

xi Van Genuchten, M.T., 1980. A closed-form equation for predicting the hydraulic conductivity of unsaturated soils. Soil science society of America journal, 44(5), pp.892-898.

xii K. Pruess, TOUGH2 – A General Purpose Numerical Simulator for Multiphase Fluid and Heat Flow, Lawrence Berkeley Laboratory Report LBL–29400, 1991.

xiii Bear Jacob, Hydraulics of Groundwater,1979, McGraw-Hill Inc.

xiv Improving the worthiness of the Henry problem as a benchmark for density dependent ground water flows. Water Resources Research Vol 40, 2004.

xv A R Hoch, C P Jackson Rock-matrix diffusion in transport of salinity. SKB Report R-04-78.

xvi C. M. Oldenburg and K. Pruess. EOS7R: Radionuclide Transport for Tough2, Lawrence Berkley Laboratory Report LBL-34868, Berkley, CA, November 1995.

xvii Javandel, I., C. Doughty, and C.-F. Tsang, Groundwater Transport, Handbook of Mathematical Models, American Geophys. Union, pp. 14-19, 1984.

xviii Joyce S, Applegate D, Appleyard P, Gordon A, Heath T, Hunter F, Hoek J, Jackson P, Swan D, Woollard H, 2014. Groundwater flow and reactive transport modelling in ConnectFlow. SKB R-14-19, Svensk Kärnbränslehantering AB.

xix Parkhurst D L, Kipp K L, Charlton S R, 2010. PHAST Version 2: a program for simulating groundwater flow, solute transport, and multicomponent geochemical reactions. Techniques and Methods 6-A35, U.S. Geological Survey, Denver, Colorado.

xx Hall, P. (1982). "On Some Simple Estimates of an Exponent of Regular Variation". Journal of the Royal Statistical Society, Series B (Methodological) 44 (1): 37–42.

xxi A. Banerjee, I. S. Dhillon, J. Ghosh, and S. Sra. Clustering on the Unit Hypersphere using von Mises-Fisher Distributions. JMLR, 6:1345–1382, Sep 2005.

xxii Aitchison, J. and Brown, J.A.C. (1957) The Lognormal Distribution, Cambridge University Press.

xxiii Robinson P.C. 1984, Numerical calculations of critical densities for lines and planes. J.Phys. A:Math. Gen. 17, 2823-2830.

xxiv Bour and Davey 1998, On the connectivity of three-dimensional fault networks, Water Resources Research, Vol 34

xxv DECOVALEX Task C Stage 1 Project Progress Report, Lanru Jing and John Hudson, 2009

xxvi DarcyTools, Version 2.1 Verification and validation R-04-21. Urban Svensson,

Computer-aided Fluid Engineering AB, Sweden. March 2004

xxvii NEA/SKI, The International HYDROCOIN Project, Level 1: code verification, OECD Publications, 1988.

xxviii R. Atkinson, T.P. Cherill, A.W. Herbert, D.P. Hodgkinson, C.P. Jackson, J. Rae and P.C. Robinson, Review of the groundwater flow and radionuclide transport modelling in KBS-3, UKAEA Report AERE-R. 11140, 1984

xxix G. Dagan & J. Bear (1968): Solving the problem of local interface upconing in a coastal aquifer by the method of small perturbations, Journal of Hydraulic Research, 6:1. 15-44

xxx A.D. Werner, D. Jakovovic, C.T. Simmons (2009): Experimental observations of saltwater up-coning, Journal of Hydrology, 337, 230-241

xxxi NEA/SKI, The International HYDROCOIN Project, Level 3: uncertainty and sensitivity analysis, OECD Publications, 1991.

xxxii Lee Hartley, Peter Jackson, Mike Poole Development of hydrogeological modelling tools based on NAMMU SKB Report R-01-49

xxxiii Lee Hartley, Andrew Hoch, Peter Jackson, Steve Joyce, Rachel McCarthy, William Rodwell, Ben Swift, 2006. Groundwater flow and transport modelling during the temperate period for the SR-Can assessment, SKB R-06-98, Svensk Kärnbränslehantering AB.

xxxiv Joyce S, Simson T, Hartley L, Applegate D, Hoek J, Jackson P, Roberts D, Swan D, Gylling B, Marsic N, Rhén I, 2010. Groundwater flow modelling of periods with temperate climate conditions – Laxemar. SKB R-09-24, Svensk Kärnbränslehantering AB.

xxxv S P Watson, M J Poole and A R Hoch, NAMMU Implementation of Test Cases for Flow and Transport in Porous Media, AEA Technology Report 14302/00/1 Issue 1, 2000.

xxxvi R Atkinson, T P Cherrill, A W Herbert, D P Hodgkinson, C P Jackson, J Rae and P C Robinson, Review of the Groundwater Flow and Radionuclide Transport Modelling in KBS-3, UKAEA Report AERE R.11140, 1984.

xxxvii P C Robinson, C P Jackson, A W Herbert and R Atkinson, Review of the Groundwater Flow Modelling of the Swiss Project Gewähr, UKAEA Report AERE R.11929, 1986

xxxviii S T Morris, J D Porter and C P Jackson, An Investigation of the Accuracy of the Spectral Turning Bands Random Field Generator, Nirex Report NSS/R320, 1997.

xxxix Lofman J and Meszaros F. Modelling of Groundwater Flow and Solute Transport in Olkiluoto - Update 2011, Posiva Working Report 2011-YY, in prep

xl F. Schwartz and G. Lee. Cross-verification Testing of Fracture Flow and Mass Transport Codes. Technical Report 91-29, Stripa Project, 1991

xli. Golders Associates -Transient solver cross code comparison between NAPSAC and FRACMAN/MAFIC. 94524312/21 April 1995.